School of graduate studies "Galileo Galilei"
Università Degli Studi di Pisa

PhD Thesis

Modelling environment effects on spectroscopic molecular responses with hybrid QM/classical methods

CANDIDATE

Alessandro Biancardi

SUPERVISOR

Prof. Benedetta Mennucci

EXTERNAL ADVISOR

Prof. Luca Frediani

SSD CHIM/02

XXIV CYCLE, YEARS 2008 - 2011

The most important discoveries are made only when you can see the greater connections.

Walter Thirring

Contents

Introduction

The objective of this thesis is the modelling of environment effects on spectroscopic molecular responses, using hybrid QM/classical methods.

The term "environment effects", is a general term that refers to the modifications of the behaviour of a molecular system when it is in condensed phase, for instance when surrounded by a solvent, a membrane or an interface, as well as by a pocket in a nucleic acid or in a cyclodextrin. Different environments modify the spectroscopic molecular responses in a unique manner, e.g. in case of absorption and emission UV/vis spectra measured in different environments, positions and intensities of the bands are changed and the changes depend strongly on the environment. In solution these modifications are referred to as solvatochromism.

A precise understanding of the connection between spectroscopic molecular responses and environment effects is still lacking, and the interpretation of experimental results may present controversial issues. A deeper understanding of the environment effects involving different intermolecular interactions and coupled dynamical processes, can be achieved combining the experimental observations with the computational modelling, which provides a quantitative description of environment effects and a microscopic insight into structural and dynamical effects of the local environment.

Since the huge number of molecules that must be considered in order to simulate a condensed phase and get a physically and statistically correct picture, a fully Quantum Mechanical (QM) study is unfeasible. Focused descriptions based on hybrid QM/classical approaches are needed in order to reduce the computational cost of the simulation. In such focused models, the investigated system is partitioned into two layers: a focused one, the molecular system of interest comprising the so-

lute plus eventually some solvent molecules, and the rest, i.e. the environment. The focused layer is usually described using an accurate QM technique, whereas the environment is described classically, for instance employing classical Molecular Mechanics (MM) or Polarizable Continuum Models (PCM). The environment is described using a classical force field, in the first case and as a structureless continuous dielectric, characterized by its macroscopic permittivity, in the second case.

The environment effects, i.e. the interactions between the focused layer and the environment, originate from specific and non-specific interactions. In the former case, the environment behaves like a discrete medium consisting of individual molecules that can be conveniently described using an accurate QM or a more approximated MM approach. In the case of a solvent, specific interactions correspond to the interactions between the solute and the first shell of solvation. Non-specific interactions are those between the solute and the outer shells of solvation. In this case, the interactions with individual (solvent) molecules are less important and in practice the environment behaves like a bulk, characterized by averaged quantity, for instance the dielectric permittivity. The solvent in such a case can be effectively described as a continuum. Continuum models usually assume that the electrostatic interaction with the solute due to the polarity of the environment is predominant over the other interactions (e.g. dispersive, repulsive and steric interactions). The latter are thus either neglected or described at a lower level of accuracy.

The focused approaches described in this thesis, are applied to the study of environment effects on:

- two-dimensional infrared (2D-IR) spectroscopic responses (study of vibrational couplings in peptides and DNA base pairs);
- electronic absorption and fluorescence spectroscopic responses (study of the electronic absorption and fluorescence transition energies, quenching and enhancing of the fluorescence, in homogeneous solvents, membranes and DNA pockets).

The thesis is organized as follows:

- Chapter 1 introduces the theoretical methodologies needed to model environment effects using hybrid QM/classical methods. Firstly, we consider the linear response extension of these techniques. Secondly, we focus on the modelling of vibrational couplings (or vibrational energy transfer) using two vibrational local modes approaches and their extension in the framework of Polarizable Continuing Model (PCM).

- Chapter 2 presents the modelling of the environment effects on molecular vibrations and vibrational couplings, using Transition Dipole Coupling (TDC) and Hessian Matrix Reconstruction (HMR). Firstly a comparative analysis of the two approaches is reported for a model system, then the HMR-PCM formalism is applied to the evaluation of the vibrational coupling between amide modes in peptides and between carbonyl vibrations of DNA base pairs. The purpose is to develop an accurate methodology suitable for effectively predicting and interpreting the vibrational couplings in solution.

- Chapter 3 presents the modelling of environment effects on the electronic absorption and fluorescence spectroscopic responses in several environments: a homogeneous solvent, a membrane and a pocket in DNA. The purpose is to achieve a microscopic understanding of the intermolecular effects which govern the absorption and fluorescence properties of complex environments. Firstly, the influence of different solvents on the photophysical properties of selected molecular probes, is analyzed using continuum, discrete and mixed discrete and continuum, solvation approaches, in order to achieve more insight on solvent-induced structural modifications, polarization effects, solubility, solute-solvent hydrogen-bonding interactions, and solute aggregation. Secondly, the influence of a membrane, on the photophysical properties of a selected molecular probe, is presented combining PCM with a molecular field theory for the positional-orientational-conformational distribution of the probes in the membrane. The dependence of the absorption and emission energies, on position and orientation across the interface is investigated. Finally, we analyze the environment effects on the cyanine thiazole orange (TO) in solution and when intercalated

in single and double stranded DNA; the dependence of the absorption and emission energies and of the quenching enhancing effects of fluorescence in the different environment is explored.

Chapter 1

Modelling environment effects

In this chapter, we provide a brief introduction of the theoretical methodologies for the modelling of environment effects. In section 1.1 we present how to model environment effects using hybrid QM/classical methods. In section 1.2 we focus on the linear response (LR) extension of these techniques and in section 1.3 we present how to model vibrational couplings using two vibrational local modes approaches, and their extension in the framework of Polarizable Continuum Model (PCM).

1.1 Hybrid QM/classical approaches

Within focused models, i.e. the hybrid QM/classical approaches, such as the hybrid Quantum Mechanics/Polarizable Continuum Model (QM/PCM) or the hybrid Quantum Mechanics/Molecular Mechanics (QM/MM) model, the effective Hamiltonian, $\hat{H}_{\text{eff}}$, is the sum of the gas phase Hamiltonian ($\hat{H}_0$) of the focused part, described at the QM level, and of the interaction Hamiltonian ($\hat{H}_{\text{int}}$);

$$\hat{H}_{\text{eff}} = \hat{H}_0 + \hat{H}_{\text{int}} \tag{1.1}$$

where the latter describes the interaction between the focused part and the environment (and the self-interaction energy of the environment when it is described at the MM level); what distinguishes the different embedding approaches is the explicit form of the interaction Hamiltonian.

$$\hat{H}_{\text{int}} = \begin{cases} \hat{H}_{\text{QM/PCM}} & \text{(PCM)} \\ \hat{H}_{\text{QM/MM}} + H_{\text{MM}} & \text{(MM)} \end{cases} \tag{1.2}$$

The explicit formulation of the interaction Hamiltonians will be presented in sections 1.1.1 and 1.1.2.

1.1.1 The QM/PCM approach

In the QM/PCM approach [1–3], the focused part of the system is described at a QM level, whereas the environment is described as a macroscopic continuum medium having suitable dielectric properties. The main reason for this choice is the computational simplicity and the possibility to study a broad class of physical phenomena within the same framework.

In this approach, the focused part is embedded in a molecular-shaped cavity inside a polarizable continuum dielectric (characterized by a dielectric permittivity $\epsilon(\boldsymbol{r})$) which represents the long range electrostatic response of the environment. The polarization of the dielectric produces a reaction potential, which is given in terms of an apparent surface charge σ spread on the cavity surface. This is a classical electrostatic problem nested within the QM model. To determine the apparent surface charge, the Poisson equation for a charge distribution ρ embedded in a cavity, surrounded by and infinite dielectric with permittivity, ε, needs to be solved.

$$-\boldsymbol{\nabla} \cdot [\varepsilon(\boldsymbol{r}) \boldsymbol{\nabla} V(\boldsymbol{r})] = 4\pi\rho(\boldsymbol{r}) \tag{1.3}$$

which can be rewritten as:

$$\begin{aligned} -\boldsymbol{\nabla}^2 V(\boldsymbol{r}) &= 4\pi\rho(\boldsymbol{r}) \quad \text{inside the cavity} \\ -\varepsilon\boldsymbol{\nabla}^2 V(\boldsymbol{r}) &= 0 \qquad \text{outside the cavity} \end{aligned} \tag{1.4}$$

with two jump conditions for the potential,

$$V_{\text{in}} - V_{\text{out}} = 0 \tag{1.5}$$

and its normal derivative on the cavity surface,

$$\frac{\partial V_{\text{in}}}{\partial \boldsymbol{n}} - \epsilon \frac{\partial V_{\text{out}}}{\partial \boldsymbol{n}} = 0 \tag{1.6}$$

where $\boldsymbol{n}$ is the normal vector to the cavity surface.

In the computational practice the cavity surface is approximated in terms of small surface elements (called *tesserae*) using a boundary element method (BEM); after discretization, the apparent surface charge σ can be written in terms of point charges, q_k, which uniquely define the polarization of the solvent. As a result, the interaction Hamiltonian of Eq. 1.2, can be written:

$$\hat{H}_{\text{QM/PCM}} = \sum_k q_k \hat{V}_k \tag{1.7}$$

where q_k and $\hat{V}_k$ are the apparent surface charge and electrostatic potential on the *tessera* k

The discrete point charges q_k can be obtained self-consistently by either a matrix inversion or an iterative procedure; [4] in the former case the electrostatic problem is recasted in the following matrix form, which is common to all versions of PCM: [1]

$$\boldsymbol{q} = -\boldsymbol{Q}\boldsymbol{V} \tag{1.8}$$

where $\boldsymbol{Q}$ is the PCM response matrix (correlating the solute potential on the *tesserae* to the dielectric polarization), a square matrix depending only on geometrical factors and the dielectric constant of the medium (its dimension is $T \times T$, with T the number of tesserae); $\boldsymbol{q}$ is the vector collecting the unknown apparent surface point charges and $\boldsymbol{V}$ is a vector collecting the electric potential due to the charge density of the focused part.

What distinguishes the different versions of PCM is the explicit form of the PCM response matrix $\boldsymbol{Q}$; in the present thesis we have considered the Integral Equation Formalism version of Polarizable Continuum Model (IEF-PCM), developed by Cancès and Mennucci [5,6], which will be described in section 1.1.1.1. It is quite flexible and general, because the potentials are redefined in terms of the proper Green's func-

tion and thus can be applied with the same strategy to very different media ranging from isotropic to anisotropic solvents, or membrane and interfaces. Its application to membrane and interfaces will be described in section 1.1.1.2.

1.1.1.1 The integral equation formalism version of PCM (IEF-PCM)

Using the Green's function the potential is redefined in terms of additive contributions, $G(\boldsymbol{r},\boldsymbol{r}')\,\rho(\boldsymbol{r}')\,d\boldsymbol{r}'$, arising from the individual charge elements $\rho(\boldsymbol{r})\,d\boldsymbol{r}$, where $G(\boldsymbol{r},\boldsymbol{r}')$ is the potential in $\boldsymbol{r}$ generated by a unitary charge in $\boldsymbol{r}'$; thus for a charge distribution $\rho(\boldsymbol{r})$ the associated potential, becomes:

$$V(\boldsymbol{r}) = \int G(\boldsymbol{r},\boldsymbol{r}')\,\rho(\boldsymbol{r}')\,d\boldsymbol{r}' \tag{1.9}$$

Since $G(\boldsymbol{r},\boldsymbol{r}')$ is the potential generated by a unitary charge, the corresponding Poisson equation can be written as:

$$-\boldsymbol{\nabla}\cdot\left[\varepsilon(\boldsymbol{r})\,\boldsymbol{\nabla}G(\boldsymbol{r},\boldsymbol{r}')\right] = 4\pi\delta(\boldsymbol{r}-\boldsymbol{r}') \tag{1.10}$$

An analytical solution of the Green's function is available for isotropic and in some anisotropic environments; for instance, the Green's function inside the cavity (in vacuo) is $G_i(\boldsymbol{x},\boldsymbol{y}) = \frac{1}{|\boldsymbol{x}-\boldsymbol{y}|}$, whereas the Green's function outside the cavity (in an isotropic liquid with a dielectric permittivity ε) is $G_e(\boldsymbol{r},\boldsymbol{r}') = \frac{1}{\varepsilon|\boldsymbol{r}-\boldsymbol{r}'|} = \frac{G_i(\boldsymbol{x},\boldsymbol{y})}{\varepsilon}$. When an analytical solution is not available it can effectively be built numerically as, for example, in the case of diffuse interfaces and membranes (See Section 1.1.1.2).

Within this framework the solution of Eq. 1.3 may be rewritten as: [5,6]

$$\left\{\left(2\pi-\hat{D}_e\right)\hat{S}_i + \hat{S}_e\left(2\pi-\hat{D}_i^*\right)\right\}\sigma = -\left\{\left(2\pi-\hat{D}_e\right)V + \hat{S}_e\frac{\partial V}{\partial n}\right\} \tag{1.11}$$

where V is the electric potential due to the charge density of the focused part and D_a, D_a^*, S_a are integral operators formally defined for σ by:

$$\left(\hat{S}_a\cdot\sigma\right)(\boldsymbol{x}) = \int_\Gamma G_a(\boldsymbol{x},\boldsymbol{y})\,\sigma(\boldsymbol{y})\,d\boldsymbol{y} \tag{1.12}$$

$$\left(\hat{D}_a \cdot \sigma\right)(\boldsymbol{x}) = \int_\Gamma \left[\varepsilon_a \boldsymbol{\nabla}_y G_a(\boldsymbol{x}, \boldsymbol{y}) \cdot \boldsymbol{n}(\boldsymbol{y})\right] \sigma(\boldsymbol{y})\, d\boldsymbol{y} \tag{1.13}$$

$$\left(\hat{D}_a^* \cdot \sigma\right)(\boldsymbol{x}) = \int_\Gamma \left[\varepsilon_a \boldsymbol{\nabla}_x G_a(\boldsymbol{x}, \boldsymbol{y}) \cdot \boldsymbol{n}(\boldsymbol{x})\right] \sigma(\boldsymbol{y})\, d\boldsymbol{y} \tag{1.14}$$

where the index $a = i$ or e indicates the internal or the external of the cavity, respectively; thus $\varepsilon_i = 1$ and $\varepsilon_i = \varepsilon$ are the dielectric permittivities inside and outside the cavity.

For an isotropic environment Eq. 1.11 reduces to the isotropic IEF-PCM equation:

$$\left\{\left[2\pi\left(\frac{\varepsilon+1}{\varepsilon-1}\right) - \hat{D}_i\right]\hat{S}_i\right\}\sigma = -\left\{2\pi - \hat{D}_i\right\}V \tag{1.15}$$

The partitioning of the cavity surface in small *tesserae* allows us to rewrite Eq. 1.11 and 1.15 as a set of T coupled equations (T is the number of *tesserae*). In matrix form, the matrix Q of Eq. 1.8 can be rewritten as:

$$\boldsymbol{Q} = \boldsymbol{T}^{-1}\boldsymbol{R} = \left\{\left[2\pi\left(\frac{\varepsilon+1}{\varepsilon-1}\right)\boldsymbol{A}^{-1} - \boldsymbol{D}\right]\boldsymbol{S}\right\}^{-1}\left[2\pi\boldsymbol{A}^{-1} - \boldsymbol{D}\right] \tag{1.16}$$

where $\boldsymbol{A}$ is a diagonal matrix containing the area of the tesserae (a_k) and $\boldsymbol{D}$ and $\boldsymbol{S}$ are the matricial representations of the corresponding integral operators: [7]

$$D_{ij} = \begin{cases} \frac{(\boldsymbol{s}_i - \boldsymbol{s}_j)\cdot\hat{n}_j}{|\boldsymbol{s}_i - \boldsymbol{s}_j|^3} & \text{if } i \neq j \\ -\left(2\pi + \sum_{j\neq i} D_{ij}a_j\right)\frac{1}{a_i} & \text{if } i = j \end{cases} \tag{1.17}$$

$$S_{ij} = \begin{cases} \frac{1}{|\boldsymbol{s}_i - \boldsymbol{s}_j|} & \text{if } i \neq j \\ 1.0694\sqrt{\frac{4\pi}{a_i}} & \text{if } i = j \end{cases} \tag{1.18}$$

1.1.1.2 The Green's function for interfaces and membranes

Since the first attempt of Onsager and Samaras in 1934, [8] in continuum model studies the interfaces are described as a step discontinuity between two continuous dielectric media, i.e. an inhomogeneous medium in which the dielectric constant

changes discontinuously from one dielectric to another. This common step-interface approximation shows some serious shortcomings and can provide unphysical results in proximity of the interface.

In order to overcome these limitations, a recent extension of the Polarizable Continuum Model (PCM) to study diffuse interfaces was proposed by Frediani et al. [9] in the formalism of the IEF-PCM. This approach can account for the effect of the non-uniform dielectric environment on the electronic states of the probe and seems to be able to provide results comparable to MD simulations. [10] In this extension, an inhomogeneous medium represented by a dielectric with a continuum varying dielectric function $\epsilon(\boldsymbol{r})$ which changes continuously from one bulk dielectric to another, over a few Angstrom. Since in that cases an analytical solution is not available, the Green's function is built numerically.

Analogously to the case of sharp boundaries, the Green's function at a diffuse interface (with a dielectric constant varying on the z-axis) can be formally written as: [9]

$$G^E\left(\boldsymbol{r},\boldsymbol{r}'\right) = \frac{1}{C\left(z,z'\right)\left|\boldsymbol{r}-\boldsymbol{r}'\right|} + G_{img}\left(\boldsymbol{r},\boldsymbol{r}'\right) \tag{1.19}$$

where the first term is a Coulomb-like term with the dielectric constant replaced by an effective dielectric function $C(z,z')$ that can be obtained through the following steps and G_{img} is the image term corresponding to the step-interface.

The electrostatic problem within an inhomogeneous dielectric, i.e. within a diffuse interface and membrane, can be solved using the Green's function $G\left(\boldsymbol{r},\boldsymbol{r}'\right)$, which is solution of the Poisson equation:

$$\boldsymbol{\nabla}\cdot\left[\epsilon(z)\,\boldsymbol{\nabla}G\left(\boldsymbol{r},\boldsymbol{r}'\right)\right] = -4\pi\delta(\boldsymbol{r}) \tag{1.20}$$

where it is assumed that dielectric constant, varies only along the z-axis. In view of the translational symmetry the z-axis can be separated from the the two-

dimensional space of x and y, as:

$$G\left(\boldsymbol{r},\boldsymbol{r}^{'}\right)=\frac{1}{\pi}\int e^{i\boldsymbol{k}_{||}\cdot\left(\boldsymbol{r}_{||}-\boldsymbol{r}_{||}^{'}\right)}g\left(z,z^{'},k_{||}\right)d\boldsymbol{k}_{||} \tag{1.21}$$

where $\boldsymbol{r}_{||}$ and $\boldsymbol{r}_{||}^{'}$ are the projections of $\boldsymbol{r}$ and $\boldsymbol{r}^{'}$ onto the interface plane and $g\left(k,z,z^{'}\right)$ the reduced Green's function. Substituting Eq. (1.21) into Eq. (1.20) the following differential equation for the reduced Green's function $g\left(k,z,z^{'}\right)$ can be obtained:

$$\frac{d}{dz}\left[\epsilon\left(z\right)\frac{d}{dz}g\left(k,z,z^{'}\right)\right]-k^{2}\epsilon\left(z\right)g\left(k,z,z^{'}\right)=-2\pi\delta\left(z-z^{'}\right) \tag{1.22}$$

The reduced Green's function $g\left(k,z,z^{'}\right)$ can be obtained using a finite-difference approach from the former equation. Since the transformed Green's function of Eq. 1.19 can be written as

$$g\left(k,z,z^{'}\right)=\frac{1}{C\left(z,z'\right)k}e^{k|z-z'|}+g_{img}\left(k,z,z^{'}\right) \tag{1.23}$$

the effective dielectric function $C\left(z,z'\right)$, can be obtained taking the limit of the transformed Green's function:

$$\frac{1}{C\left(z,z'\right)}=\lim_{k\to+\infty}k\,e^{k|z-z'|}G\left(k,z,z^{'}\right) \tag{1.24}$$

Further details about the theoretical apparatus needed to compute $q\left(s_{k},\epsilon\left(z\right),\varrho\right)$ in presence of inhomogeneous media, such as liquid/liquid interfaces, liquid/gas interfaces or planar membranes within PCM have been discussed in ref. [9].

1.1.2 The QM/MM-Pol approach

In the QM/MM-Pol approach [11], the focused part of the system is described at a QM level, whereas the environment is described through a classical polarizable force field, using a set of atomic point charges, q_m, and a set of induced dipoles, μ_a.

Electrostatic forces are described by atomic partial charges, whereas polarization is explicitly treated by adding isotropic polarizabilities at selected points in the solvent molecules. Thus the interaction Hamiltonian, $\hat{H}_{\mathrm{QM/MM}}$ (of Eq. 1.2), is composed by two interaction terms: one due to the charges, $\hat{H}_{\mathrm{elec}}$, and one due to the induced dipoles, $\hat{H}_{\mathrm{pol}}$. The self interaction between charges and dipoles, H_{MM}, must also be included:

$$\hat{H}_{\mathrm{QM/MM}} = \hat{H}_{\mathrm{elec}} + \hat{H}_{\mathrm{pol}} = \sum_m q_m \hat{V}_m - \frac{1}{2}\sum_a \boldsymbol{\mu}_a \hat{\boldsymbol{E}}_a \tag{1.25}$$

$$H_{\mathrm{MM}} = \sum_m q_m \sum_{n>m} \frac{q_n}{|\boldsymbol{r}_{nm}|} - \frac{1}{2}\sum_a \boldsymbol{\mu}_a \sum_m \frac{q_m \left(\boldsymbol{r}_a - \boldsymbol{r}_m\right)}{\left|\boldsymbol{r}_a - \boldsymbol{r}_m\right|^2} \tag{1.26}$$

where q_m and $\hat{V}_m$ are the MM atomic point charge and the molecular potential on the site m, respectively; $\hat{\boldsymbol{E}}_a$ and $\boldsymbol{\mu}_a$ are the electric field due to the charge distribution and the induced dipole, on the site a, respectively; indices m and a refer to the solvent charge sites and latter to the solvent polarization sites.

The induced dipoles $\boldsymbol{\mu}_a$ on each polarizable site are given by

$$\boldsymbol{\mu}_a^{\mathrm{ind}} = \alpha_a \left(\boldsymbol{E}_a + \boldsymbol{E}_a^{\mathrm{solvent}}\left\{q_i, \boldsymbol{\mu}_{i\neq a}^{ind}\right\}\right) \tag{1.27}$$

where α_a is the isotropic polarizability, $\boldsymbol{E}_a$ is the electric field due to the charge distribution of the focused part and $\boldsymbol{E}_a^{\mathrm{solvent}}$is the total solvent electric field calculated at the specific site; since the induced dipole moments depends on all other induced dipole moments, the former equation needs to be solved iteratively or using a matrix inversion. In the latter case the problem of finding the induced dipoles can be reduced to the following matrix equation, which is analogous to Eq. (1.8):

$$\boldsymbol{\mu}^{\mathrm{ind}} = \boldsymbol{B}\boldsymbol{E} \tag{1.28}$$

where $\boldsymbol{B}$ is a square matrix only depending on geometrical parameters (its dimension is $3N \times 3N$, with N the number of polarizable sites); $\boldsymbol{\mu}^{\mathrm{ind}}$ is the vector collecting the unknown induced dipoles and $\boldsymbol{E}$ is the vector collecting the electric fields due to the charge density of the focused part.

Once the apparent surface charges (through Eq. 1.8) or the induced dipoles (through Eq. 1.28), have been determined, they can be used to compute molecular properties. However, both the induced dipoles, μ_a, and the apparent surface polarization charges, q_k, implicitly depend on the wavefunction of the focused part (whereas the atomic partial charges of the QM/MMpol are fixed). Therefore the formers introduce a further nonlinearity in the SCF resolution of the quantum mechanical problem of the focused part. In the standard Self Consistent Field (SCF) approach (either in its Hartree-Fock or DFT formulation) this nonlinearity modifies the SCF scheme in what is generally known as Self Consistent Reaction Field (SCRF) problem, in which there is a mutual polarization between the focused part and its environment.

1.2 Electronic excited states

An electronic transition in solvated molecular systems acts as a perturbation of the properties and dynamics of the solvent molecules. The solvent response, i.e. the polarization, may be divided in fast and slow component. The fast one is mainly electronic in character, and instantaneously responds to the perturbation, whereas the static (slow) component does not change, immediately but it remains fixed in equilibrium with the initial situation. These differences in response times may lead to non equilibrium states, in which the fast component is equilibrated and the slow component is not equilibrated, with the excited charge distribution of the solute.

The full process of formation and relaxation of an electronic excited state is generally simplified in terms of three sequential time steps (see Figure 1.1):

(i) vertical excitation (the environment molecules remain oriented in their ground state configuration, i.e. the slow polarization component remains fixed, while the fast part of the polarization instantaneously readjusts),

(ii) relaxation of the slow degree of freedom of the excited state (with an increase of time also the slow part of environment polarization gradually reorients to the equilibrium), and

(iii) vertical emission towards the vertical ground state (finally the probe undergoes a radiative process, in which only the fast part of the polarization readjusts, emitting the fluorescence radiation).

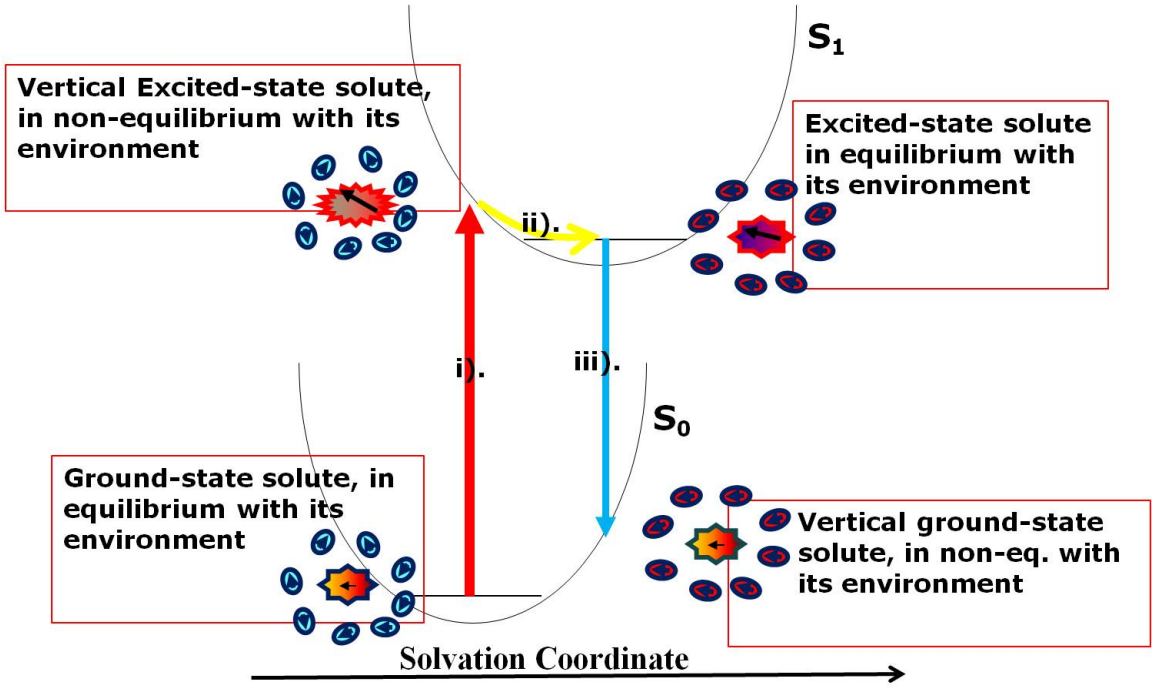

Figure 1.1: A simplified representation of the formation and relaxation of an electronic excited state .

In the presence of a polarizable environment, the three steps are characterized by three specific delays in the solvent response, also known as nonequilibrium effects, which have to be properly included in the calculations of both absorption and emission energies.

A valid strategy for the study of the environment effects on solvated molecular systems undergoing an electron transition is represented by the extension of the linear response (LR) scheme to continuum (LR-QM/PCM) [12] or discrete (LR-QM/MMpol) [11] polarizable solvation approaches. In these LR approaches the excitation energies are determined as the poles of the frequency-dependent response function of the investigated molecular system, described by the effective Hamiltonian. Moreover, the LR approach avoids the explicit calculation of the wavefunction

of the excited electronic state, which is needed in the alternative State Specific (SS) approach.

In the LR approaches the excitation energies can be determined by solving the following matrix equation: [13]

$$\begin{pmatrix} \boldsymbol{A} & \boldsymbol{B} \\ \boldsymbol{B}^* & \boldsymbol{A}^* \end{pmatrix} \begin{pmatrix} \boldsymbol{X}_n \\ \boldsymbol{Y}_n \end{pmatrix} = \omega_n \begin{pmatrix} 1 & 0 \\ 0 & -1 \end{pmatrix} \begin{pmatrix} \boldsymbol{X}_n \\ \boldsymbol{Y}_n \end{pmatrix} \tag{1.29}$$

where $\boldsymbol{A}$ and $\boldsymbol{B}$ collect the Hessian component of the energy functional with respect to the wavefunction variational parameter; the solution of the former equation yields the excitation energies, ω_n, and the transition vectors $\begin{pmatrix} \boldsymbol{X}_n \\ \boldsymbol{Y}_n \end{pmatrix}$ representing the first order changes in the wavefunction.

In condensed phase the $\boldsymbol{A}$ and $\boldsymbol{B}$ matrices include of a polarization contribution ($\boldsymbol{C}_{pol}$) which accounts for the fast environment response, associated with a specific energy transition.

$$\boldsymbol{A} = \boldsymbol{A}_{\text{vacuo}} + \boldsymbol{C}_{\text{pol}} \tag{1.30}$$

$$\boldsymbol{B} = \boldsymbol{B}_{\text{vacuo}} + \boldsymbol{C}_{\text{pol}} \tag{1.31}$$

What distinguishes the LR-QM/PCM and the LR-QM/MMpol approaches, is the explicit form of the polarization contribution.

In the LR-QM/PCM approach the nonequilibrium effects are accounted for by partitioning the solvent induced charges into a dynamical ($\boldsymbol{q}_{\text{dyn}}$, fast) and an inertial ($\boldsymbol{q}_{\text{in}}$, slow) component, [1]

$$\boldsymbol{q} \cong \boldsymbol{q}_{\text{dyn}} + \boldsymbol{q}_{\text{in}} \tag{1.32}$$

The slow component of the induced charges remains in equilibrium with the electronic initial state of the focused system, whereas the fast component of solvation is in equilibrium with the final state wavefunction and with the slow component of solvation. The implementation of this partition is realized using the static (ϵ_s) and the optical (ϵ_∞) dielectric constants, for the slow component and the dynamic

component, respectively. As a result, the polarization contribution (of Eqs. 1.30 and 1.31) can be written as: [12]

$$C^{\mathrm{Pol}}_{ai,bj} = \sum_k V_k \left(\phi_i \phi_a^*\right) q_k \left(\phi_j \phi_b^*; \epsilon_\infty\right) \tag{1.33}$$

In the LR-QM/MMpol approach the nonequilibrium effects are accounted for by using a polarizable classical force field. Non-polarizable classical force fields completely neglect the fast component of polarization and, although this may be a reasonable approximation for weakly polarizable solutes, it may be more questionable for more polarizable ones [11, 14] (e.g. in excited states that are usually more polarizable than the ground state). Thus a proper account of the nonequilibrium effects on both absorption and emission energies has to be done using the induced environment dipoles and the mutual polarization between the focused part and the environment, which is needed for an accurate simulation of the fast component of the polarization. As a result, the polarization contribution (of Eqs. 1.30 and 1.31) can be written as:

$$C^{\mathrm{Pol}}_{ai,bj} = \sum_k \boldsymbol{E}_k \left(\phi_i \phi_a^*\right) \boldsymbol{\mu}_k^{\mathrm{ind}} \left(\phi_j \phi_b^*; \alpha_k\right) \tag{1.34}$$

Although for molecular systems in vacuo the LR and SS approaches are equivalent, this is not longer true in condensed phase. [15] This because the LR approach is based on the focused ground state Hamiltonian, which does not account for the fast relaxation of the environment in the excited state. In order to partially account for the formation and relaxation of the solute excited state, in the case of PCM, Caricato et al. [16] developed a corrected Linear Response (cLR); using this improved approach the equilibrium and non-equilibrium LR energies are corrected by the interaction between the relaxation term of the density matrix (ρ_Δ) and the corresponding apparent charges ($q_k\left(\rho_\Delta\right)$):

$$\omega_K^{\mathrm{neq}} = \mathring{\omega_K} + \frac{1}{2} \sum_k V_k \left(\rho_{\Delta,\mathrm{neq}}\right) q_k \left(\rho_{\Delta,\mathrm{neq}}\right) \tag{1.35}$$

$$\omega_K^{\mathrm{eq}} = \mathring{\omega_K} + \frac{1}{2}\sum_k V_k\left(\rho_\Delta\right) q_k\left(\rho_\Delta\right) \tag{1.36}$$

where ω_K^{neq} and ω_K^{eq} are the cLR transition energies and $\mathring{\omega_K}$ is the LR transition energy, obtained in a completely frozen solvent.

1.3 Vibrational couplings

The usual description of molecular vibrations is based on the hypothesis of normal (uncoupled) vibrational modes (see appendix A); however, as shown by modern ultrafast infrared spectroscopic experiments, this picture cannot be strictly true for all cases, e.g. in case of the two-dimensional infrared (2D-IR) spectroscopy that not only gives the vibrational frequency of the different vibrations but also the couplings (the energy transfers or flow) between different vibrational modes.

The 2D-IR spectroscopy is a correlation spectroscopy with similarities to two-dimensional nuclear magnetic resonance (2D-NMR), which allows to follow what happens to vibrations, vibrational couplings and anharmonicities, in a molecule after ultrafast excitations, providing a two-dimensional view of infrared spectrum, which contain diagonal and off-diagonal peaks:

- diagonal peaks are associated with single molecular vibrations and reveal the energy of the vibrations
- off-diagonal peaks are determined by the vibrational coupling (or vibrational energy transfer) and provide direct information about structure and [17] dynamic of molecular systems, [18] and of the local environment. They are represented by the off-diagonal force constants ($k^{\alpha\beta}$), determined by the mixed derivative of the potential energy,

$$k^{\alpha\beta} = \frac{\partial V}{\partial \boldsymbol{l}_\alpha \partial \boldsymbol{l}_\beta} \tag{1.37}$$

where $\boldsymbol{l}_i$ is the i-th vibrational mode. These couplings can be empirically defined in terms of Local Modes (LM's), i.e. vibrational modes not strictly uncoupled, supposing that vibrations may be localized on certain bonds or

groups of atoms. [19–24]

The 2D-IR spectra are, however, very complex to interpret if not supported by a reliable and accurate theoretical method. Thus despite its potentiality, the extraction of structural information from the vibrational couplings (which determine the radiationless energy flow between different vibrational modes), requires the combination of experimental data with theoretical models.

The consideration of the local environment is crucial in order to realistically describe vibrational couplings in solution, mainly because the interaction with the environment modifies both vibrations and couplings. In order to allow these approaches to reach their full potential, it is of fundamental importance to incorporate solvent effects in all the "ingredients" of the models. A possible strategy is based on the use of classical molecular dynamics (MD) simulations or hybrid quantum-mechanical/MD approaches, in which the quantum nature of vibrational transitions is retained. [25] As a matter of fact, it appears evident that in many cases the solute-solvent interactions are mainly electrostatic, so that modelling of the solvating environment by a continuum solvation model may provide a good representation of solvent effects on vibrational spectra at a computational cost comparable with that of the corresponding calculation for the isolated system.

In the present section we extend the PCM to describe vibrational couplings among local vibrations in peptides within the Hessian matrix reconstruction (HMR) [26, 27] and the transition dipole coupling (TDC) [28–31] models. The TDC is the simplest approach and is based on the Coulomb interaction between the vibrational transition point dipoles associated to the interacting modes (accounting only for through-space interactions), whereas HMR is a more accurate approach, able to account for both through-space and through-bond effects. Both methods rely on the definition of a vibrational subspace described by a set of "local" vibrational modes on the molecular structure, which is chosen depending on the nature of the vibration under investigation [26, 29, 32]. In a first approximation, they are considered not interacting with the remaining vibrations.

1.3.1 Transition Dipole Coupling within the framework of PCM (TDC-PCM)

In this section we present a model to study the coupling between local vibrational modes in presence of an external dielectric medium mimicking the solvent. The local vibrational modes considered here involve a well spatially separated set of atomic nuclei which may belong to the same molecule or to distinct molecules. Under this condition, the vibrational coupling originates mainly from the through-space interaction, and, for isolated molecules, it may be expressed as the electrostatic interaction between the derivatives of the electronic density with respect to the LM's, $\boldsymbol{l}_\alpha$ and $\boldsymbol{l}_\beta$, of the two oscillators (see Eq. 1.37). In presence of an external medium, this electrostatic interaction presents an additional contribution. In our formulation the environment is described within the framework of the PCM. As described in section 1.1.1, within the PCM framework the polarization of the solvent is represented by the apparent surface charge density on the cavity hosting the solute charge distribution in the dielectric. This additional charge distribution modifies the electrostatic coupling between the vibrational oscillators, with respect to the gas phase case.

It is convenient to start by considering the case of two LM's coordinates $(\boldsymbol{l}_\alpha, \boldsymbol{l}_\beta)$, supported by two different molecules A and B, hosted within a dielectric medium. The charge distributions of the two molecules will be denoted as $\rho_A(\boldsymbol{l}_\alpha)$ for the LM $\boldsymbol{l}_\alpha$ and $\rho_B(\boldsymbol{l}_\beta)$, for the LM $\boldsymbol{l}_\beta$; each charge distribution ρ_x induces an apparent surface charge polarization σ_x . The electrostatic energy of the total system (charge distributions plus dielectric medium) can be written as, [33,34]

$$V_{AB}^{PCM}(\boldsymbol{l}_\alpha, \boldsymbol{l}_\beta) = V_{AB}^{direct}(\boldsymbol{l}_\alpha, \boldsymbol{l}_\beta) + \frac{1}{2} V_{AB}^{explicit}(\boldsymbol{l}_\alpha, \boldsymbol{l}_\beta) \tag{1.38}$$

where $V_{AB}^{direct}(\boldsymbol{l}_\alpha, \boldsymbol{l}_\beta)$ is the electrostatic interaction between the bare charge distributions (the same as in vacuo)

$$V_{AB}^{direct}(\boldsymbol{l}_\alpha, \boldsymbol{l}_\beta) = \int\int \frac{\rho_A(\boldsymbol{l}_\alpha; \mathbf{r}_i)\, \rho_B(\boldsymbol{l}_\beta; \mathbf{r}_j)}{|\mathbf{r}_i - \mathbf{r}_j|} d\mathbf{r}_i d\mathbf{r}_j \tag{1.39}$$

whereas $V_{AB}^{explicit}(\boldsymbol{l}_\alpha, \boldsymbol{l}_\beta)$ represents the additional electrostatic interactions induced by the presence of the environment,

$$V_{AB}^{explicit}(\boldsymbol{l}_\alpha, \boldsymbol{l}_\beta) = V_{\rho_A\sigma_A}(\boldsymbol{l}_\alpha, \boldsymbol{l}_\beta) + V_{\rho_A\sigma_B}(\boldsymbol{l}_\alpha, \boldsymbol{l}_\beta) + V_{\rho_B\sigma_B}(\boldsymbol{l}_\alpha, \boldsymbol{l}_\beta) + V_{\rho_B\sigma_A}(\boldsymbol{l}_\alpha, \boldsymbol{l}_\beta) \quad (1.40)$$

where:

$$V_{\rho_x\sigma_y}(\boldsymbol{l}_\alpha, \boldsymbol{l}_\beta) = \int\int_\Sigma \frac{\rho_y(\boldsymbol{l}_\alpha, \mathbf{r}_i)\,\sigma_x(\boldsymbol{l}_\alpha, \mathbf{s}_i)}{|\mathbf{r}_i - \mathbf{s}_j|} d\mathbf{r}_i d\mathbf{s}_j \qquad x, y = A, B\,. \quad (1.41)$$

In the last equation $V_{\rho_x\sigma_y}$ represents the electrostatic interaction between the charge distribution ρ_x and apparent charge σ_x, induced by ρ_y (x, $y = A$, B).

The force constant $k_{AB}(\boldsymbol{l}_\alpha, \boldsymbol{l}_\beta)$ is then determined by the mixed derivative of the electrostatic energy V_{AB} with respect the LM's $\boldsymbol{l}_\alpha$ and $\boldsymbol{l}_\beta$, supported by two different molecules A and B. Differentiating Eq. (1.38) with respect to local modes, leads to four terms which can be recasted as a sum of two contributions:

$$k_{AB}^{TDC-PCM}(\boldsymbol{l}_\alpha, \boldsymbol{l}_\beta) = k_{AB}^{direct}(\boldsymbol{l}_\alpha, \boldsymbol{l}_\beta) + k_{AB}^{explicit}(\boldsymbol{l}_\alpha, \boldsymbol{l}_\beta) \quad (1.42)$$

where

$$k_{AB}^{direct}(\boldsymbol{l}_\alpha, \boldsymbol{l}_\beta) = \left[\int\int \frac{\rho_A^\alpha(\boldsymbol{l}_\alpha, r_i)\,\rho_B^\beta(\boldsymbol{l}_\beta, r_j)}{|\mathbf{r}_i - \mathbf{r}_j|} d\mathbf{r}_i d\mathbf{r}_j\right]_{Q_\alpha=0, Q_\beta=0} \quad (1.43)$$

and

$$k_{AB}^{explicit}(\boldsymbol{l}_\alpha, \boldsymbol{l}_\beta) = \left[\int\int_\Sigma \frac{\sigma_A^\alpha(\boldsymbol{l}_\alpha, \mathbf{r}_i)\,\rho_B^\beta(\boldsymbol{l}_\beta, \mathbf{r}_j)}{|\mathbf{r}_i - \mathbf{r}_j|} d\mathbf{r}_i d\mathbf{s}_j\right]_{Q_\alpha=0, Q_\beta=0} \quad (1.44)$$

where the upper indexes denote partial derivative of the corresponding charge distributions with respect to the LM's. In deriving Eqs. (1.43-1.44) we have assumed that the charge densities of the two oscillators are non-overlapping and that the charge density of each unit is independent of the nuclear displacements in the other unit. This assumption implies that the cavity or cavities have a fixed geometry,

independently of the displacement coordinates of the two oscillators.

If the oscillators are separated by distances much larger than their size, a dipolar approximation can be introduced to describe the electrostatic interactions determining the vibrational coupling. The vibrational coupling may then be written as:

$$k^{TDC-PCM}\left(\boldsymbol{l}_{\alpha}, \boldsymbol{l}_{\beta}\right) = \boldsymbol{\mu}_{A}^{\alpha} \cdot \mathbf{E}_{B}^{\beta} \tag{1.45}$$

where μ_A^{α}, the transition dipole moment and $\mathbf{E}_B^{\beta}$ is the total electric field due to the other oscillator, namely

$$\mathbf{E}_{B}^{\beta} = \mathbf{E}_{B}^{\mu_B^{\beta}} + \mathbf{E}_{B}^{\sigma_B^{\beta}} \tag{1.46}$$

where $\mathbf{E}_j^{\mu_B^{\beta}}$ is the electric field produced by the transition dipole moment μ_B^{β}

$$\mathbf{E}_{B}^{\mu_B^{\beta}}(\mathbf{r}) = \mathbf{T}_{AB} \cdot \boldsymbol{\mu}_{B}^{\beta} \tag{1.47}$$

and $\mathbf{E}_j^{\sigma_j}$ is the electric field produced by the differentiated charge distribution,

$$\mathbf{E}_{B}^{\sigma_\beta}(\mathbf{r}) = -\nabla \int_{\Sigma} \frac{\sigma_{B}^{\beta}(\mathbf{r}')}{|\mathbf{r} - \mathbf{r}'|} d\mathbf{r}' \tag{1.48}$$

where $\mathbf{T}_{ij}$ is the dipole interaction tensor, given by $\mathbf{T}_{ij} = \frac{3\mathbf{r}_{ij} \cdot \mathbf{r}_{ij} - r_{ij}^2 \mathbf{I}}{r_{ij}^5}$ ($\mathbf{r}_{ij} = \mathbf{r}_i - \mathbf{r}_j$ is the distance vector of length r_{ij} between the two dipoles), $\mathbf{I}$ is a unit tensor and ∇ is the gradient operator with respect the components of the position vector $\mathbf{r}$.

In the computational practice, the apparent surface charge distribution is discretized into a set of apparent point charges $\{q_{B,i}^{\beta}\}$ spread on the surface of the cavity and the electric field may be written as

$$\mathbf{E}_{B}^{\sigma_\beta}(\mathbf{r}) = -\nabla \sum_{i} \frac{q_{B}^{\beta}(\mathbf{s}_i)}{\mathbf{r} - \mathbf{s}_i} \tag{1.49}$$

where $\mathbf{s}_i$ is the position vector of the i-Th charge and the summation runs over all the apparent charges.

As reported in section 1.1.1, the apparent point charges $q_{B,i}^{\beta}$ are obtained as solution of the matrix equation

$$\mathbf{q}_B^\beta = \mathbf{Q}\mathbf{V}(\rho_B^\beta) \tag{1.50}$$

where $\mathbf{q}_B^\beta$ is a column vector collecting the apparent charges, $\mathbf{V}(\rho_B^\beta)$ is a column vector containing the electrostatic potential produced by the molecular charge distribution, ρ_B^β, at the location of the apparent charges, and $\mathbf{Q}$ is the PCM response matrix (see Eq. 1.8).

To summarize, in the TDC-PCM model the vibrational coupling $k_{\mathrm{AB}}^{\mathrm{TDC\text{-}PCM}}(\boldsymbol{l}_\alpha, \boldsymbol{l}_\beta)$ is a sum of two contributions:

$$k_{AB}^{direct}(\boldsymbol{l}_\alpha, \boldsymbol{l}_\beta) = \boldsymbol{\mu}_A^\alpha \cdot \boldsymbol{E}^{\mu_B^\beta} = \boldsymbol{\mu}_A^\alpha \cdot \tilde{\boldsymbol{T}}_{AB} \cdot \boldsymbol{\mu}_B^\beta = \frac{\boldsymbol{\mu}_A^\alpha \cdot \boldsymbol{\mu}_B^\beta - 3\left(\boldsymbol{\mu}_A^\alpha \cdot \mathbf{r}_{AB}\right)\left(\boldsymbol{\mu}_B^\beta \cdot \mathbf{r}_{AB}\right)}{r_{AB}^3} \tag{1.51}$$

$$k_{AB}^{explicit}(\boldsymbol{l}_\alpha, \boldsymbol{l}_\beta) = \boldsymbol{\mu}_A^\alpha \cdot \boldsymbol{E}^{\sigma_B^\beta} = \boldsymbol{\mu}_A^\alpha \cdot \int_\Sigma \sigma_B^\beta(\mathbf{r}') \frac{\mathbf{r} - \mathbf{r}'}{|\mathbf{r} - \mathbf{r}'|^3} d\mathbf{r}' \approx \boldsymbol{\mu}_A^\alpha \cdot \sum_k q_B^\beta(\mathbf{s}_k) \frac{\mathbf{r} - \mathbf{s}_k}{|\mathbf{r} - \mathbf{s}_k|^3} \tag{1.52}$$

where the former is the simple bare dipole-dipole interaction as in TDC [28, 35] method, whereas the latter is the interaction mediated by the medium.

1.3.1.1 Calculation of the transition dipoles and charges

The molecular quantities involved in the TDC-PCM equations can be determined by performing a QM calculation of LM's for the solvated monomers A and B, and extracting the derivatives of the molecular charge density distribution with respect the LM of interest. For each monomer the PCM calculation of the molecular Hessian is performed using the dimeric cavity, at the corresponding equilibrium geometry. The calculations must be performed within the fixed cavity approximation and using a non-equilibrium solvation regime.

The computed derivatives of the molecular charge densities are expressed in terms of the derivative of the one-particle density matrix $\mathbf{P}^x$, associated to the chosen basis set used for the expansion of the molecular orbitals of the QM calculation.

The density matrix $\mathbf{P}^x$ is then used to compute the corresponding transition dipole moments and the derivative of the apparent charges. The transition dipoles $\boldsymbol{\mu}_A^\alpha$ is given by:

$$\boldsymbol{\mu}_{\{A,r\}}^{\alpha} = Tr\left(\mathbf{P}_A^\alpha \mathbf{M}_r\right) \tag{1.53}$$

where $\boldsymbol{P}_A^\alpha$ is the derivative of the density matrix of monomer A with respect to its local mode α, $\mathbf{M}_r$ is the matrix corresponding to the r-Th component of the electric dipole operator expressed in the basis set. A corresponding expression involving the monomers B holds for $\boldsymbol{\mu}_{\{B,r\}}^{\beta}$.

The transition charges $q_{B,i}^{\beta}$ are obtained using Eq. (1.49) and the the electrostatic potential $V(\rho_B^\beta)$ given by:

$$V_{\{B,i\}}^{\beta} = tr\mathbf{P}_B^\beta \mathbf{V}(i) \tag{1.54}$$

where $\boldsymbol{P}_B^\beta$ is the derivative of the density matrix of monomer B with respect to its local mode β, $\mathbf{V}(i)$ is the matrix corresponding to component of the electrostatic potential operator at the position of the i-Th apparent charges. To take into account the non-equilibrium solvation regime, the solvent response matrix of Eq. (1.50) must be evaluated using the optical dielectric constant of the solvent (ϵ_∞).

1.3.2 Hessian Matrix Reconstruction within the framework of PCM (HMR-PCM)

In this section we consider the more accurate HMR-PCM approach to study the vibrational couplings. The basic formulation of the HMR requires an harmonic QM calculation of the vibrational local modes and the vibrational normal modes of the full system. Thus, the normal modes of the target system are redefined in terms of vibrational modes, so that the inter-mode vibrational coupling can be computed. In this approach solvent effects are obtained by reformulating vibrational calculations for a solvated system, i.e. in presence of an external dielectric medium mimicking the solvent. [36,37] Thus in HMR-PCM approach the effects of the solvent are implicitly accounted for by calculating normal modes and frequencies for the solvated system

as well as by redefining the local modes in solution.

In the HMR-PCM approach the vibrational coupling is calculated by assuming that the NM's of the full system (Q_i) can be approximately related to LM's (l_i) by a unitary transformation. [26]

$$\begin{pmatrix} \mathbf{Q}_1 \\ \mathbf{Q}_2 \end{pmatrix} \backsimeq \mathbf{U} \begin{pmatrix} \mathbf{l}_1 \\ \mathbf{l}_2 \end{pmatrix} \tag{1.55}$$

All the modes are given as $3N$-components vectors of atomic mass weighted Cartesian displacements (N is the number of atoms). The LM's can be obtained:

- cutting the full system in smaller parts into which the local vibrations are localized and using the NM's of these smaller parts to obtain the LM's. [26] This approach is applied in Section 2.1.

- dividing the full system into smaller parts in which the local vibrations are localized, using the PHVA to obtain the LM's. This improved computational strategy based on the combination of the HMR-PCM and Partial Hessian Vibrational Analysis (PHVA, see appendix A), used to obtain accurate vibrational LM's, was developed in my PhD work. This approach is applied in Section 2.2.

It is worth remembering that an accurate modelling of the LM's is crucial to give an accurate modelling of the vibrational couplings.

Using the same transformation of Eq. (1.55), the vibration couplings (β) can be obtained from the NM's frequencies (ω_i) through: [28, 38]

$$\begin{pmatrix} \epsilon_1 & \beta \\ \beta & \epsilon_2 \end{pmatrix} = \mathbf{U}^{-1} \begin{pmatrix} \omega_1 & 0 \\ 0 & \omega_2 \end{pmatrix} \mathbf{U} \tag{1.56}$$

The transformation matrix $\mathbf{U}$ can be given by:

$$\mathbf{U} = \begin{pmatrix} cos\theta & sin\theta \\ -sin\theta & cos\theta \end{pmatrix} \tag{1.57}$$

where the transformation angle (θ) is: [26]

$$\theta = \frac{\theta_1 + \theta_2}{2} = \frac{arctan\left(\frac{\boldsymbol{Q}_1 \cdot \boldsymbol{l}_2}{\boldsymbol{Q}_1 \cdot \boldsymbol{l}_1}\right) + arctan\left(\frac{\boldsymbol{Q}_2 \cdot \boldsymbol{l}_1}{\boldsymbol{Q}_1 \cdot \boldsymbol{l}_1}\right)}{2} \tag{1.58}$$

To summarize, using the former transformation matrix, the following relation between NM's and LM's can be found:

$$\begin{pmatrix} \epsilon_1 & \beta \\ \beta & \epsilon_2 \end{pmatrix} = \begin{pmatrix} cos\theta & sin\theta \\ -sin\theta & cos\theta \end{pmatrix}^{-1} \begin{pmatrix} \omega_1 & 0 \\ 0 & \omega_2 \end{pmatrix} \begin{pmatrix} cos\theta & sin\theta \\ -sin\theta & cos\theta \end{pmatrix} \tag{1.59}$$

This gives the following expression for the vibrational couplings:

$$\beta = \frac{1}{2}(\omega_1 - \omega_2)\sin(2\theta) \tag{1.60}$$

Chapter 2

Two-dimensional infrared (2D-IR) spectroscopic responses

This Chapter deals with the modelling of environment effects on two-dimensional infrared (2D-IR) spectroscopic responses. In particular we focus on vibrational couplings between amide modes in peptides (Section 2.1) and between carbonyl vibrations in base pairs of nucleic acids (Section 2.2).

2.1 Vibrational couplings between amide modes in peptides

This Section presents and discusses two different applications, namely the HMR-PCM and TDC-PCM approaches (described in Section 1.3) to a model system constituted by a formaldehyde dimer. Then the PCM-HMR model is applied to the evaluation of the vibrational couplings between amide modes in (s)-N-methyl acetylproline amide (NMAP).

As shown in Section 1.3, in the HMR-PCM method the solvent effects are taken into account in terms of changes of its normal modes and vibrational frequencies, due to the presence of the solvent; on the other hand, TDC-PCM method relies instead on the evaluation of the vibrational transition dipoles of the local modes in the presence of the solvent, and then explicitly includes medium screening effects

on the Coulombic interaction between the transition dipoles. Due to its intrinsic limitations, the TDC method is not quantitatively reliable and is only suitable to model the vibrational coupling of weak interacting systems, whereas the more reliable HMR-PCM method can be applied to study complex molecular systems both in vacuo and solution.

The application of the 2D-IR spectroscopy to peptide systems is particularly interesting because of the little knowledge on the interactions between amide vibrations. In this study we only consider amide vibrations I and II, [39] since they are by far the most commonly used for structural analysis (a list of the amide vibrations is reported in Table 2.1).

Amide	Description	Frequency (cm^{-1})
A	NH str.	∼3300
B	NH str.	∼3200
I	CO str.	∼1600-1700
II	NH bend, CN str.	∼1500-1600
III	NH bend	∼1200-1400
IV	OCN bend	∼630-770
V	NH bend	∼650-800
VI	CO bend	∼540-600
VII	Skeletral torsion	∼200
S	$C_\alpha H$ bend	∼1400

Table 2.1: Characteristic infrared amide vibrational frequency [40–42].

2.1.1 Computational Details

All structures were optimized at the DFT level using the B3LYP hybrid functional [43] with the 6-31G(d) basis set for formaldehyde and the 6-311++G(d,p) basis set for NMAP, both in vacuo and solution. Solvent effects were described by exploiting the IEF-PCM (see Subsection 1.1.1) as implemented in the Gaussian03 code (G03). [44] Extension of PCM to the TDC model has been implemented in a locally modified version of the same code. The PCM molecular cavities surrounding the molecular solutes were built by interlocking spheres. For formaldehyde dimers, the calculations were performed by using for each monomer both a single sphere placed on the carbon atom, with radius [45] R_{sph}=3.0Å, or a PCM cavity made of four spheres placed on each atom with radii R_C=1.925Å , R_O=1.75Å, R_H=1.2Å

(see Figure 2.1). For NMAP the cavity was built by using a molecular cavity made of 13 interlocking spheres according with an analogue choice reported in ref. [46] (R_C=1.925Å, R_O=1.75Å, R_N=1.83Å, $R_{H,amide}$=1.2Å, R_{CH}=2.125Å, R_{CH_2}=2.325Å and R_{CH_3}=2.525Å). In the following applications, we have analyzed three different solvents, an apolar one for the case of formaldehyde dimer and a medium and a highly polar one for NMAP; the corresponding dielectric constants used are those of cyclohexane ($\varepsilon = 2.0$), DCM, and water ($\varepsilon = 8.9$ and 78.4), respectively.

In the case of NMAP, free energies and Boltzmann populations of the various conformers were obtained by including zeropoint and thermal contributions (at 298 K). The same quantities in solvent were obtained by further including nonelectrostatic (repulsion, dispersion, and cavitation) energy contributions. [47]

To apply the HMR approach to NMAP, the amide-I (amide end) and amide-II local modes were represented by the elements of the carbonyl carbon and oxygen atoms and the amino nitrogen and hydrogen atoms in the acetamide ($CH_3 - CO - NH_2$) normal modes, whereas the amide-I (acetyl end) local mode was represented by the elements of the carbonyl carbon and oxygen atoms in the N-methylacetamide normal modes.

2.1.2 Results and Discussion

2.1.2.1 PCM-TDC vs PCM-HMR: A performance comparison on formaldehyde dimers

Here we show the performance of the TDC-PCM with respect to the more complete HMR-PCM method and to benchmark it with respect to the Onsager solvation approach, for which an analytical formulation of the solvent effect on the coupling can be defined. A very simple system formed by two interacting C=O stretching modes placed on two different formaldehyde units is considered. Two different spatial arrangements are considered, i.e., head-to-tail and face-to-face dimers (see Figure 2.1), both with variable r distance between the medium points of the C=O bond. In Table 2.2, force constants for head-to-tail and face-to-face formaldehyde dimers in vacuum and in cyclohexane are reported as a function of the r distance.

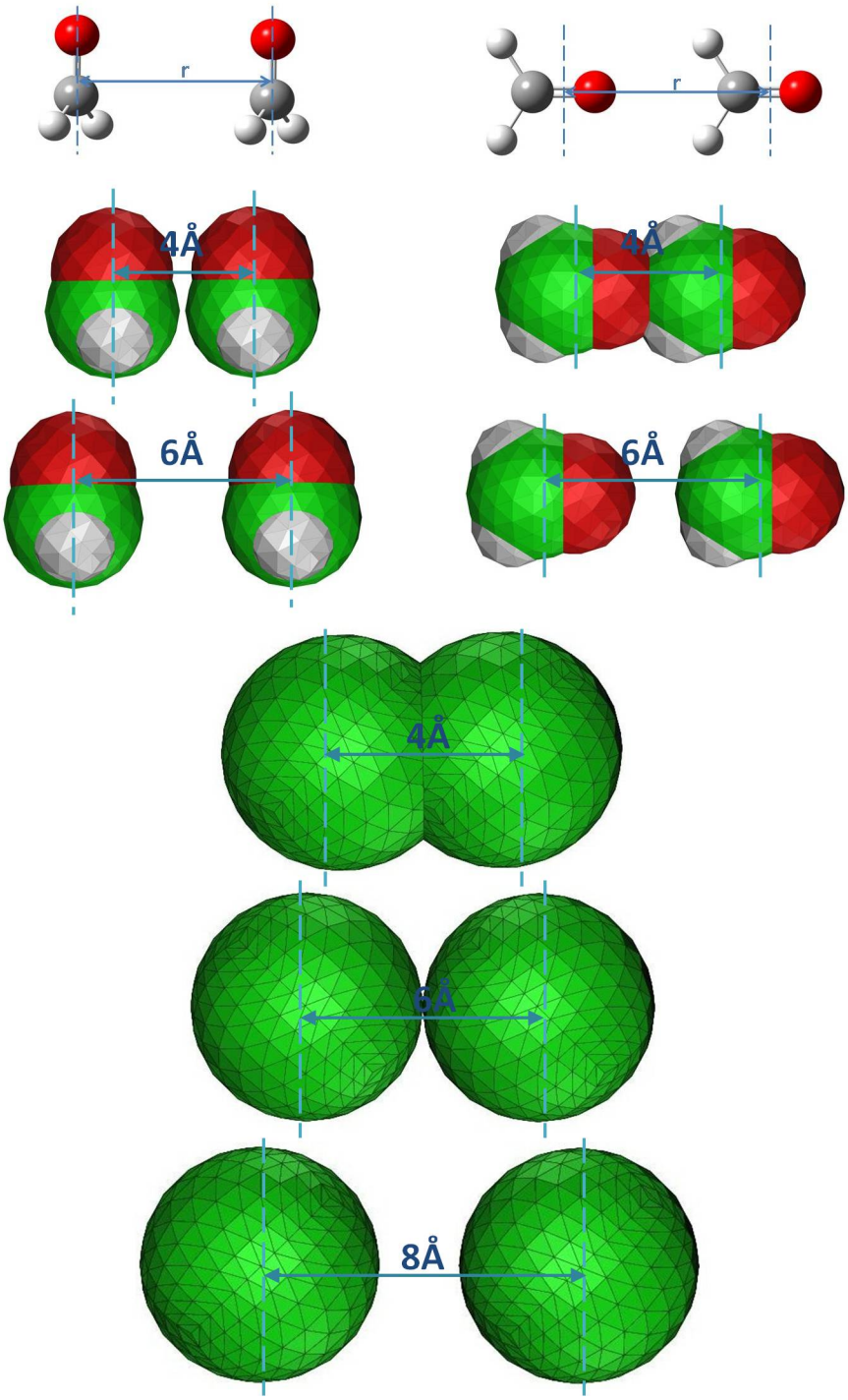

Figure 2.1: Scheme of the face-to-face (left) and head-to-tail (right) formaldehyde dimers. The corresponding spherical and molecular PCM cavities are also shown.

Dimer	r	$k^{\text{HMR}}_{\text{vacuum}}$	$k^{\text{TDC}}_{\text{vacuum}}$	$k^{\text{HMR-PCM}}_{\text{sphere}}$	$k^{\text{TDC-PCM}}_{\text{sphere}}$	$k^{\text{HMR-PCM}}_{\text{mol.cavity}}$	$k^{\text{TDC-PCM}}_{\text{mol.cavity}}$
head-to-tail	4	2.83	7.30	2.85	7.60 (7.94)	1.79	7.10 (9.24)
	6	1.65	2.16	1.29	1.81 (2.40)	1.31	1.86 (2.78)
	8	0.79	0.91	0.64	0.75 (1.02)	0.65	0.77 (1.17)
	12	0.25	0.27	0.10	0.22 (0.30)	0.20	0.26 (0.35)
	16	0.11	0.11	0.04	0.09 (0.13)	0.08	0.11 (0.15)
face-to-face	4	4.57	3.65	3.86	3.03 (4.06)	3.83	3.33 (4.67)
	6	1.12	1.08	0.88	0.87 (1.20)	0.91	0.94 (1.39)
	8	0.47	0.46	0.38	0.37 (0.51)	0.36	0.39 (0.59)
	12	0.14	0.13	0.11	0.11 (0.15)	0.10	0.13 (0.17)
	16	0.06	0.06	0.05	0.05 (0.06)	0.04	0.05 (0.07)

Table 2.2: Coupling Force Constant k_{AB} (10^3 mdyne $\text{Å}^{-1}\text{am}u^{-1}$) between the Carbonyl Stretching Modes of the Formaldehyde Dimers, obtained using HMR and TDC in gas phase and in cyclohexane as a function of the intermolecular distance (r, in Å). For the TDC-PCM approach, the direct component (see Eq. 2.1) is also shown in parentheses.

Looking first at the gas-phase data, it appears that TDC and HMR results are quite different for distances smaller than 12Å with TDC overestimating and underestimating the couplings in the head-to-tail and the face-to-fact orientations, respectively. Such a behaviour is not unexpected, because the approximation of the two oscillators as a pair of point transition dipoles becomes reasonable only at large distances with respect to the molecular size. Moving to solvated dimers, the analysis becomes more complex as this intrinsic limit of the TDC approach couples with the solvent polarization effect, which acts both on the magnitude of the transition dipoles and on their interaction. From the data reported in Table 2.2, we can dissect these two effects by comparing the gas phase k_{TDC} with the direct component and the total value of the $k_{\text{TDC-PCM}}$. As it can be seen from the values of the direct component (given in Table 2.2 in parentheses), the solvent induces a net amplification of the transition dipoles, which would lead to a ca. 30% increase of the dipole-dipole interaction. However, the inclusion of the screening effect completely changes this behavior, leading to a decrease of the total coupling of less than 5% for the head-totail and less than 10% for the face-to-face orientation. In order to get better insight into solvent effects, it is convenient to define a solvent screening factor as

$$s^{\mathrm{PCM}} = \frac{k^{\mathrm{PCM}}}{k^{\mathrm{direct}}} \tag{2.1}$$

In Figure 2.2, we report the distance dependence of s for the TDC-PCM in comparison with the screening factor predicted by the Onsager ($s^{\mathrm{Onsager}} = \frac{9\varepsilon}{(2\varepsilon+1)^2}$) and the Förster [48] approaches ($s^{\mathrm{Forster}} = \frac{1}{\varepsilon}$). For this analysis, two sets of PCM results are reported, the ones obtained from the values reported in Table 2.2 and the ones obtained in the case of spherical cavities. As expected, s^{PCM} is a function of the dimer orientation and distance, and it converges to the Onsager factor only at large distances. In the case of spherical cavities, the short-distance discrepancy found for the head-to-tail orientation with respect to the Onsager prediction can easily be explained by noting that at $r = 4$Å the two spheres slightly overlap and, as a result, the interaction between the transition dipoles is less screened (s is closer to one) than at larger distances, for which the two spheres are separated.

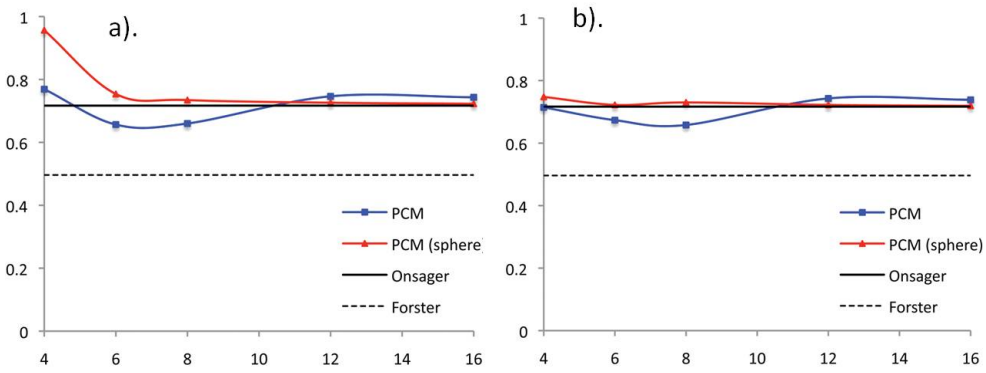

Figure 2.2: Screening factor (see text) in the formaldehyde dimers as a function of the r distance (in Å) for the head-to-tail orientation (left panel) and the face-to-face orientation (right panel).

2.1.2.2 Vibrational Coupling Between Amide Modes in N-Methyl Acetyl-proline Amide (NMAP)

In this Section we analyze the vibrational coupling for trans NMAP in aqueous and DCM solutions. The choice of this dipeptide is based on previous studies, [46] which have shown that PCM is able to give a reliable description of its conformational effects and several spectroscopic properties in water, such as vibrational frequencies,

	C_7	3_{10} helix I	P_{II}
gas phase	99	1	-
CH_2Cl_2	17	29	54
water	4	28	68

Table 2.3: Calculated Boltzmann Populations (%) of the Various Conformers of NMAP in Gas Phase, Water, and DCM

IR/VCD, Raman/VROA, UV/CD spectra, ORD, and NMR.

In order to get a reliable description of spectroscopic properties of systems exhibiting different conformations, not only it is crucial to get an accurate description of the properties but also to correctly predict the relative populations of different conformers. In particular, for NMAP it has been shown, [46] that only 3_{10} helix I and C_7 are stable minima in the gas phase, whereas in water three structures, i.e., 3_{10} helix I, P_{II} and C_7, coexist with different conformational weights. The populations of the most relevant stable conformations calculated in the previous paper for the gas phase and water are reported in Table 2.3, together with newly obtained values in DCM, whereas in Figure 2.3, we report the structure of the three possible conformers together with indication of the dihedral angles which identify them.

	(ϕ, ψ)		
	C_7	3_{10} helix I	P_{II}
gas phase	-81,77	-76,-13	-
CH_2Cl_2	-82,74	-72,-24	-62,144
water	-82,74	-68,-28	-62,146

Table 2.4: Dihedral angle values (in Degrees) for the optimized structures of NMAP in dichloromethane and water, with PCM and in vacuo. The calculated dihedral angle in vacuo and in water are taken from Ref. [46].

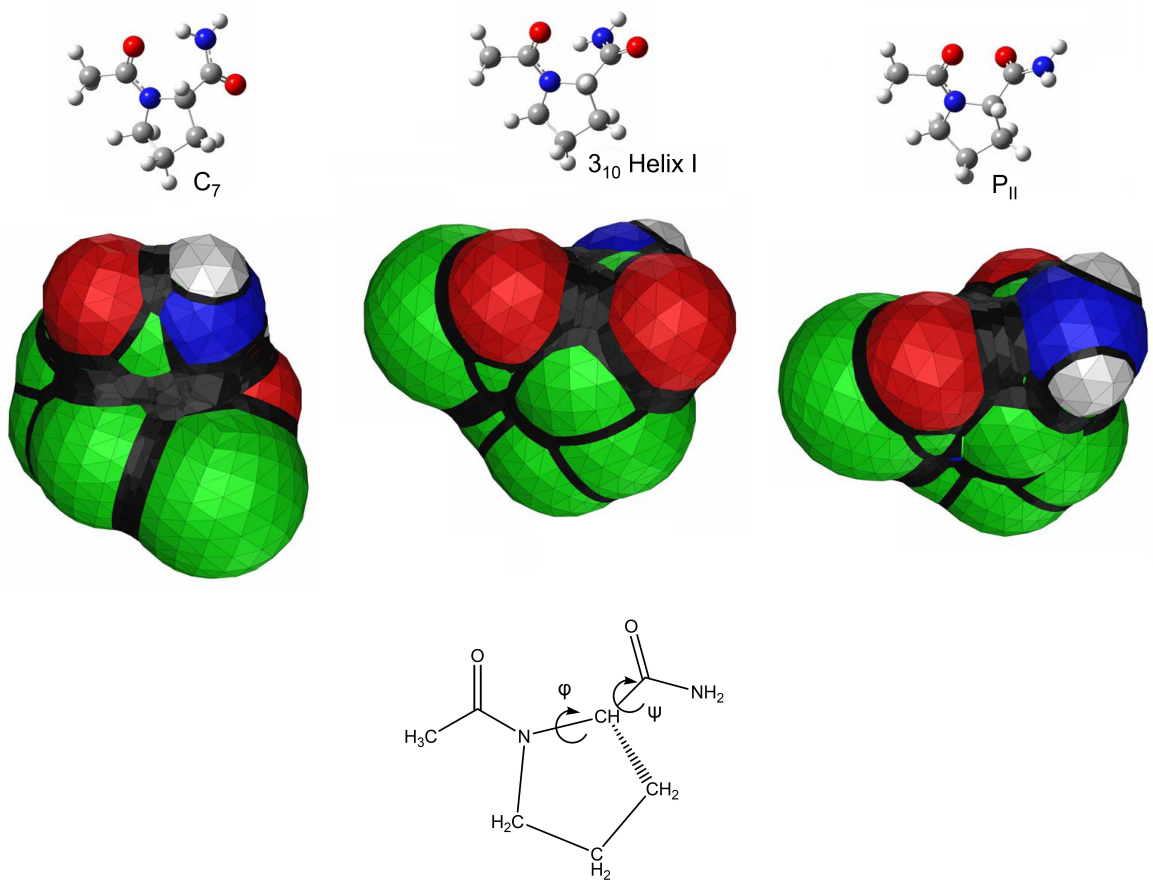

Figure 2.3: Structures for the three most stable NMAP conformers. The PCM cavities are also shown.

As reported in Table 2.3, results in DCM are in between gas phase and water; in fact, in the gas phase only the C_7 conformation is substantially populated, whereas in water, the P_{II} conformer, unstable in vacuo, is the dominant species, with only a small amount of 3_{10} and an almost negligible quantity of C_7 . In DCM an intermediate situation is reported, being P_{II} still prevalent (54%) but with 3_{10} roughly one-half of the P_{II}, and C_7 no longer negligible (17%).

Such a different picture in the three environments, together with the different values of the coupling of the conformers in each environment, causes quite dissimilar average β values in the various media reported in Table 2.5 for amide-I-amide-I, Amide-I (Ac)-Amide II, and amide-I (Am)-Amide II. In the same table we also report the corresponding vibrational couplings in vacuo, DCM, and water for the most relevant NMAP conformations. "Ac" and "Am" in the tables refer to the acetyl and amide end, respectively. Due to the near proximity of "vibrational oscillators", only

the HMR method has been applied. In fact, for highly interacting chromophores, the dipole-dipole interaction is clearly not reliable as shown also in the previous section. The use of the HMR method, in fact, makes the resulting couplings account for both through-space and through-bond interactions. The latter should be very large for amide-amide coupling, due to the proximity of the groups involved, in some cases also bonded to each other. As expected, coupling values are strongly dependent upon the molecular conformation exactly as the angles between transition dipoles (see Table 2.5), which are, together with β couplings, another outcome of 2DIR experiments. The 2DIR spectra of NMAP in DCM have been reported by Rubtsov and Hochstrasser, [49] who studied energy transfer pathways between amide modes. In Table 2.5, a comparison between calculated average data in DCM and experiments is reported.

Conformation			
	gas phase	CH_2Cl_2	water
	Amide I (Ac) -Amide I (Am)		
C_7	10.7 (38)	8.2 (33)	9.1 (30)
3_{10}	0.7 (108)	2.2 (114)	2.5 (116)
P_{II}	-	6.0 (68)	7.0 (70)
average	10.6 (39)	5.3 (76)	5.8 (81)
exp [49]	-	10 (44 - 56)	-
	Amide I (Ac)-Amide II (Am)		
C_7	19.3 (33)	18.1 (31)	17.5 (32)
3_{10}	8.0 (71)	11.1 (87)	11.0 (92)
P_{II}	-	2.6 (43)	3.1 (49)
average	19.2 (33)	7.8 (54)	5.9 (60)
exp [49]	-	19 (35 - 34)	-
	Amide I (Am)-Amide II (Am)		
C_7	25.8 (66)	20.7 (57)	20.0 (55)
3_{10}	30.4 (75)	21.7 (64)	18.5 (60)
P_{II}	-	20.7 (64)	18.2 (66)
average	25.9 (66)	21.0 (63)	18.4 (64)
exp [49]	-	30 - 32 (52 - 66)	-

Table 2.5: Vibrational couplings (β) and angles (θ, in parentheses) between amide modes of NMAP in gas-phase, in water and in dichloromethane. The Comparison between Calculated and Experimental value of NMAP in DCM are also shown. (Vibrational couplings in cm^{-1}, angles in degrees)

In general, a good reproduction of experimental findings is shown for both cou-

plings and angles. In more details, couplings are always slightly underestimated with respect to experiments. By analyzing this result together with the data of the single conformers (Table 2.5), it becomes evident that such an underestimation is a consequence of the underestimation of the population of the C_7 conformer. Exactly the same applies to angles between transition moments. Indeed the study of conformational stability in solvents of low to medium polarity, as DCM, using a continuum solvation model can be more delicate than in highly polar solvents like water. In fact, in DCM, a delicate balance between electrostatic and nonelectrostatic effects applies, which finally leads to free energy differences between the conformers below 0.8 kcal/mol at room temperature. These values are of about the same order of magnitude as the accuracy of the model.

2.2 Vibrational couplings between carbonyl vibrations in DNA

This Section focuses on the application of the HMR-PCM method to the study the vibrational coupling between carbonyl vibrations in DNA.

It is well known that infrared techniques are very sensitive to the structure of the polynucleotide helix since DNA bases change their vibrational properties in a unique way, due to vibrational couplings and environment effects. An accurate modelling of molecular vibrations and vibrational couplings is a key factor in order to correlate the change of couplings to structural modifications; [50] in the case of DNA, this is fundamental, for instance, to develop more efficient DNA-binding drugs. [51, 52]

QM calculations of the vibrational coupling in DNA oligomers have been performed by Zanni et al. [53] and by Lee et al. [54–57] adopting different computational strategies. In particular, Zanni et al. have studied the vibrational coupling between normal modes involving carbonyl stretching in Watson-Crick (WC) base pairs guanine (G) and cytosine (C) and between nearest-neighbour bases G and C, in two different DNA oligomers. QM calculations were performed on isolated G and C bases, by neglecting the deoxyribose and phosphate groups to reduce the computational costs, and the vibrational coupling was obtained by using the electrostatic

TDC and a finite difference evaluation of the PES curvature. In particular, for the vibrational coupling between the Watson–Crick base pairs, a single pair was used as model, while for the evaluation of the vibrational coupling between nearest neighbour bases G and C, two stacked base pairs were considered. The vibrational coupling for the same DNA oligomers has also been studied by Lee et al. [54], by performing QM calculations on G and C using a modified HMR method.

The consideration of the local environment has been reported as crucial in order to realistically describe vibrational couplings in solution, principally because the interaction with the environment modifies both the single local vibrations and the coupling between them. Similarly to the study reported in the previous Subsection on amide vibrational couplings in small peptides, here we apply a computational strategy still based on the PCM combined with the HMR method and Partial Hessian Vibrational Approach (PHVA) (see appendix A) to evaluate inter- and intra-layer couplings between hydrogen bonded and stacked DNA base pairs. In particular, the coupling between carbonyl vibrations located on G and C bases will be considered in the case of a A-form DNA of well known structure, resolved with X-ray crystallography. [58]

2.2.1 Modeling DNA oligomers

In this study we have investigated a sequence of guanine and cytosine in the double stranded helix DNA d(G_nC_n). In particular, we have used the structure of the DNA oligomer d(G_4C_4) determined by McCall et al. [58] by single-crystal X-ray methods (PDB ID: 2ANA). In the structure, there are two strands in the asymmetric unit, and these coil about each other to form a right-handed A-type double-helix with Watson-Crick hydrogen bonds between base-pairs. The two d(G-G-G-G)·d(C-C-C-C) segments in the oligomer exhibit similar and uniform structures (see Figure 2.4).

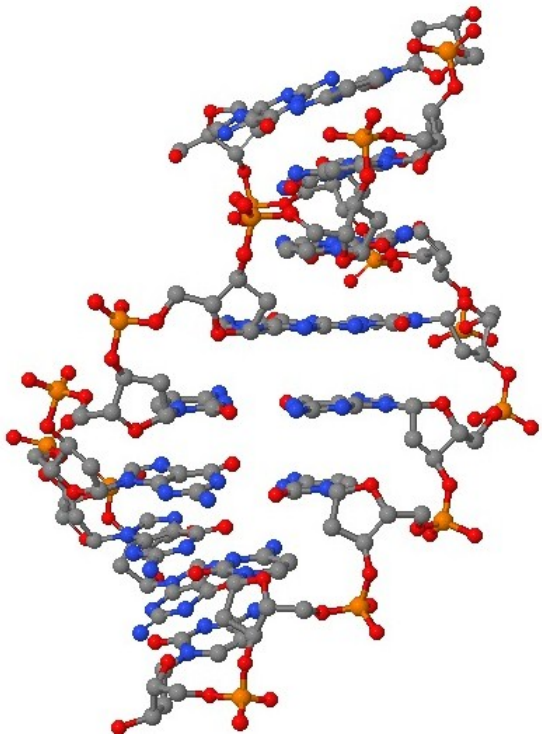

Figure 2.4: Structure of the DNA oligomer investigated in this study. From this experimental structure five different coupled bases were extracted, that from now on will be indicated as fragments 1-5.

From this experimental structure five different clusters were extracted, containing the coupled bases, that from now on will be indicated as fragments 1-5. The borders of the helix were not considered.

To introduce the effect of the rest of DNA, two different models were used. In the first model (referred to as PCM) the environment was represented as a continuum dielectric, while in the second model (cluster) the adjacent base pairs were explicitly included in the QM calculation. More in details, for the H-bonded (HB) pairs two additional base pairs were considered, while for the stacked pairs four additional base pairs were included (see Figure 2.5).

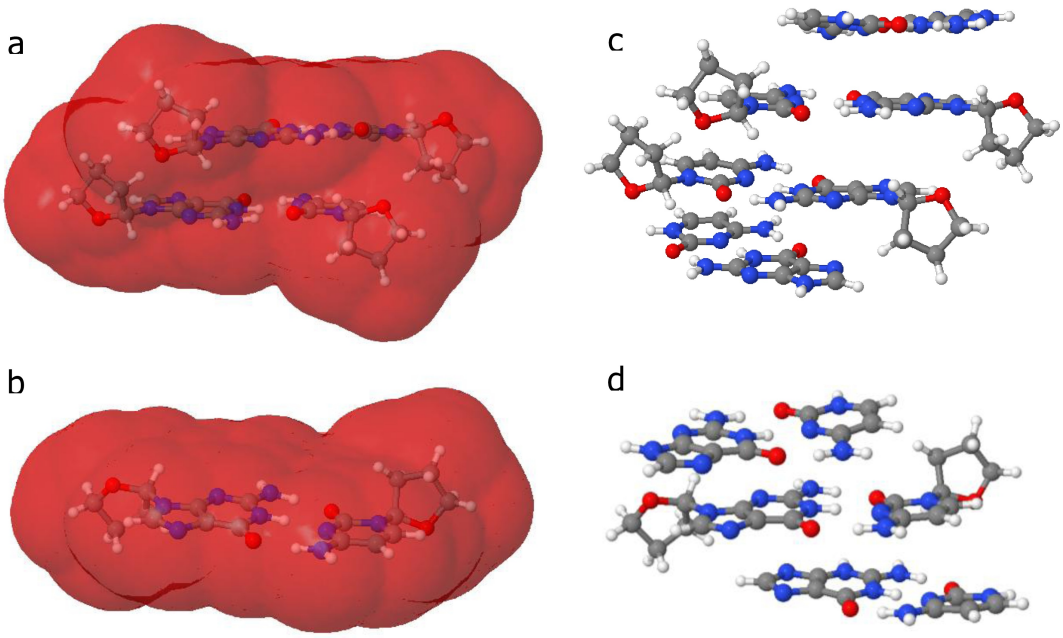

Figure 2.5: Representations of the stacked and HB fragments within the PCM (a and b) and the explicitly included adjacent base pairs (c and d), respectively.

2.2.2 Methodologies

As pointed out by Lee and Cho, [54] the application of the HMR approach to the study of coupled vibrations localised on base pairs presents critical points, due to the high delocalization of the vibrational modes. To overcome these critical points, we have combined the HMR approach with the PHVA. [59–64] The PHVA is used both to perform the vibrational calculation on the coupled Hydrogen-Bonded (HB) and stacked pairs and to localize the vibrational modes on each single basis. As presented in Appendix A, the system is divided into a freely vibrating and a frozen part, which does not directly contribute to the normal mode of the vibrating one. In agreement with the one-bond-distance rule [65] more than one bonds between the freely vibrating (the bases) and the fixed part (the furanoses and the adjacent base pairs in the cluster model) have been left in order not to bring the two parts too close (see Figure 2.6). The calculation of the vibrational coupling between two local modes located on different base pairs, consists of the following steps:

1. Normal Modes calculation of the single uncoupled basis in the presence of the others kept frozen, using the PHVA. These are the local modes of the uncoupled basis, which are used as a basis for the determination of the vibrational coupling.

2. Normal Modes calculation of the coupled pair (possibly in the presence of the other bases kept frozen, using the PHVA). These are the normal modes of the coupled pair.

3. Application of the HMR using the results of the coupled and the uncoupled calculations to determine the vibrational coupling between the local vibrations.

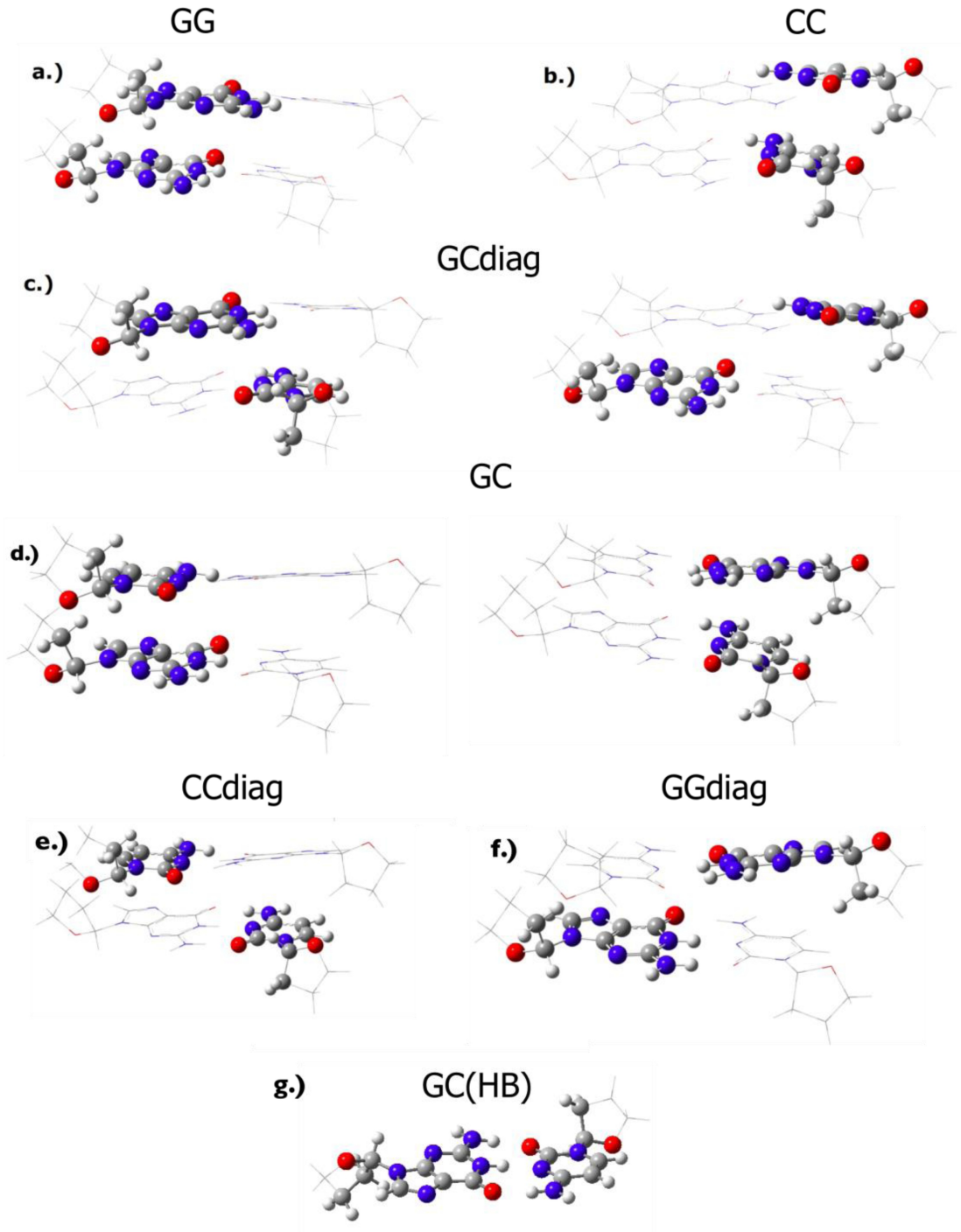

Figure 2.6: Representations of the stacked (a-f) and HB fragments (g). The freely vibrating atoms are represented in "Ball & Stick", whereas the frozen atoms are shown in "wireframe". The systems (a-d) are obtained from the fragments 1,2,4,5 ; whereas the systems represented in (e-f) are obtained from the fragment 3.

2.2.3 Computational details

All calculations were performed by using the Gaussian 09 package, [66] by employing DFT and using the M06-2X functional. [67] This functional was chosen for its ability to describe non-covalent interactions. [68,69] To describe the continuum environment the IEF-PCM (see Section 1.1.1) was used. PCM cavities were built as a series of interlocking spheres centred on the atoms. Two different set of radii were tested: the UFF radii (all multiplied by cavity size factor of 1.1), which are the Gaussian 09 default settings (from now on indicated as StCav), and a set of enlarged radii (employing a cavity size factor of 1.7) so to take into account void space around the base pairs in the DNA double helix (from now on indicated as LCav). In the particular case of the PCM calculations for the fragments, in order to consider the possibility that in a DNA double helix the volume between the base pairs cannot be accessible to solvent, a larger radius (equal to that of the Carbon atom) was used for the hydrogen atoms involved in hydrogen bonds between base pairs. Two different values of the dielectric permittivity were tested, corresponding to a weakly polar ($\varepsilon = 6$) and an non polar ($\varepsilon = 2$) environment.

The combination of three basis sets for the three different parts of the fragments was used, namely 6-311+G(d,p) for the freely vibrating bases, 6-31G(d) for the other vibrationally frozen bases and 3- 21g for the furanose rings. All the geometries were kept fixed to the experimental structure (taken from Ref. [58]), with the exception of the missing hydrogens in the experimental X-ray structure, that were optimised at the 6-311+G(d,p) level.

2.2.4 Results and Discussion

2.2.4.1 Normal modes and frequencies of references bases in solution

Before discussing the couplings in the DNA oligomers, in this Section we will focus on the vibrational properties of the single bases composing the systems, i.e. guanine (G) and cytosine (C), in their methylated form. The role of such results is twofold: in fact, besides being interesting *per se*, they can also give an idea of the accuracy of the results obtained in the following analysis on the DNA oligomers, since the single

C and G are used as basis set for the PHVA and HMR analysis. The vibrational properties of C and G have been previously studied in the literature, both from the experimental [53, 70–75] and computational [53, 70, 76–79] points of view. In particular, values for the two selected modes, referred to in the following as G_s and C_s have been reported in various environments. According to DFT calculations, these modes have predominately carbonyl stretch character, as shown in Figure 2.7. Such modes are the ones on which the following discussion on vibrational couplings will be focused.

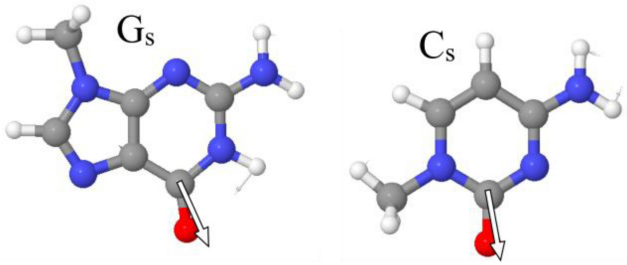

Figure 2.7: Structure and pictorial view of the two selected normal modes of G (left) and C (right)

In Table 2.6, PCM calculated frequencies for G_s and C_s modes in different environments, are reported, chosen according to the availability of experimental data. The outcomes of previous calculations reported in the literature are also shown for comparison's sake, as well as experimental values. In the case of PCM calculated data, two different choices of the definition of the PCM molecular cavity surrounding the solute in the dielectric are compared, i.e. the cavity obtained by exploiting the default settings of Gaussian 03 [80] (G03,) and Gaussian 09 [66] (G09). In fact, the cavity size and shape are the only adjustable parameters in a PCM calculation, for a given solvent. The calculated value of G_s in DMSO are sensitive to the choice of the PCM cavity. In particular, the use of a smaller cavity (the G03 default settings) decreases the calculated value of more than 20 cm^{-1}. As said, the G_s mode involves the C=O group, which, due to the geometry of the molecule is exposed to the solvent, and therefore very sensitive to the polarity of the solvent (compare also

the previous calculations in vacuo reported in Table 2.6). However, with the default G09 settings, the cavity surrounding the C=O group is larger than in the case of the G03 default settings, so that a decrease in the solvent effect (which causes a decrease in the calculated value) is observed. As far as the comparison with the experiment is concerned, a better agreement is obtained with the use of the G03 cavity. However, both choices of the PCM cavity yield a experimental/calculated ratio in the range 0.96-0.97, which are in line with the reported scaling factors for the same DFT functional and similar basis sets [81]. The use of a low-polarity environment for the calculations (ε=2) makes the calculated values approach the calculations for the isolated system, as it is expected. Also, a very low difference is observed with the two cavities, as the solvent effect being in both cases very low. Also in the case of cytosine in water, the same trend as reported for DMSO as varying the cavity is observed. In fact, a difference of about 20 cm^{-1} is reported for C_s, with the G03 once again approaching the experimental value, with an experimental/calculated ratio in the range 0.97-0.99, depending on the reference experimental value.

2.2.4.2 Normal modes and frequencies in DNA

The analysis reported in the previous Section for the solvated G and C bases has shown the characteristics (including possible limits) of the QM model here adopted to describe vibrational motions in solvated systems. When moving to a more complex environment such as DNA however, further difficulties appear due to the extremely inhomogeneous and anisotropic interactions between the bases and the embedding matrix. In particular, when focusing on vibrations, differences between solvated and embedded bases can appear not only in the frequencies of the investigated modes but also in the nature of the modes themselves. It is thus necessary to analyze the possible changes on the previously investigated modes before trying to simulate their couplings.

As explained in the methodological Section, the computational strategy here adopted is based on the HMR approach, in which the couplings between vibrational modes are obtained by "projecting" the local modes of the uncoupled systems into those of the coupled pair. In present context, the local modes are those of the

uncoupled G or C but in the presence of the embedding matrix, which will modify the local modes due to different effects, including the fact that now G and C are chemically bonded to furanose groups. The presence of a real chemical bond between the guanine or the cytosine to the DNA strand will in fact reduce the vibrational freedom of these molecules with important consequences in the displacements and the frequencies related to the modes. Here, in particular, we shall focus on the coupling between what we previously indicated as G_s and C_s modes.

Mode	This work	Previous calculations in vacuo	Experimental
C_S	1738 G09 $\varepsilon = 2$	1750 (B3LYP/6-31G(d)) [54]	1712 in N_2 [70]
	1738 G03 $\varepsilon = 2$	1660 (BP86/6-311G) [70]	1720 in Ar [77]
			1730 in Ne [78]
	1702 G09 in H_2O	1722 (MP2:6-31G (d, p)) [73]	1645 in D_2O [53]
	1680 G03 in H_2O	1785 (B3LYP/6-31++G(d,p)) [53]	1660 in H_2O [79]
		1818 B3LYP/6-31G(d,p) [74]	
G_S	1799 G03 $\varepsilon = 2$	1686 (BP86/6-311G) [70]	1736, 1749 in Ar [76]
	1799 G09 $\varepsilon = 2$	1727 (B3LYP/6-31+G(d,p)) [71]	1742 in N_2 [76]
	1760 G09 in DMSO	1762 (B3LYP/6-31G(d)) [54]	1693 in DMSO [53]
	1637 G03 in DMSO	1840 (B3LYP/6-31++G(d,p)) [53]	
		1833 (B3LYP/6-31G(d)) [72]	

Table 2.6: Calculated M06-2X/6-311+G(d,p) and experimental values for a selected mode of C and G monomers in various environments. (All data are given in cm^{-1}).

In Figure 2.7, we previously reported the selected modes of G and C whereas in Table 2.7 we report the corresponding frequencies obtained in vacuo and with the different models for mimicking the DNA environment.

With respect to the calculations in vacuo, the presence of the continuum dielectric, even if with a low dielectric constant, causes a decrease in the frequency absolute values, which is of the order of 6 cm^{-1} for C and 10 cm^{-1} for G. The use of a larger PCM cavity (i.e. LCav), causes the results to go towards the in vacuo limit, as expected. Overall, the differences among the results obtained with the two choices for the size of the PCM cavity are minor, in both cases of the order of 5-7 cm^{-1}, and independent on the choice of the fragment. The increase in the dielectric constant of the medium (moving from ε=2 to ε=6) also causes a shift of the

same order. Noticeably, the calculations performed with the "cluster" model yield results very similar to the PCM ε =2, thus showing that the actual environment experienced by the single base in the DNA environment is nicely reproduced by the PCM.

We first note that, even if in Table 2.7 we reported data for fragment 1, the analysis we can get is general as the differences obtained for the same system in different fragments are always small, of the order of 10 cm^{-1}.

Cytosine	C_{S1}	C_{S2}	avg
vacuum	1709	1700	1704
PCM ε=2, StCav	1703	1694	1698
PCM ε=2, LCav	1707	1699	1703
PCM ε=6, StCav	1696	1687	1691
cluster	1703	1695	1699
Guanine	G_{S1}	G_{S2}	avg
vacuum	1764	1755	1760
PCM ε=2, StCav	1754	1745	1750
PCM ε=2, LCav	1761	1752	1756
PCM ε=6, StCav	1743	1734	1738
cluster	1757	1749	1753

Table 2.7: Vibrational frequencies of uncoupled linked cytosine and guanine moieties as obtained with different solvation models, in the fragment 1. C_{S1}, C_{S2} and G_{S1}, G_{S2} refer to the local vibrations of cytosine and guanine in fragment 1, respectively. All values are given in cm^{-1}.

In order to get more insight into the trends just commented, it is relevant to recall here the actual molecular structures of the systems to which Table 2.7 refers. In particular, it is to note that all the calculations were performed on the same geometries, corresponding to what is extracted from the experimental X-ray structure taken from Ref. [58], except for the positions of the hydrogen atoms, which were optimized. In addition, each basis is, in this case linked, to a partially frozen furanose group (see Figure 2.6), and the corresponding frequencies have been obtained in the presence of the coupled basis, kept frozen. All these aspects make the comparison with what was previously shown in Table 2.6 for the "free" bases, quite difficult. In

fact, in that case, the geometries were relaxed in each of the considered environments. As can be seen, the differences are quite substantial: by referring to the PCM $\varepsilon = 2$ calculation, the calculated data for the "free" bases are about 45 cm^{-1} higher than the corresponding ones for the bonded bases in the frozen fragments.

2.2.4.3 Couplings

In Table 2.8 we report the vibrational couplings (β) obtained for the different pairs (stacked and HB) using different solvation models: the values reported in the different columns refer to G-G, C-C, and G-C, in the stacked pairs (see Figure 2.6 a, b, c) and G-C in the HB pair (see Figure 2.6g), respectively. In the case of stacked G-C two sets of values are reported corresponding to the two different diagonal arrangements (see Figure 2.6c).

environment	β_{GG}	β_{CC}	β_{GC}	β_{CG2}	β_{GC}(HB)
gas phase	10.0	4.5	2.5	4.5	11.4
ε=2, StCav	9.1	3.7	0.9	4.0	11.8
ε=2, LCav	9.1	3.6	1.0	4.3	12.0
ε=6, StCav	8.1	3.5	0.5	2.9	13.7
cluster	8.6	3.6	1.5	4.2	10.8

Table 2.8: Vibrational couplings calculated in vacuo and through different solvation models, in the fragment 1. All values are in cm^{-1}.

As far as the nomenclature in Table 2.8 is concerned, we note that, the coupling terms β_{GG} and β_{CC} refer to stacked guanine and cytosine bases, respectively, and β_{GC}, β_{CG2} refer to the diagonal coupling between guanine and cytosine.

As it can be seen from the data reported in Table 2.8, the inclusion of the effects of the DNA environment always leads to a decrease of the coupling constants, with the only exception of the HB pair in a PCM environment.

Such a decrease in the β values can be ascribed to screening effects of the polarisable environment and this is what found for all stacked pairs with all solvation models. As expected the largest screening is found in the case of PCM with $\varepsilon = 6$ (i.e. the highest dielectric constant). For all stacked pairs the cluster calculation is

better reproduced by the PCM model with $\varepsilon = 2$, which can be defined as the most realistic continuum model for describing a DNA-like environment: therefore, in the following, the analysis of PCM environment will be limited to this description.

In the case of the HB pair, the analysis is less simple as the PCM description always leads to an increase of β also in the case of the smallest permittivity (ε=2), and the largest cavity. This increase seems to be due to a large variation of the transition densities which is here opposite to the expected screening effect which is also diminished being the two coupled bases quite close. [82]

Moving now to the comparison among the different pairs, it is interesting to note that the GG stacked pair presents a coupling constant very similar to that of the GC HB pair, for which the largest interaction was expected.

In order to be properly compared with experiments, the results reported in Table 2.8 have to be further analysed so to estimate the effects of heterogeneity along the double strand. As explained in the methodological Section, from the DNA oligomer we have extracted five non-equivalent fragments (see Figure 2.6). The corresponding β values obtained in vacuo and with PCM $\varepsilon = 2$ with the two cavities are reported in Table 2.9, whereas in Table 2.10 we collect the main geometrical parameters, namely the internuclear distances between the carbonyl carbons of the two coupled bases and the angles between the corresponding CO vectors.

fragment	β_{GG} vac	β_{GG} $\varepsilon=2$ LCav	β_{GG} $\varepsilon=2$ StCav	β_{CC} vac	β_{CC} $\varepsilon=2$ LCav	β_{CC} $\varepsilon=2$ StCav
1	10.0	9.1	9.1	4.5	3.7	3.6
2	11.7	10.7	9.9	3.5	3.4	3.4
3	6.7	6.7	6.5	2.9	2.6	2.5
4	13.9	12.9	12.0	3.4	3.3	3.3
5	10.6	9.8	9.0	2.9	2.7	2.7
avg	10.6	9.8	9.3	3.4	3.1	3.1

fragment	β_{GC} vac	β_{GC} $\varepsilon=2$ LCav	β_{GC} $\varepsilon=2$ StCav	β_{CG2} vac	β_{CG2} $\varepsilon=2$ LCav	β_{CG2} $\varepsilon=2$ StCav	β_{GC}(HB) vac	β_{GC}(HB) $\varepsilon=2$ LCav	β_{GC}(HB) $\varepsilon=2$ StCav
1	2.5	1.0	0.9	4.5	4.3	4.0	11.4	12.0	11.8
2	1.5	1.3	1.1	8.2	7.5	6.9	9.7	9.8	9.7
3	6.0	5.7	6.0	11.9	8.5	6.1			
4	1.5	1.3	1.3	3.4	3.6	5.0			
5	6.3	2.4	1.7	4.6	4.2	4.1			
avg	3.6	2.3	2.2	6.5	5.6	5.2			

Table 2.9: Calculated vibrational coupling constants for the investigated fragments in different environments (All values are given in cm^{-1}).

fragment	r_{GG}	r_{CC}	r_{GC}	r_{CG2}	r_{GC}(HB)	θ_{GG}	θ_{CC}	θ_{GC}	θ_{CG2}	θ_{GC}(HB)
1	4.2	4.4	7.3	4.2	4.5	24	24	174	162	174
2	3.7	4.7	7.2	4.5	4.4	32	40	168	154	170
3	4.6	5.5	4.7	4.2		47	47	91	96	
4	3.6	4.5	7.1	4.7		21	24	175	164	
5	3.8	4.4	7.1	4.5		27	31	178	156	
avg	4.0	4.7	6.7	4.4	4.5	30	33	157	146	172

Table 2.10: Internuclear C(O)-C(O) distances (in Å) and CO-CO dihedral angles (in degrees) in the coupled bases in the different fragments.

We note that the significant differences found in the fragment n=3 are due to the change in the sequence of bases. In fact, we note that, in fragments 1, 2, 4, 5 the coupling terms β_{GG} and β_{CC} refer to stacked guanine and cytosine bases, respectively, and β_{GC}, β_{CG2} refer to the diagonal coupling between guanine and cytosine, whereas in fragment 3, the coupling terms β_{GC}, β_{CG2} refer to the coupling between stacked

guanine and cytosine, respectively, and β_{GG} and β_{CC} refer to the coupling between diagonal guanine and cytosine (see Figure 2.6d-f).

The comparison of the β values with the structural data reported in Table 2.10 reveals that the vibrational couplings are sensitive not only to the inter-layer distances, but also on the specific DNA base pairs, i.e. on the specific environment acting on the specific DNA basis.

Finally, in Table 2.11, a comparison between our data and the outcomes of previous calculations are reported, as well as experimental data available in the literature.

We first note that previous calculations were performed by exploiting a different approach with respect to ours. In fact, the data reported in Ref. [53], were obtained by using a Finite Difference (FD) approach, in which the coupling is calculated through the numerical evaluation of total energy second derivative, with respect to the local modes of the single nucleic acid bases. In this case, the local modes are normal modes of the isolated nucleic basis.

The calculations reported in Ref. [54], were performed with an extension of the HMR approach (Extended-HMR), which assumes the Hessian matrix in the atomic coordinate system to be divided into blocks, each associated to the local nucleic acid bases modes. Such an Hessian sub-matrix generates the correspondent local modes, which are used to transform the Hessian matrix from the global basis modes to the local modes. The same approach was also exploited to obtain the data reported in Ref. [55], where environmental effects are taken into account through molecular dynamics techniques.

The differences between the various approaches explain the variability of the results, being the set of values for the β_{GG} vibrational coupling the most significative under this comparative viewpoint. Also, due to the large differences between the computational approaches previously exploited and our method, it is not simple to clearly evidence the origins of the discrepancies. However, the trend reported for the extended-HMR/B3LYP approach by Lee and Cho [54] is in good agreement with our data, whereas the largest discrepancies are noticed for FD calculations [53], which is however the most different with respect to our model.

Table 2.11 also reports the comparison between the calculated and the fitted experimental vibrational couplings taken from Refs. [75] and [53]. Overall, a general good agreement with experiments is found, especially if we consider that the experimental findings refer to a dG_5C_5 sequence which is not identical to the similar sequence dG_4C_4 used in the present study. The effect of the environment described in a explicit or in a continuum manner is not large, due to the low polarity of the environment to be modelled; however, the account of environmental effects improves the agreement with the experimental data.

method	environment	β_{GG}	β_{CC}	β_{GC}	β_{CG2}	β_{GC}(HB)	Ref.
HRec/M06-2X On fragment 1	gas phase	10.0	4.5	2.5	4.5	11.4	ThisWork
	$\varepsilon = 2$, LCav	9.1	3.7	1.0	4.3	12.0	
	$\varepsilon = 2$, StCav	9.1	3.6	0.9	4.0	11.8	
	cluster	8.6	3.6	1.5	4.2	10.8	
HRec/M06-2X Averaged values On fragment 1-5	$\varepsilon = 2$, LCav	9.8	3.1	2.3	5.6	10.9	ThisWork
	$\varepsilon = 2$, StCav	9.3	3.1	2.2	5.2	10.6	
FD/MP2	gas phase	$\varepsilon = 2$	$\varepsilon = 2$	3.0	4.7	11.6	[53]
FD/B3LYP		LCav	StCav	1.6	5.0	10.4	
Extended-HRec/B3LYP	gas phase	8.4	1.3	0.4	2.5	13.9	[54]
	Cluster	8.3	1.0	0.2	2.3	13.7	
	classical MD simulation in D_2O solvent	17.4	3.2	1.8	4.3	12.8	[55]
exp. (±2cm-1)		9.5	0.7	1.9	2.7	9.6	[53]
exp.		9.7	2.3	> 1.0	5.0	–	[75]

Table 2.11: Comparison among experimental and calculated vibrational couplings. All values are given in cm^{-1}.

Chapter 3

Electronic absorption and fluorescence spectroscopy

This Chapter deals with the modelling of environment effects on electronic absorption and fluorescence spectroscopy, of molecular probes in apolar, polar and protic solvents (Section 3.1), in membrane (Section 3.2) and intercalated in nucleic acids (Section 3.3).

3.1 Molecular probes in apolar, polar and protic solvents

This Section deals with the modelling of environment effects on electronic absorption and fluorescence spectroscopy of solvated molecular probes.

Although the environment effects in solvated systems are commonly described as simple univocal indices, they actually reflect extremely complex phenomena involving many different intermolecular interactions and are affected by coupled dynamical processes of both the molecular probe and the solvent [83,84]. This is more evident in emission spectra in which the solvent effects and dynamic, cannot be separated from the dynamics of the excited molecular probes; in particular, in this process the excited probe may remain immobilized at a certain location or due to molecular diffusion it may undergo excursion over a distance within its excited state lifetime,

showing the average properties of the diffusive region. For these reasons, these complex environment effects (especially on emission spectra) cannot be described using simple polarity scales [84].

Our aim is to model the absorption and fluorescence properties of solvated fluorescent probes using a TD-DFT approach, combined with three alternative families of methods: (i) PCM (see Subsection 1.1.1), (ii) QM/MM-Pol (see Subsection 1.1.2) and (iii) a "super-molecular" approach, where both the solute and some neighbouring solvent molecules are explicitly included in the QM calculations.

These methods have been applied to the study of a set of fluorescent probes, namely, 4-aminophthalimide (4-AP), 6-Propionyl-2-dimethylaminonaphthalene (PRODAN) and a recently synthesized PRODAN analogue 7-diethylamino-9,9-dimethyl-9H-fluorene-2-carbaldehyde (FR0). Their structures are shown in Figure 3.1.

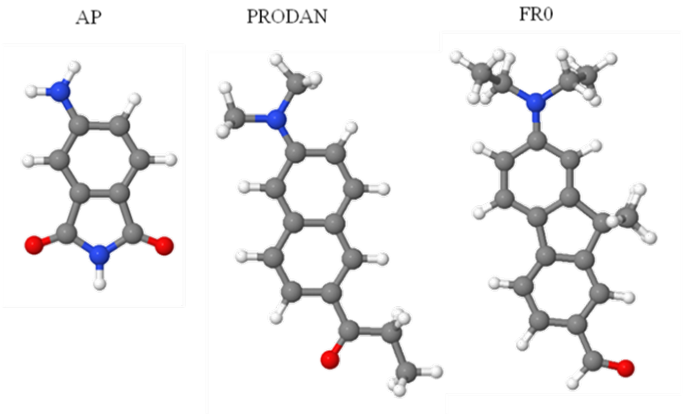

Figure 3.1: Graphical representation of the three investigated fluorescent probes

The sensitivity of these molecular probes to even small changes in the local environment polarity is mainly due to their charge-transfer (CT) character [85,86]; i.e. electronic transitions can be rationalized in terms of an intermolecular charge transfer from a donor part to an acceptor part of the same molecule, with a large change in the dipole moment between the two states. If the fluorescent probe also presents HB sites, it shows a greater sensitivity, in the spectroscopic molecular response, to the properties and dynamics of the HB solvent [87, 88], in addition to polarity. Moreover, femtosecond-resolved fluorescence Stokes shifts have shown that the charge transfer in a HB environment is assisted by collective solvent interactions

and delocalization of charges through the solvent network [89]; the possibility for a CT excited state to activate HB networks can give rise to new deactivation channels, mostly of nonradiative nature, which can largely reduce the fluorescence quantum yield and eventually lead to its complete quenching.

3.1.1 Computational Details

All the QM calculations have been performed by using a locally modified version of the Gaussian 09 package. [66] The ground- (GS) and first singlet excited-state (ES) geometry optimizations and absorption and emission calculations were performed by means of the (TD)DFT method using the CAM-B3LYP functional [90,91] and the 6-311+G(d,p) basis set. The IEF-PCM (see Subsection 1.1.1) has been used to describe the effects of the environment with cavities built as a series of interlocking spheres centered on atoms with the radii: [45] 1.7 Å for C, 1.9 Å for CH, 2.0 Å for CH_n (n=2, 3), 1.52 Å for O, 1.6 Å for N, and 1.2 Å for H not bonded to C, all multiplied by a cavity size factor of 1.2. PCM vertical absorption and emission energies were obtained, by exploiting the corrected linear response (cLR) scheme (see Section 1.2). To analyze the effects of HB, molecular dynamics (MD) simulations were carried out with two protic solvents (water and methanol). Solute geometries are the same optimized structures previously used for the absorption and emission calculations. During all the simulations, the solute geometry was kept fixed. Every solute was inserted in parallelepiped boxes and solvated with nonpolarizable TIP3P water molecules [92] and nonpolarizable f99 methanol molecules. [93] All the simulations were performed using the AMBER9 package where the solute was described with the general amber force field (GAFF). [94] In order to extend the simulations to excited states and to have a consistent picture for both GS and ES simulations, the electrostatic charges have been calculated with the Merz-Singh-Kollman scheme [95,96] applied to GS and ES geometry and electronic density, respectively, using the same level used for the QM calculations. Before each production simulation was started, the cell size for both adducts was adjusted in a series of minimizations and short NVT molecular dynamics simulation runs in order to achieve both the correct temperature of the MD bath and the correct density of the solvent molecules filling the

simulation box. The final box dimensions and the corresponding number of solvent molecules are collected in Table 3.1.

System	Solvent	State	Box volume	Number of molecules
4-AP	Water	S_0	31.3 x 28.6 x 25.0	760
		S_1	30.0 x 29.3 x 25.0	749
PRODAN	MeOH	S_1	35.4 x 34.7 x 30.1	566
	Water	S_1	35.9 x 29.0 x 26.1	916
	MeOH	S_1	39.4 x 34.0 x 29.4	599
FR0	MeOH	S_1	41.3 x 36.1 x 41.7	948

Table 3.1: Box dimensions in Å, and number of solvent molecules for AP (water and methanol), PRODAN (water and methanol), FR0 (methanol), all for the excited state.

The Andersen temperature coupling scheme [97] with a relaxation time of 0.4 ps was employed. The time step was set to 1 fs. Periodic boundary conditions were applied, and the particle mesh Ewald method [98] was used to deal with electrostatic forces. Starting from the last obtained equilibrium configuration, production runs were performed in the NVT ensemble for a total simulation time of 2 ns. Mean residence times have been calculated according to the Garcia and Stiller algorithm. [99] The exponential survival function was obtained as the average of 20000 configurations, that is, every 0.1 ps. Configurations were saved every picosecond for subsequent QM and QM/MM-Pol calculations (see Section 1.1.2). New sets of partial atomic charges and distributed polarizabilities were derived and used in the QM/MM-Pol calculations (see Table 3.2 and 3.3). In particular, the distributed atomic dipole-dipole polarizabilities were calculated using the LoProp [100] approach as implemented in the Molcas [101] program, whereas the atomic charges were fitted to the electrostatic potential following the ESP method implemented in the GAUSSIAN package. For a more detailed discussion, see ref [95]. The calculations were performed at B3LYP/aug-cc-pVTZ level. The ground- and excited-state geometry optimizations of aromatic dimers were calculated with the (TD)DFT method using the M06-2X functional [67] with the 6-311+G(d,p) basis set. In all cases absorption and emission energies were computed with CAM-B3LYP.

	q	α
O	-0.64	5.74
H	0.32	2.31

Table 3.2: Charges (in a.u.) and polarizabilities (in a.u.^{3}) for water calculated at B3LYP/aug-ccpVTZ level.

	q	α
C (CH_3)	0.24	6.88
H (CH_3)	-0.03	1.98
H (CH_3)	0.04	2.12
H (CH_3)	-0.03	1.98
O (OH)	-0.60	5.80
H (OH)	0.37	1.80

Table 3.3: Charges (in a.u.) and polarizabilities (in a.u.^{3}) for methanol calculated at B3LYP/aug-cc-pVTZ level.

3.1.2 Molecular fluorescent probes

Molecular probes are particular molecules specifically chosen so that their response to even minimal changes in the local environment is large. Such sensitivity is mainly due to their intramolecular charge-transfer (CT) character, i.e. they are systems where the electronic transitions can be described in terms of an intramolecular charge transfer from a donor part to an acceptor part of the molecule, with a large change in dipole moment between the two states.

This structural modification gives an important charge transfer character to the systems, which generally also show the ability to respond to small perturbations produced by intermolecular interactions giving changes of fluorescence properties and to produce an easily detectable high-intensity signal, which is determined by relatively high molar extinction coefficient and fluorescence quantum yield. In particular, in the ACDAN molecular probe and its analogues, the presence of an electron-donor dimethylamino group and an electron-accepting carbonyl group, on opposite sides of the naphthalene core, is responsible for the CT character of these fluorophores. [85] In isotropic solvents they exhibit a fluorescence emission which changes with the polarity of the environment: it shifts from about 430 nm to about 530 nm in going from cyclohexane to water. [88,102,103] Moreover, the presence of HB sites in a fluo-

rescent probe introduces additional changes in the spectroscopic molecular response in protic solvents and a greater sensitivity to the HB properties and dynamics of the solvent, [87, 88, 104] in addition to polarity.

When used to probe membrane environments, they are also greatly affected by phase changes; remarkable variations in the fluorescence spectrum have been observed experimentally, in particular when going from liquid crystalline phase to gel phase. Changes of membrane composition are also relevant.

The molecular fluorescent probes investigated in this research work are part of this family. In the following Subsection we summarized the experimental properties of the molecular fluorescent probes investigated in this thesis.

3.1.2.1 PRODAN

PRODAN was first molecule synthesized, in 1979 by Weber and Farris [102], as a probe of solvent polarity: to this scope they sought to impose polarity dependence on the emission of the molecule by maximizing the distance between the electron donor (dimethylamino) and electron acceptor (carbonyl) groups on the naphthalene scaffold. The effect of polar solvents on its absorption and, more effectively, on its fluorescence spectra is large, leading to significant shifts of the main bands. This property has lead many investigators to use PRODAN as a probe of local solvent polarity in micro-heterogeneous macromolecular systems. In particular, the probe has been largely employed to investigate the nature and transitions of natural, synthetic, and bio-mimetic lipid membranes. [105–113] The excited-state kinetics of PRODAN are complex, and the origins of its solvatochromic nature are still on debate in the literature. In particular, a long-term controversy is whether PRODAN fluorescence occurs from a planar or from a twisted state. [114–116]

3.1.2.2 4-AP

The so called AP-based probes represent a large class of derivatives of the aminophthalimide (AP), differently substituted in the aromatic core and/or in the amino groups by short/long aliphatic moieties, with or without terminal polar functional groups (e.g.: COOR, NR_2, etc.) at the end of the tails. In particular, 4-AP and

4-DAP (the analogous of 4-AP with a dimethyl-ammine substituent) molecules are attractive candidates for probing the local properties of both homogeneous and heterogeneous media. [117, 118] The large versatility of 4-AP system is due to the fact that it emits from an intramolecular CT state. [119] Its fluorescent maximum is sensitive to both solvent polarity and to specific interactions of HB solvents such as alcohols and water. [120] Moreover, 4-AP is highly fluorescent in non polar and polar media and poorly fluorescent in protic media. The quantum yield remains more or less constant in non polar and polar solvents (70% in dioxane) [120] but a drastic fall is observed in protic solvents (1% in water). The lifetime of the emitting state is quite long-lived in aprotic solvents (14-15 ns), [120] whereas it is significantly shortened in protic media (1 ns in water). [121] Thanks to the above mentioned fluorescent response properties, AP-based systems were employed as probe molecules for investigating various types of environments: (i) homogeneous;, (ii) micro heterogeneous composed by cyclodestrines, [120] micelles [121,122] and polymer matrices [123] and (iii) binary solvent mixtures. [124–126]

3.1.2.3 FR0

This molecular probe has been recently synthesized as a fluorene derivative of PRODAN. [127] Its spectroscopic studies show that compared to PRODAN, FR0 exhibits a 2-fold larger solvatochromism and absorption coefficient, a manifold larger two-photon absorption cross section, red-shifted absorption and emission, and higher photo-stability. FR dyes exhibit fluorescence quantum yields (QY) in the range of 70-90% in a large dielectric range, which are comparable to those of PRODAN and are structurally similar to the 2-amino-7-nitro-fluorenes, [128] which also show high sensibility to solvent effects (both bulk and specific).

3.1.3 Results and Discussion

To proceed in the following investigation of the molecular properties of the investigated probes, a preliminary conformational analysis is necessary. For symmetry reasons 4-AP possess only a conformation, whereas PRODAN and FR0 (shown in their cf.1 state in Figure 3.1) have another accessible conformational state (cf.2,

with the C=O group flipped 180° with respect to the aromatic plane) in both their ground and excited states. Our calculations show that PRODAN and FR0 cf.1 are slightly more stable than the corresponding cf.2 (about 0.4 kcal/mol in water for PRODAN and about 0.2 in methanol for FR0) at the GS. In the following analysis the focus will therefore be focused on cf.1, but checks on possible specificities due to the presence of the other conformer were taken into account.

3.1.3.1 Nature of Ground and Excited States

The pronounced solvatochromism of molecules characterized by donor and acceptor groups connected through conjugated π-bonds is mainly due to a net change in the charge distribution (see Figure 3.2) moving from the electronically ground to the excited state. [85, 86]

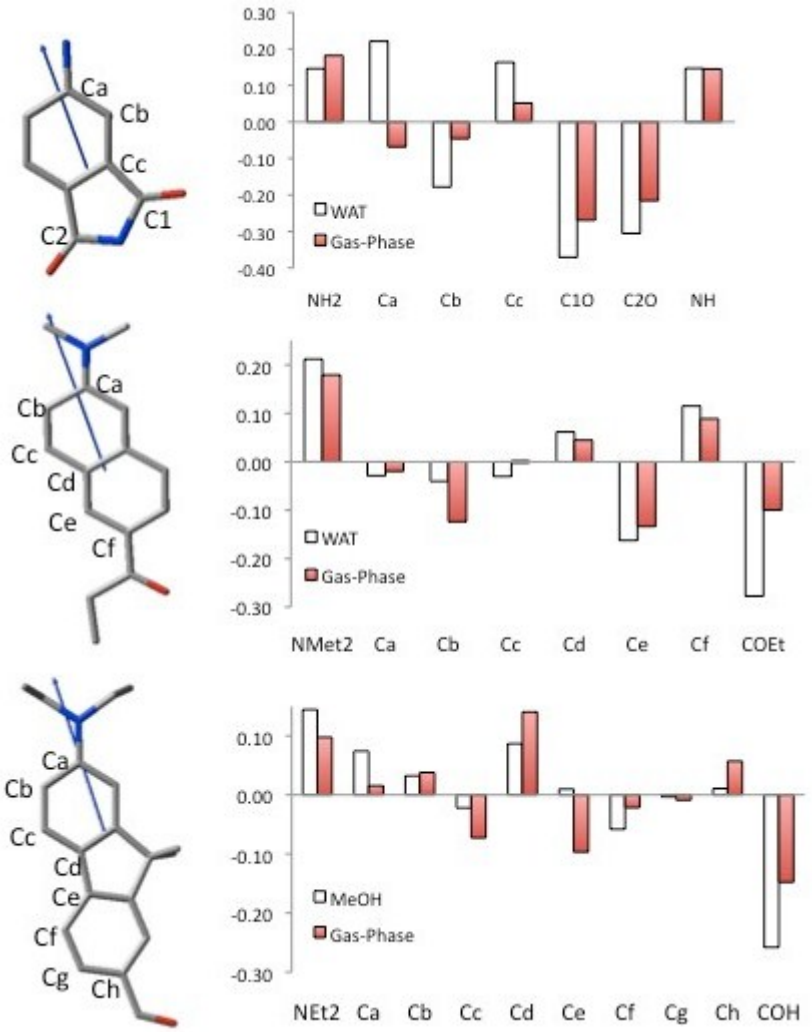

Figure 3.2: Calculated excited state dipole moment orientations and ESP charge changes (Δq) on selected atoms (or group of atoms) going from ground to excited state for 4-AP (up), PRODAN (middle) and FR0 (below). The labelling of atoms is reported in the molecular structures shown on the left.

Such a charge transfer is quantified in terms of a large change in dipole moment in the excited states. Table 3.4 collects experimentally determined ground-state dipole moments and the ground-to-excited changes, [102, 103, 116, 127, 129–137] together with the results calculated in the present work. Calculated (TD)DFT values for 4-AP are in good agreement with experiments [132–134] when gas-phase data are considered; this is what one should expect as the experimental data are generally extrapolated at zero polarity. As far as PRODAN is concerned, a more delicate analysis is required as a long-term controversy is whether PRODAN fluorescence occurs from a planar or from a twisted state. [129–131] Abelt and co-workers [115,116]

investigated the photophysical properties of several PRODAN derivatives, where the dialkylamino group is constrained to be planar or perpendicular with the naphthalene ring, by means of experimental solvatochromism studies. They found that constrained planar analogues behave just like PRODAN, while twisted analogues behave very differently, and, in addition, they have a pyramidal amino group rather than one that is planar. All this considered, they concluded that PRODAN emission is from a planar intramolecular charge-transfer state. This conclusion is further confirmed here on the basis of values reported in Table 3.4 for the variation of the dipole moment.

		calcd		exptl
		gas phase	polar solvent	
4-AP	μ_{GS}	5.3	7.0	3-4 [132–134]
	$\Delta\mu$	4.5	8.0	3-5 [132–134]
PRODAN	μ_{GS}	6.0	4.6	3 [137];5 [103, 135, 136]
	$\Delta\mu$	8.5	9.2	5 [135];7 [103];8 [137];13 [136];20 [102]
FR0	μ_{GS}	6.8	9.1	-
	$\Delta\mu$	7.3	13.5	14 [127]

Table 3.4: Experimental and calculated ground-state dipole moments (μ_{GS}) and transition dipole moments ($\Delta\mu$), in gas phase and in a polar solvent using PCM. The calculated value are determined using several methods. All values are in Debye.

Contrary to what originally reported by Weber and Farris [102] who found a large (20 D) variation of the dipole moment upon excitation, the successive experimental analyses have shown that the variation of the dipole of PRODAN is in line with other CT systems, being in the range 4-9 D. Indeed a trivial error in the equation used by Weber and Farris was recognized by Balter et al., [137] who corrected the dipole variation to only 8 D from an analysis of solvatochromic data in some selected solvents. The calculated (TD)DFT values (4.6-9.3 D) are in agreement with these most recent experimental data, and they show that a planar ES state structure indeed provides a reliable description of the excited-state dipole moment of PRODAN in both apolar and polar environments. As far as the recently synthesized FR0 system is concerned, the value of the ground-to-excited-state change of dipole moment, $\Delta\mu_{(ES\text{-}GS)}$, determined by et al. [127] is in very good agreement with that calculated at the (TD)DFT level in polar solvent. In conclusion, the selected QM

level of calculation [(TD)-CAM-B3LYP] seems to correctly reproduce the electronic and geometrical changes following the excitation for all the three molecules. This makes us confident that a similar reliability of such a method also applies to the analysis of solvent-induced changes.

3.1.3.2 Structural changes

In the three graphs we report the changes in the distance (d) during the excitation, for selected bond lengths of the molecular probes investigated. Generally, from the structural point of view, the charge transfer (CT) process leads to the following consequences:

1. the "hot-spots" (most sensitive part) of the molecule, involving the donor (D) and the acceptor (A) groups, exhibit the typical changes for the CT process: the d(C=O) increases during the CT process, while both the d(N-C) and d(C-CO) decrease.

2. when moving from 4-AP to FR0 the distance between D and A increases and, consequently, the involvement of the aromatic carbons considerably increases, clearly indicating that the charge flux is not completely localized on the two extremes but it also involves the whole conjugation path.

3. as commonly found, the d differences obtained in the gas-phase are smaller that those found in the polar environment, especially for what concerns the most polar part of the structures.

In the three graphs of Figure 3.2 we report the differences in the electrostatic potential derived (ESP) charges between excited and ground state, in gas-phase and in polar solvents (ACN for 4-AP and DMSO for PRODAN and FR0). Positive and negative values represent the decrease and increase of the electronic charge density at the atoms (or group of atoms) during the electronic excitation, respectively.

As expected, the largest differences in the ESP charge changes (Δq) were found for both donor (NH_2, NMe_2 and NEt_2) and acceptor (C=O) groups, with Δq in polar solvent (gas-phase) being in the range 0.14÷0.21 a.u. (0.09÷0.18 a.u.) and

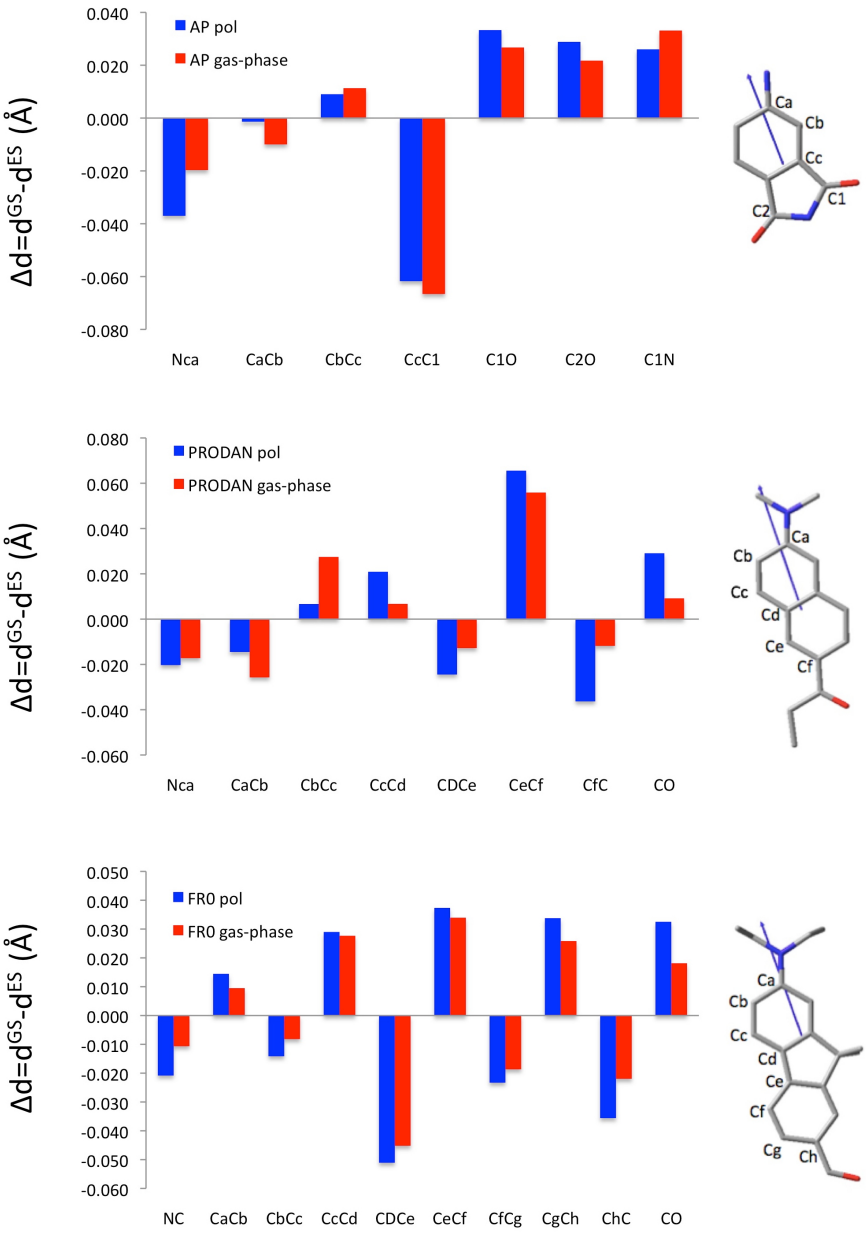

Figure 3.3: Distance changes (d) on selected bonds going from ground to excited state for 4-AP (up), PRODAN (middle) and FR0 (below). The geometries were calculated at the CAM-B3LYP/6-311+g(d,p) level in both the gas-phase and the polar solvent: water for 4-AP and PRODAN, while MeOH for FR0. The labelling of atoms is reported in the molecular structures shown on the right.

-0.26÷-0.34 a.u. (-0.10÷-0.25 a.u.), respectively. However, the graphs show that also carbons of the aromatic core considerably change their charges upon excitation: this is a clear indication that the charge flux is not completely localized on the two extremes but it also involves the whole conjugation path. The results obtained by the analysis of ESP charges confirm the charge transfer nature of the excitation for all the probes: this character is also corroborated by the consequent modification of the probes' structures (e.g bond lengths, see Figure 3.3). All this puts in evidence the most solvent-sensitive parts (which could be defined as the "hot-spots" for the CT process, and consequently for the solvent effect on the associated electronic transitions) of the fluorescent probes. In particular, this electronic/structural information will turn out to be extremely important for the understanding of the role of specific interactions (such as hydrogen bonding, aggregation, etc.), as discussed in details below.

3.1.3.3 Analysis of the Experimental Data

Before moving to the results, it is necessary to make a preliminary analysis on the use of available experimental data. As gas-phase data are usually difficult to be experimentally determined, it is necessary to introduce as reference the most "inert" apolar solvent among those measured. Here the term inert means that the selected solvent, besides being apolar, should not present any specific interaction with the solute and should also allow a good solubility. For PRODAN and FR0, the most standard apolar solvent, namely hexane, seems not a good choice. Both molecular probes show in fact a very low quantum yield in hexane and an unexpected blue shift with respect to other apolar solvents (with respect to dioxane and toluene 0.2-0.4 eV blue shifts are observed in the fluorescence). These shifts indicate possible aggregation effects due to the high polar character of the probes and their low solubility in hydrocarbon solvents. [138] If now we assume that this effect is active also in PRODAN when dissolved in hexane, we can relate the blue shift observed in the fluorescence to the formation of dimers in the excited state reasonably stable in the low polar hexane. To test such a hypothesis we have considered a PRODAN dimer assuming a stacked structure with an antiparallel arrangement. The final

optimized structure for the excited state is shown in Figure 3.4. The calculated shift in the dimer fluorescence with respect to the monomer value is 0.16 eV toward the blue, whereas the shift derived from the difference in fluorescence maxima measured in hexane and in dioxane or in toluene is ca. 0.2 eV. As it can be seen from this comparison, the aggregation effects correctly reproduce the experimentally observed blue shift, and they confirm that hexane cannot be considered as an inert solvent. For PRODAN and FR0 probes, we have thus selected dioxane as inert reference solvent.

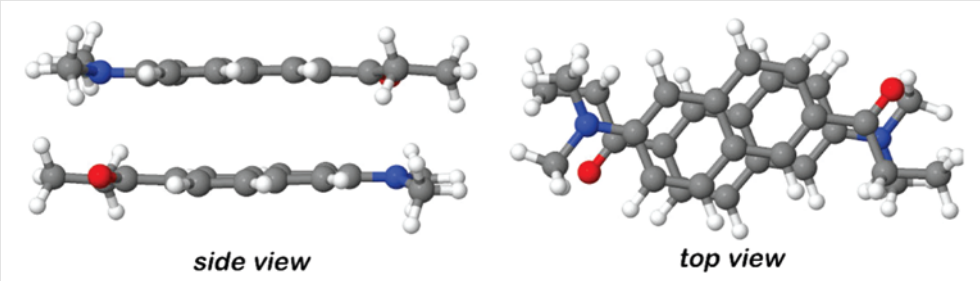

Figure 3.4: Structure of the antiparallel dimer of PRODAN in its side (left) and top (right) views.

3.1.3.4 A Purely Continuum Description

In Table 3.5 we report a comparison between experimental and calculated solvent induced shifts on absorption and emission energies and Stokes shifts (SS) of the three probes. The comparison is split into a δ_{pol} shift obtained moving from apolar (hexane for 4-AP, dioxane for PRODAN and FR0) to polar solvent (acetonitrile for 4-AP and dimethylsulfoxide for PRODAN and FR0) and a further δ_{HB} shift obtained moving from the polar solvent to an HB one (methanol and water for 4-AP and PRODAN and methanol for FR0). All calculated results refer to the PCM method.

For all probes the continuum description gives very accurate estimates of the polarity-induced δ_{pol} shift for both absorption and fluorescence energies and SS. The good general agreement found for δ_{pol} shifts is an important result. It in fact shows that nonelectrostatic effects (mostly due to dispersion and repulsion interactions between solute and solvent) which are not included in the PCM are either not important in these systems or (more probably) quite insensitive to the solvent; thus,

they cancel out when solvent-solvent shifts are considered. On the contrary, large discrepancies are observed on δ_{HB} for all the probes: this is reasonably expected for continuum models, which do not accurately account for strong local effects as those induced by H-bonds. It is, however, important to note that δ_{HB} is quite different for absorption and fluorescence processes; indeed for fluorescence it is large for all probes (0.2-0.4 eV) while for absorption it is really relevant only for 4-AP (0.12-0.13 eV). These findings show an important specificity of 4-AP with respect to the other probes, namely, its capacity to establish strong H-bond already at the electronic ground state. As a result of the unsatisfactory description of H-bonding effects on absorption/emission energies, the PCM-calculated SS are largely underestimated for all probes in all protic solvents. These behaviours will be further discussed in the following Subsection where H-bonding effects will be analyzed combining different computational strategies.

		4-AP			PRODAN			FR0	
		δ_{pol}	δ_{HB}		δ_{pol}	δ_{HB}		δ_{pol}	δ_{HB}
			MeOH	water		MeOH	water		MeOH
Abs	exptl	-0.19	-0.12	-0.13	-0.11	-0.06	-0.01	-0.03	-0.02
	calcd	-0.15	0.00	-0.01	-0.05	0.00	-0.01	-0.07	0.00
Flu	exptl	-0.52	-0.31	-0.40	-0.25	-0.22	-0.30	-0.38	-0.20
	calcd	-0.41	-0.00	-0.03	-0.22	0.00	-0.02	-0.35	0.00
SS	exptl	2725	1534	2192	1161	1257	2310	2804	1485
	calcd	2115	26	183	1339	15	115	2308	20

Table 3.5: Comparison between Experimental and PCM Solvent-Induced Shifts on Absorption (Abs) & Emission (Flu) Energies (in eV) and Stokes Shift (SS, in cm^{-1}) of the investigated probes. $\boldsymbol{\delta_{pol}}$ indicates the shift moving from hexane to acetonitrile for 4-AP and from dioxane to dimethylsulfoxide for PRODAN and FR0. Experimental data are taken from ref. [124] for 4-AP and ref [127] for PRODAN and FR0.

3.1.3.5 Hydrogen Bonding and Other Structuring Effects

One of the most important questions to clarify is if the solvent molecules are able to make stable clusters that modify the optical properties of the solute. Such an analysis is made possible by using a classical MD simulation of each molecular system in the corresponding protic solvent (in water and in methanol solution, for both ground and excited states of 4-AP, in water for excited-state PRODAN, and in

methanol for excited-state FR0). In Figure 3.5 the 3D-radial distribution functions are shown for 4-AP in water in its ground (top left) and excited (top right) state and for excited states of PRODAN (bottom left) in water and of FR0 in methanol (bottom right).

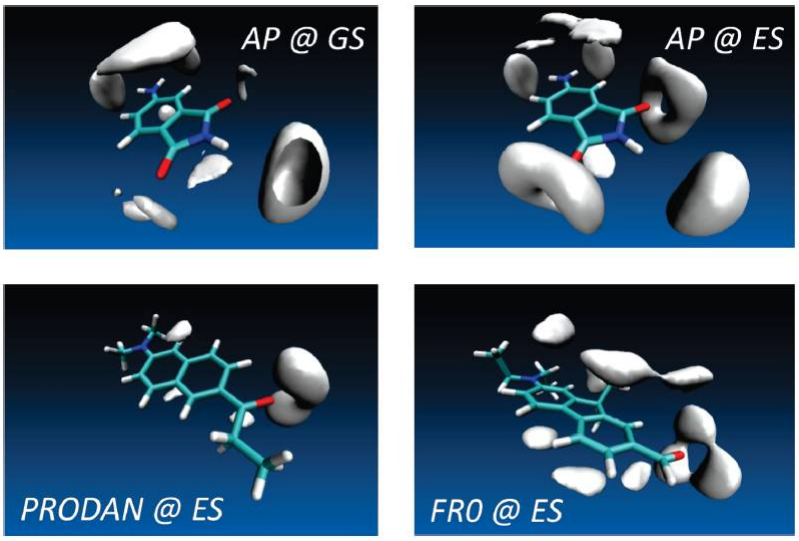

Figure 3.5: 3-D radial distribution functions solute-H(solvent) for 4-AP in water for the ground and excited states (GS and ES, respectively) and for the excited state of PRODAN in water and FR0 in MeOH.

Let us first focus the MD analysis on the 4-AP. As expected by the CT character of the excited state, the coordination number of each carbonyl group increases from 1.1 to 1.5 in water upon excitation. If we now consider the complete HB sensitive part of the molecule, the number of solvent molecules increases from 5 to 7 upon excitation. In parallel, the mean residence time (τ) at the carbonyl groups is increased from 10 to 20 ps. The change in the τ is even more important in the methanol solution, where the molecules remain 92 ps in the first solvation shell for the excited state. It is also worth noting that the O(AP)-H(solvent) distance for the excited state is smaller than the usual H-bonding distance (1.65 Å for both methanol and water solutions). All these data lead us to characterize the H-bond interactions in the excited 4-AP as a situation in between a standard H-bond and a real covalent bond.

Moving to PRODAN and FR0, the HB sensitive sites reduce to the carbonyl groups only. The corresponding coordination numbers are 1.4 (with 24 ps residence

time) and 2.2 (and 103 ps) for PRODAN in water and FR0 in methanol, respectively. The methanol molecules around the solute form a much more rigid structure than the water ones, which, being smaller, have a larger motion freedom than the methanol.

Combining the previous PCM results and this MD analysis, the final picture that comes out for all the probes dissolved in protic solvents is the formation of strongly interacting excited solute-solvent aggregates. These supramolecular systems can be simulated using different strategies. Either one extracts a statistically meaningful sample of solute-solvent configurations from MD trajectories and uses them to simulate the process of interest, or one assumes that the interactions between the solute and the first-shell solvent molecules are so strong and so persistent in time that they really constitute a stable supermolecular system which can be characterized exactly as a real molecular system including its geometry which is obtained through a full QM optimization (see Figure 3.6).

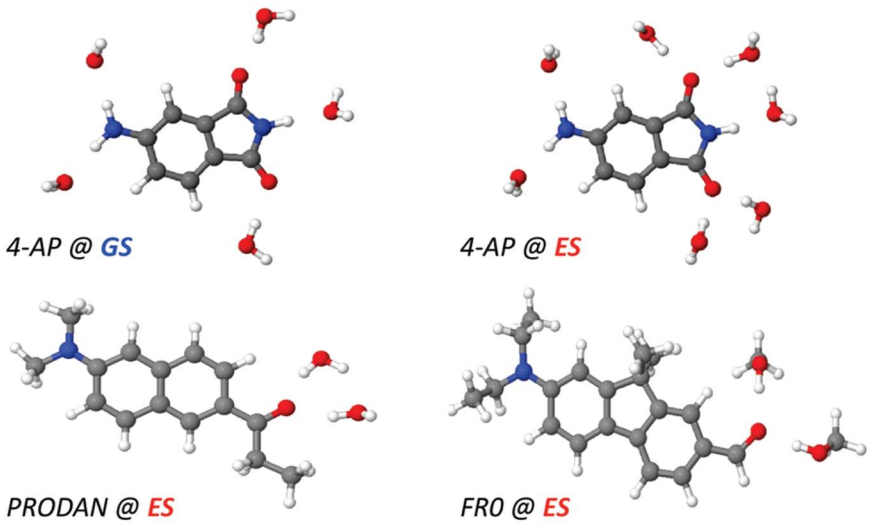

Figure 3.6: Structures of supermolecular systems of 4-AP (both in its ground and excited state) and PRODAN and FR0 (both in their excited states) obtained from QM optimizations of the solute surrounded by explicit HB solvent molecules.

Let us start the analysis of the two strategies with 4-AP. As said before for this probe both the absorption and the emission processes are significantly affected by H-bonds, and therefore MD simulations have been repeated for the two electronic states and the QM supermolecules have been calculated both in the ground and in the excited state. In Figure 3.7a we report the δ_{HB} values for both absorption and

fluorescence in water obtained with the different solvation approaches and, in Figure 3.7b, the corresponding shifts on SS. Here the PCM values refer to those reported in Table 3.5.

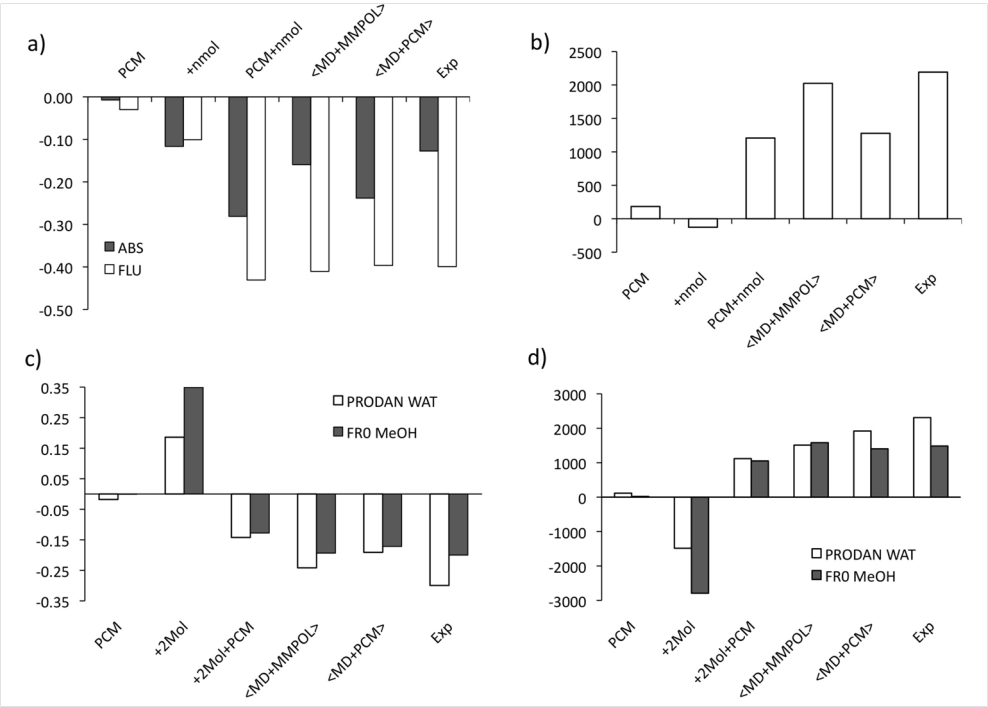

Figure 3.7: Calculated and experimental (a) absorption and emission δ_{HB} and (b) δ_{SS} for 4-AP moving from the polar solvent to water; (c) emission δ_{HB} and (d) δ_{SS} for PRODAN and FR0 moving from the polar solvent to the protic one (water for PRODAN and methanol for FR0). δ_{HB} values are in eV and δ_{SS} in cm^{-1}. The labels "+nmol" and "PCM+nmol" refer to values obtained on the QM supermolecules shown in Figure 4.

We note that two different supermolecule schemes have been tested. One (indicated as +nmol in the graphs) considers only H-bond effects, and therefore the optimization of the cluster as well as the following absorption and fluorescence calculations have been performed in the gas phase while another (PCM+nmol) also includes the effects due to the rest of the solvent beyond the first solvation shell by embedding the cluster in a PCM solvent; in this second scheme both the geometry optimization of the cluster and the absorption and fluorescence processes have been calculated including PCM effects. Also in the case of MD-derived clusters two different schemes have been tested. In the first scheme we have selected 100 configurations and introduced a cutoff of 12 and 14 Å for water and methanol, respectively,

and on the resulting aggregates we have applied a QM description for the probe and a polarizable MM for all the solvent molecules. The resulting average is indicated as $\langle MD + MMpol \rangle$ in the graphs. The second scheme still uses the same MD-derived configurations, but it introduces a shorter cutoff (2.2 Å) and the resulting by far smaller clusters are described using a QM level for both the probe and the solvent molecules whereas the rest of the solvent is substituted by PCM. The resulting average is indicated as $\langle MD + PCM \rangle$. Due to the much larger computational cost of this second approach, the average has been limited to 20 configurations. The first important result which comes out is that both descriptions based on only mean-field effects (PCM) or only H-bonds (+nmol) poorly reproduce the measured shifts. Only in the case of absorption, H-bond effects seem to be dominant and +nmol results are in sufficient agreement with experiments, but this is not true for emission for which pure H-bond effects catch only a minor percentage of the full shift. As a result of this asymmetry in the two processes, the shift on SS is wrong both qualitatively and quantitatively. By adding the effects of the rest of the solvent molecules with a PCM approach, the picture changes drastically: the shift on emission is correctly reproduced whereas some discrepancies remain for the absorption process for which PCM+nmol overestimates the shift, and, as a result, the shift on SS is underestimated. The overestimation in the shift for the absorption process seems to show that a single PCM-QM cluster is not representative of the more dynamic behavior of the solvent molecules around the ground-state solute. This hypothesis is confirmed by the accurate picture obtained with MD-derived solute-solvent configurations treated at the QM/MM-Pol level of description. In this case, both the absorption and the emission processes and the final SS are correctly reproduced. Finally, it is worth remarking that the different behaviours of the various solvation models for absorption and fluorescence energies have to be seen as due to quite different solvation dynamics for the ground and the excited state. While for excited state, all models are equally accurate in reproducing the observed δ_{HB} shift, this is not true for absorption. In other words, this can be expressed saying that the H-bonding effects on the excited state are so strong and so persistent in time that we are exactly in the limiting case where the static picture kept by PCM+nmol and the dynamic

one kept by $\langle MD + MMpol \rangle$ coincide. For the 4-AP in the ground state instead, H-bond effects are weaker and their description requires a real dynamic approach.

The computational analysis can go even further in investigating the role of H-bonding effects. It can, for example, dissect the behavior of the various sensitive sites of 4-AP and verify if they are additive. To reach this goal, we have considered the dimethylamino version of the AP probe (DAP). Due to the methyl substitution, DAP presents a lower capacity to attract water molecules with respect to 4-AP, and, if H-bonding effects are additive, it should have a smaller δ_{HB} for both absorption and emission. Indeed this is not the case as the measured δ_{HB} is around 0.15 eV for absorption and 0.3 eV for emission in both 4-AP and DAP. To have a definitive proof that this experimental observation is an indication of the dominant role played by H-bonds with carbonyl oxygen atoms, we have determined a new QM supermolecule, constituted by excitedstate DAP and five water molecules.

The structure we have considered is parallel to the one used for 4-AP (see Figure 3.6) but without the two further water molecules H-bonded to NH_2 group. In addition, we have included the effect of the rest of the water molecules using PCM. The δ_{HB} calculated for DAP supermolecule moving from acetonitrile to water is in very good agreement with experiments (0.31 eV), and this confirms what suggested by the experimental observation, i.e., the dominant role played by carbonyl oxygens in the interaction with water molecules. Moving to PRODAN and FR0, in Figure 3.7c-d we report exactly the same analysis shown for 4-AP, but this time only emission (c) and SS values (d) are reported as for absorption δ_{HB} is negligible. As can be seen from the graphs, the description based on only H-bond effects (+2 mol) is not only quantitatively insufficient but also qualitatively wrong as it leads to a blue shift instead of a red shift in the emission energies. This results show that the δ_{HB} shift is the result of a balanced combination of specific H-bonds and longer-range effects. This is further confirmed by the good results obtained with any of the three approaches including the effect of the solvent outer shells. More in detail, the PCM-solvated QM clusters (PCM+2 mol) correctly reproduce the observed behaviours, but they slightly underestimate the shift for FR0 and more significantly for PRODAN; as a result, the shifts on SS are too low for both probes. On the contrary, the

two MD-derived approaches (both PCM and MM-Pol) give a very good description for both probes, with PRODAN still presenting a small underestimation. Indeed the real physics beyond the large solvatochromism of PRODAN fluorescence and its specific sensitivity to H-bonding environments is a still open and very challenging problem as we have commented in the previous Subsection where we have summarized the debate on the possibility of twisted emitting species. However, from our study some conclusions can be derived. First of all, a twisted structure seems to be excluded in any solvent (either apolar, polar, or protic): for both apolar (but still inert) and polar solvents a PCM-like picture of a planar emitting system well reproduces the solvatochromism both in the absorption and in the emission process as well as correctly reproducing the high Stokes shifts. Moreover, specific effects due to solvent molecules which present a clear structured distribution around the excited state have shown to be fundamental to describe the additional shift observed in protic solvents. Once that is clarified, however, some further minor but not negligible effects are still missing in order to completely simulate the solvatochromism of PRODAN. Here we try to suggest two possible mechanisms that could be active in the excited state of PRODAN.

The first possible mechanism has been proposed by Rowe et al. [87] for PRODAN based on a multivariate photokinetic analysis, and it suggests that excitation increases the probability of the carbonyl oxygen protonation in protic solvents. To verify if this hypothesis can indeed explain the large δ_{HB}, we have calculated the optimal geometry of possible protonated species, the PRODAN itself and the PRODAN with two H-bonded water molecules. For both structures we have calculated the emission energies: the resulting δ_{HB} shifts are very similar for the two species, and they are both ca. -0.5 eV. This value is clearly a large overestimation of the observed -0.3 eV but still indicates that effects due to strong H-bonds which eventually result in labile protonated species are in qualitative agreement with the experimental findings. Another possible mechanism that we propose here involves a conformational change induced by excitation. In a recent study [139] on a different probe, acetyl anthracene, we have shown the possibility for an isomerization, due to rotation of the carbonyl group, upon excitation. If we now assume that the same mechanism

can be possible for PRODAN especially when dissolved in H-bonding solvents, we can verify if the emission properties of the second possible conformer (cf.2) can explain the missing contribution to the observed δ_{HB}. To do that we have determined the optimal geometry of the excited-state conformer obtained by a 180° rotation of the carbonyl group with respect to the aromatic plane and calculated the resulting emission energy. Such an analysis has been repeated for both the PRODAN and the PRODAN H-bonded to two water molecules; in both cases, bulk effects due to a PCM solvent have been introduced. The resulting structures present a larger stability than the corresponding ones obtained for cf.1 and an additional fluorescence δ_{HB} shift of -0.05 eV. This additional red shift if summed to the δ_{HB} found for the $\langle MD + MMpol \rangle$ model applied to cf.1 leads to a final HB shift of -0.29 eV, in very close agreement with the experimental -0.3 eV shift measured in water. This analysis is certainly incomplete as calculations of transition barriers as well real of the photochemical reaction path should be performed, but it is a promising hypothesis to explain the additional red shift in the PRODAN fluorescence in protic solvents. We finally note that assuming a similar isomerization effect for FR0 in methanol does not lead to any significant change: emission energies for cf.2 in fact differ from those obtained for cf.1 by less than 0.02 eV.

3.1.3.6 Quantum Yield and Quenching Effects

All the systems here studied present high absorption coefficient and high (in the range of 60-90%) fluorescence quantum yield (QY) for most of the solvents. However, all of them show a net decrease of their QY with protic solvents (and more specifically with water): 2% in 4-AP, 12% in PRODAN, and 3% in FR0. Moreover, a strong decrease of QY is also observed for PRODAN and FR0 in hexane (2% in PRODAN and 11% in FR0). The explanations for these behaviours may be different. In the previous Subsections we have already presented and discussed aggregation effects that can be active for PRODAN (and FR0) in very low polar solvents such as hexane. There we have used these aggregation effects to explain the unexpected blue shift of fluorescence found in hexane with respect to other low polar solvents. The same effects can be used here to explain the strong reduction of QY in this solvent: in

fact aggregation induces excitonic splittings that lead to low-lying dark states not present on the monomeric species. Such states can thus represent possible new decay channels as they can lose their excitation energy in a nonradiative way, for example, due to transfers to the environment. More difficult is instead the analysis of the reduction of QY due to protic solvents (and in particular water) which is common to all the three studied probes. Yuan and Brown [140] attributed the observed decrease in the QY of two 4-aminonaphthalimides derivatives in aqueous ethanol (relative to ethanol) to the quenching by the water molecules. According to this model, a cluster of some seven or eight water molecules is required to effect the quenching, possibly corresponding to the excitation of one quantum of a stretching mode in each water molecule. Harju et al. [141] and Mukherjee et al. [124] suggested that the abrupt decrease in the QY of 4-AP in protic solvents was due to the reduction in the ES-GS energy gap in the proton-transferred species. Also Noukakis and Suppan [142] focused their attention on the protonation degree of the carbonyl group(s) in the excited CT state of AP. The analysis reported in the previous Subsection confirms the fundamental role played by strong HB interactions in the excited state of 4-AP which gives rise to stable large clusters. In particular clusters including up to seven H-bonded water molecules are required to get the correct shift in the fluorescence. This picture can also be used here as an indirect confirmation of the experimentally suggested hypothesis that H-bonds effects are the responsible for the reduction of fluorescence in water (and other protic solvents).

Moving to PRODAN, recently Moyano et al. [143, 144] have used spectroscopic techniques and cyclic voltammetry to show that in water, it self-aggregates due to its low solubility. They have also shown that PRODAN molar extinction coefficient for the charge-transfer electronic absorption band diminishes dramatically in water upon increasing the concentration, which suggests that the intramolecular charge-transfer process is inhibited by aggregation. The results we have previously discussed for PRODAN dimer in hexane can be reconsidered here to support such an hypothesis; as said before the aggregation gives rise to low-lying dark excited states which can allow additional nonradiative decay channels not available when PRODAN is not aggregated. This is the quenching mechanism in H-aggregates made of homodimers.

Unfortunately, specific studies on the QY properties of FR0 are not available, but the similarity with PRODAN reported in the reference paper by Kucherak et al. [127] for hexane seems to indicate that what we have found for PRODAN with the dimeric study can be valid also for this analogue probe.

3.2 Molecular probes in membranes

This Section deal with the modelling of environment effects on absorption and fluorescence properties on molecular probes in a membrane environment.

Membranes are inhomogeneous environments, which can be described as diffuse boundaries within which molecular probes are subjected to different interactions than when they are immersed in a bulk phase. Although they have lengths of few nanometers, membranes are of fundamental importance and govern several chemical and biological processes. [145] Despite that, a microscopic explanation of the effects biological membranes have on the photo-physical properties of molecular probes is still lacking. Furthermore, the experimental results currently available are limited, due to difficulties in distinguishing the response the small membrane volume to that of the adjacent bulk phases. [146, 147] Specific spectroscopic techniques, see for instance ref. [148], have been developed to overcome such limitations.

Molecules inside membranes can experience different effects, depending on their nature (different molecules respond differently to the same local environment [149]), their position in the membrane itself and their orientation. The modification of the photo-physical properties of the probe is the result of a combination of these effects, and it may be very complicated to separate them when carrying out an experimental analysis, since simple polarity-scale models are too simplistic for modelling such a complex environment effect. [150, 151]

The aim of this chapter is to model the absorption and fluorescence properties of molecular probes, inside a diffuse membrane/interface, using an integrated computational methodology, complementing the QM/PCM description of electronic transitions with a recent Molecular Field Theory [152] (MFT) for the calculation of the orientational-positional distribution function of the probe in the membrane. [152]

Since both the PCM and the MFT models are based on a continuum approximation, the molecularity of the solvent is not accounted for; however, the advantage of such models is that they provide a clear connection between the properties of the environment and their effect on the molecule at an affordable computational cost. In principle, specific aspects of solute/solvent interactions, if needed, may be introduced in this picture by, for instance, including explicit solvent molecules.

In this work, the molecule used as a probe is the 6-acetyl-2-(dimethylamino)naphthalene (ACDAN), a fluorescent molecule which is also representative of the longer tail homologues PRODAN and 6-dodecanoyl-2-dimethylamine-naphthalene (LAURDAN). These molecules are commonly used membrane fluorescent probes [153–158]. The structures of two conformers for each of them are shown in figure 3.8.

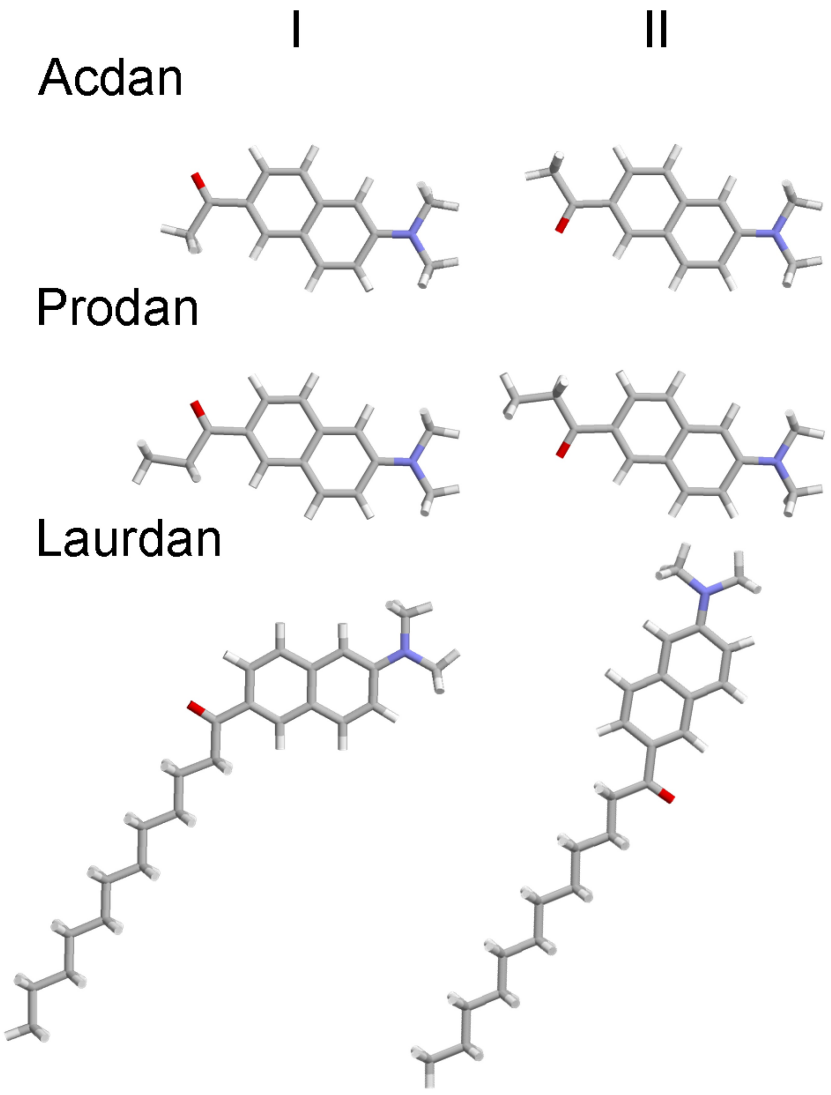

Figure 3.8: Molecular structures of the fluorescent probes ACDAN, PRODAN and LAURDAN. For each probe two conformers are shown, differing for the orientation of carbonyl oxygens, which points either towards the β (I) or the α (II) naphthalene position. Acyl chains in the all-trans chain conformation are shown.

3.2.1 Computational details

Electronic states and vertical transitions of the probes in their ground state S_0 and in the first excited state S_1, in vacuum and in solution, were determined by means of the (TD)DFT method using the CAM-B3LYP functional [90, 91] and employing the 6-311+G(d,p) basis set. The CAM-B3LYP functional was chosen for its ability in treating long-range exchange interactions and therefore in describing states with

charge-transfer character. The IEF-PCM (see Subsection 1.1.1) has been used to describe the effects of the environment with cavities built as a series of interlocking spheres centered on atoms with the radii: [45] 1.7 Å for C, 1.9 Å for CH, 2.0 Å for CH_n (n=2, 3), 1.52 Å for O, 1.6 Å for N, and 1.2 Å for H not bonded to C, all multiplied by a cavity size factor of 1.2. The theoretical apparatus needed to compute environment effects in interfaces and membranes, within IEF-PCM has been discussed in detail in Subsection 1.1.1. The vertical absorption and emission energies in solution were obtained, by exploiting the corrected linear response scheme (see Section 1.2).

ACDAN, which is a commonly used fluorescent probes and is also representative of Prodan and Laurdan, was chosen because of its negligible dependence on the length of the acyl chain and for obvious computational reasons. The results we shall present refer to the probe in conformation I but we checked, on selected points, that results for the other conformation were not significantly different. The ground and excited states geometries of the investigated probe were optimized in bulk water and were kept fixed for all the subsequent calculations.

Here we have used an integrated computational methodology, complementing the QM/PCM description of electronic transitions with a recent Molecular Field Theory (MFT), [152] (see appendix B), for the calculation of the orientational-positional distribution function of the probe in the lipid bilayer. The distribution functions of the probes, reported in the discussion Subsection, was calculated by Pariso in Ref. [159]. The membrane used in the study was the dipalmitoylphosphatidylcholine (DPPC) bilayer. At both QM/PCM and MST levels a consistent model of the bilayer is used, treated as a non-uniform and anisotropic continuum.

3.2.2 Molecular probes in membranes

Since molecular probes bear chromophores which exhibit large changes of their photophysical characteristics as a function of the local environment, they are extremely useful to investigate membrane microenvironments. ACDAN, PRODAN and LAURDAN are important examples in this field. [153–158]

The fluorescence spectra of ACDAN in lipid bilayers exhibit two bands, cen-

tered at 440 nm and 490 nm, respectively. [105, 153, 160] In some cases, additional emission at about 520 nm was found, which was ascribed to dye partitioning in water. [161] Remarkable variations were observed on going from the liquid crystalline to the gel phase, as well as under changes of membrane composition; therefore these probes were devised as suitable to monitor phase transitions and to assess the lateral heterogeneity of lipid bilayers. [158] Moreover, they were proposed as reporters of changes in membrane organization induced by pressure, [153, 162] curvature [163] and strains, [164] as well as by addition of cholesterol, [105,108,109] local anesthetics and alcohols. [109,153,161,165] Different explanations were proposed for the spectral features of the fluorescence emission and, in general, for the results of fluorescence experiments in membranes; after many studies, there remain controversial issues. The red-shift is generally believed to reflect changes in the polarity of the microenvironment related to the amount of water accessible to the probe; [105] a crucial role of the mobility of water and/or lipids was stressed. [106, 153, 165–167] It was discussed whether the change of polarity should be taken as an indication of lateral heterogeneity (due to the presence of domains differing in physical state and composition) [105] or could rather reflect location of the probe at different depths. [153] From the influence of the chemical structure of phospholipid head-groups and from the absence of very fast contributions (on the picosecond timescale) to solvent relaxation, some authors inferred that water molecules should not be intended as free, but rather as bound to the lipid headgroups. [112, 157, 168, 169] Another issue concerns hydrogen bonding: [135, 165, 170] it has been argued that a generic dipolar effect is not sufficient to produce fluorescence shifts as large as those observed in experiments, and the presence of two forms of the probe, H-bonded and non H-bonded, has been hypothesized, the former of which would be responsible for the emission at about 490 nm. A major point, to translate spectroscopic data into physical information on the system, is the location of the probe. [112] After several solvent relaxation studies and quenching experiments, there is lack of consensus on the distribution of Prodan and Laurdan in lipid bilayers. [160] Despite the presence of the same chromophore, differences in the behaviour of the two probes were evidenced by fluorescence [171] and FTIR studies. [161, 172] These were generally

ascribed to the different position of Prodan and Laurdan, which would be a consequence of the length of their acyl tail. From its stronger perturbation effect in the chain region [172] and its lower sensitivity to the type of polar headgroup, [171] Laurdan was inferred to reside deeper in the bilayer than Prodan. For the latter a heterogeneous distribution was proposed, [168] as well as a relocation between regions more or less rich in water upon changes in the bilayer organization, caused by phase transition. [153, 154, 161, 171, 172] There is also uncertainty on the nature of the emissive states. In particular, a long-term controversy is whether Prodan fluorescence occurs from a planar or from a twisted state. Abelt and coworkers [116] investigated the photophysical properties of several Prodan derivatives, where the dialkylamino group is constrained to be planar or perpendicular with respect to the naphthalene ring, by means of experimental solvatochromism studies. They found that constrained planar analogues behave just like Prodan, while twisted analogues behave very differently and, in addition, they have a pyramidal, rather than a planar, amino group. All this considered, they concluded that Prodan emission is from a planar ICT state. Several QM studies have been also carried out to characterize the electronic states of Prodan, its structure and spectroscopic behavior in various solvents. [87, 129, 130, 173]

In the previous Section we have unequivocally shown, with accurate QM approaches combined with different computational solvation models, that a twisted excited state is not necessary to explain both the large Stokes shifts and the large solvatochromism which characterize Prodan (and its analogues), but that a planar excited state involving a significant rearrangement of the electronic density properly describes all the specific spectroscopic signatures. It was shown that strongly interacting excited solute-solvent clusters are formed due to specific effects of H-bonding nature, which, when combined to longer-range solvent effects, are responsible for the significant red-shift found in the fluorescence of Prodan moving from a polar but aprotic solvent to a protic one. When fluorescent probes are embedded in lipid bilayers, further complications derive from the heterogeneous nature of the environment. On a nanometer length-scale there are dramatic changes of polarity, density, order and mobility, which affect the spectroscopic behavior both by determining

the location and orientation of the probes and by directly influencing the electronic transitions. Recently an extension of the PCM to interfaces (as described in Section 1.1.1) was proposed to take into account the effect of the non-uniform dielectric environment on the electronic states of the probe. Using such an approach, the dependence of the absorption and emission energies of Prodan on its position and orientation across the interface was explored; [131] however, the lack of information on the probe distribution in membrane precluded direct connection with experimental observables. Here we propose an integrated computational methodology, complementing the QM/PCM description of electronic transitions with a recent molecular field theory for the free energy of the probe in the lipid bilayer. [152] At both levels a consistent model of the bilayer is used, treated as a non-uniform and anisotropic continuum. In this way the molecularity of the solvent is lost; however, there is the advantage of a clear connection between the properties of the environment and their effects, at an affordable computational cost. Specific aspects of solute/solvent interactions, if needed, may also be introduced into this picture in a suitable way. Here we apply this integrated methodology to ACDAN, PRODAN and LAURDAN in a model dipalmitoylphosphatidylcholine (DPPC) bilayer; theoretical predictions are compared with literature experimental data in order to explain the observed spectroscopic signatures of these probes.

3.2.3 Results and Discussion

The Results and Discussion Section is organized in terms of separated Subsections on (i) QM/PCM fluorescence profile, (ii) free energy profiles and distributions and (iii) combination of QM/PCM and MFT approaches.

3.2.3.1 Free energy profiles and distributions

Figure 3.10 shows the water/bilayer transfer free-energy profile $u_{\Omega,\chi}(Z)$ and the corresponding position distribution function $P_{\Omega,\chi}(Z)$ calculated for ACDAN and Prodan in the S_0 and S_1 states, with Z being the position along the bilayer normal of the origin of the molecular frame, defined as in Figure 3.9. Practically identical results were obtained for conformers I and II of the probes.

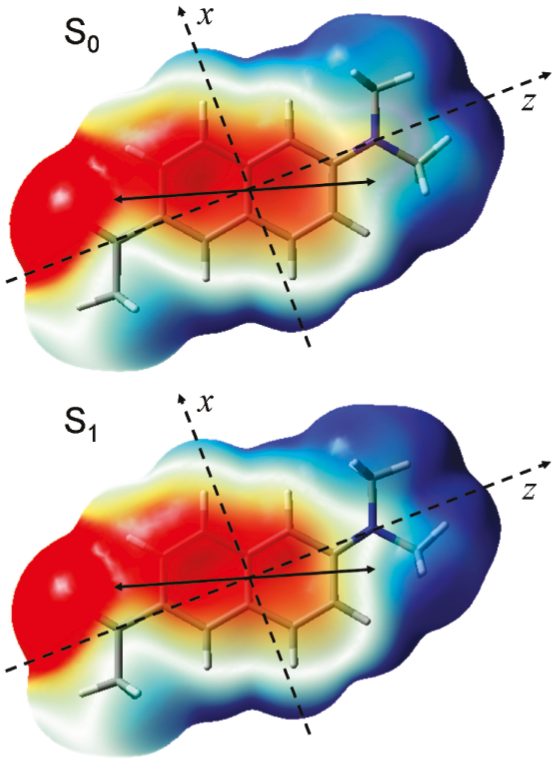

Figure 3.9: Molecular structure of the I conformer of ACDAN in the ground S_0 (top) and excited S_1 (bottom) states. The electrostatic potential is mapped on an isodensity surface (negative to positive from red to blue). Superimposed on each structure we show the molecular reference frames (dashed lines) and the transition dipole moments (solid arrows).

The free-energy profiles exhibit a well about 6-7 kcal mol^{-1} deep in the region between 10 and 19 Å from the bilayer midplane, slightly lower for Prodan than for ACDAN, with some difference between the ground and the excited states. The corresponding position distribution profiles indicate a preference of the two probes for locating the center of their naphthalene moiety near the hydrophobic/hydrophilic interface; vanishing probability in the central region of the bilayer is predicted. The excited-state distributions are a little narrower than those in the ground state, and their maximum is slightly shifted toward the polar region, which can be traced back to electrostatic effects. In fact, in agreement with experiment, [135] an increase of the molecular dipole moment, from about 6 to about 10 D, is predicted upon going from the ground to the excited state. As shown in Figure 3.9, this corresponds to an enhancement of the exposed charges on the electron-donor and - acceptor groups

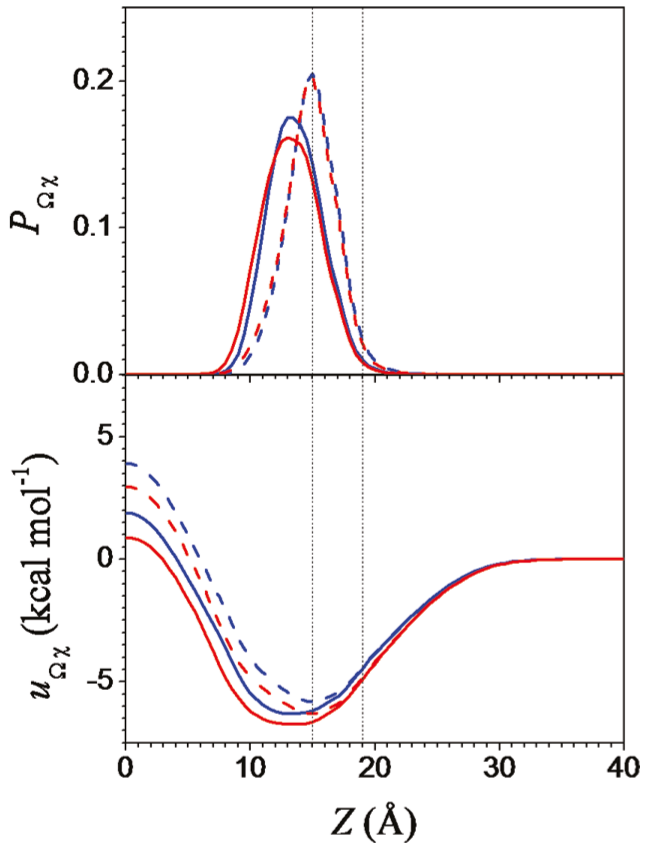

Figure 3.10: Transfer free energy $u_{\Omega,\chi}(Z)$ (bottom) and position distribution function $P_{\Omega,\chi}(Z)$ (top) calculated for ACDAN (blue line) and Prodan (red line) in the S_0 (solid line) and S_1 (dashed line) states as a function of the position of the center of the molecular frame across the lipid bilayer. The coordinate $Z = 0$ corresponds to the bilayer midplane; the vertical lines indicate the average position of the carbonyl and phosphate groups of lipid molecules. Given the symmetry of the system, only one-half of the bilayer is shown.

in the chromophore.

The analysis of the different contributions to the mean-field potential (see Appendix B), shows that dispersion interactions are the main determinants of the partitioning of ACDAN and PRODAN in the bilayer; in their absence, the free-energy profile would be nearly flat and would only exhibit an appreciable increase for insertion of the probes deep in the bilayer core due to the energetic cost associated with charges buried in the apolar region. Electrostatic interactions are relatively weak but have a peculiar effect by stabilizing positions and orientations that allow the exposed charges, which are mainly located in the carbonyl and in the amino groups, to reside close to water. The location of the probes close to the

hydrophilic/hydrophobic interface is also promoted by a drop in the lateral pressure of the bilayer, [174] which favors the formation of a molecular cavity in this region. Anisotropic interactions with the acyl chains stabilize orientations of the long molecular axis nearly parallel to the bilayer normal and insertion in the most ordered region, with the result of slightly broadening the position distribution of the probes.

Figure 3.11 shows the orientational probability distribution calculated for the conformer I of Prodan in its preferred position in the S_0 and S_1 states. The plots show a strong anisotropy, with a pronounced tendency of the molecule to keep the naphthalene plane perpendicular to the bilayer surface.

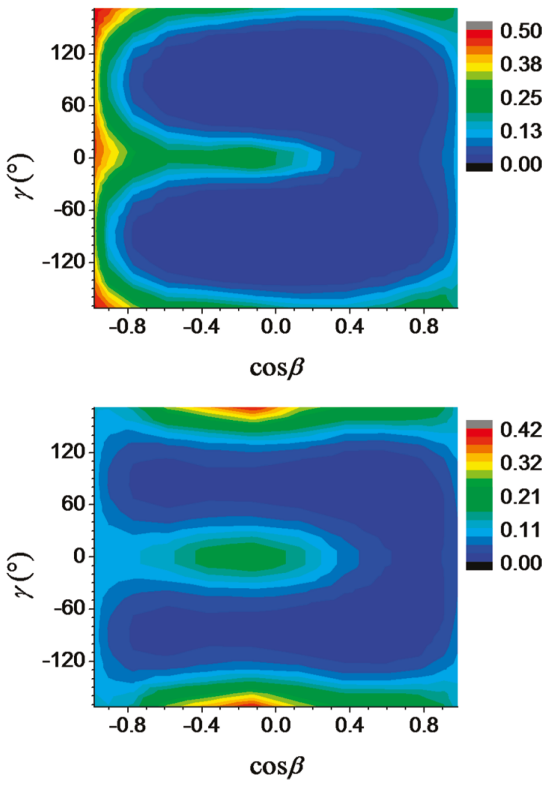

Figure 3.11: Orientational probability distribution calculated for conformer I of Prodan in the S_0 (top) and S_1 (bottom) states, at distances of 13.5 and 15.0 Å from the bilayer midplane, respectively. β is the angle between the bilayer normal and the molecular z axis, and γ defines a rotation around this axis (for $\gamma = 0$ and 180, the naphthyl plane is perpendicular to the bilayer surface).

The probe in the ground state preferentially aligns its long axis parallel to the bilayer normal, with the carbonyl or, to a lesser extent, the dimethylamino group

pointing toward water. In the S_1 state, the perpendicular orientation is stabilized over the parallel, with the carbonyl either pointing toward water or, with a lower probability, toward the bilayer core. This can be ascribed to the increased charges on exposed atoms because the horizontal alignment allows the molecule, as a whole, to reside in a more polar environment. The orientational distribution of ACDAN exhibits analogous features, except for an even more pronounced preference for directing the C=O group toward water due to the weaker hydrophobic character of its acyl end.

We collect in Figure 3.14 the preferred orientations of the chromophore, represented for ACDAN, as obtained from the analysis just discussed. These orientations will be henceforth denoted as **VU** (vertical, C=O up, $\cos\beta = 1$), **VD** (vertical, C=O down, $\cos\beta = 1$), **HU** (horizontal, C=O up, $\cos\beta = 0$ and $\gamma = 180$), and **HD** (horizontal, C=O down, $\cos\beta = 0$ and γ=0).

In the case of Laurdan, the long acyl chain significantly affects the interaction with the lipid bilayer. Figure 3.12 shows the transfer free-energy profile $u_{\Omega,\chi}(Z)$ and the probability distribution $P_{\Omega,\chi}(Z)$ in the S_0 and S_1 states, calculated by averaging over all conformers.

A free energy well about 11 kcal mol^{-1} deep is predicted, the lauroyl tail being responsible for the greater affinity of this probe for the membrane environment in comparison to the shorter-chain homologues. The distribution of the chromophore moiety reaches its maximum at the hydrophobic/hydrophilic interface and is broadened by the contribution of different conformers. A distinction between L-shaped (like I in Figure 3.14) and elongated conformers (like II in Figure 3.14) emerges from the conformational analysis, the former being generally stabilized and characterized by a narrower distribution in the bilayer. As for Prodan and ACDAN, even for Laurdan, the position distribution is predicted to slightly narrow and shift toward the bilayer surface upon going from the ground to the excited state due to the increase of exposed charges, which anchor the chromophore to the bilayer head group region.

L-shaped conformers of Laurdan are found to preferentially align the aromatic plane parallel to the acyl chains, with the long naphthalene axis perpendicular to the bilayer normal (**HU** orientation). In this way, they can direct the polar carbonyl

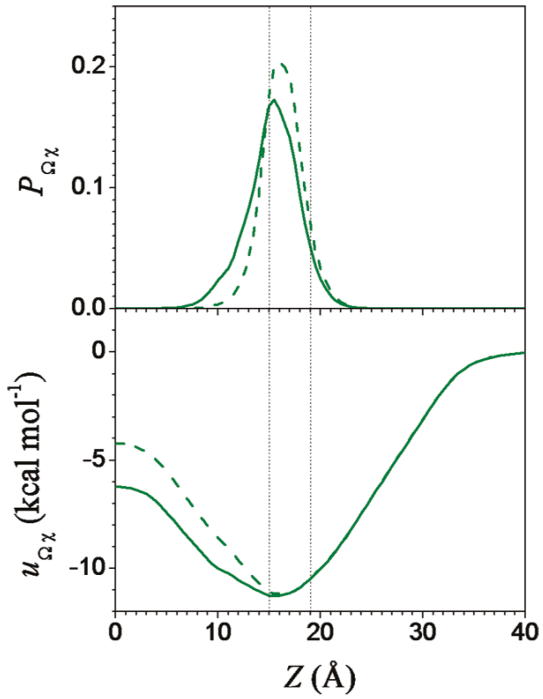

Figure 3.12: Transfer free energy $u_{\Omega,\chi(Z)}$ (bottom) and position distribution function $P_{\Omega,\chi(Z)}$ (top) calculated for Laurdan in the S_0 (solid line) and S_1 (dashed line) states as a function of the position of the center of the molecular frame across the lipid bilayer. The coordinate $Z = 0$ corresponds to the bilayer midplane; the vertical lines indicate the average positions of the carbonyl and phosphate groups of lipid molecules. Given the symmetry of the system, only one-half of the bilayer is shown.

group toward the hydrophilic region and bury the apolar tail in the hydrophobic core of the bilayer. As an example, we show in Figure 3.13 the orientational distribution calculated for the most stable of the conformers in its ground state, in the most probable position; a very similar plot was obtained for the excited state.

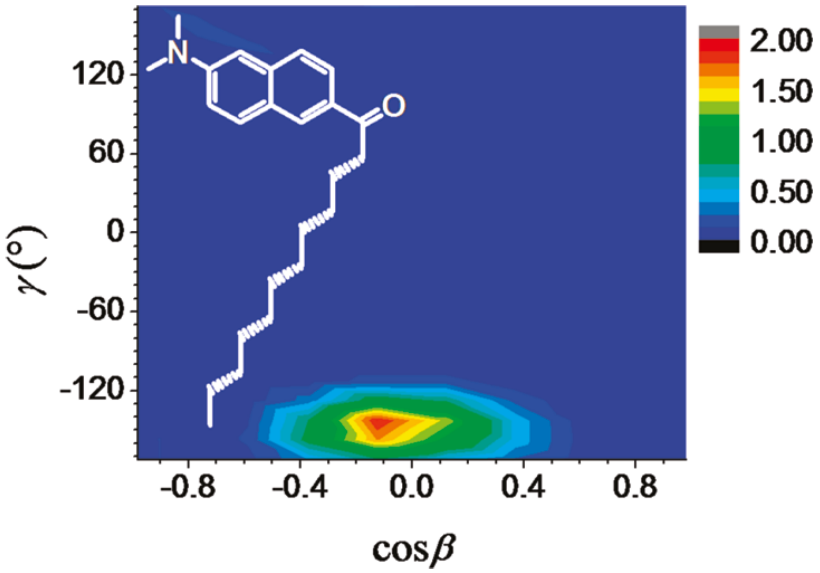

Figure 3.13: Orientational probability distribution calculated for an L-shaped conformer of Laurdan in the S_1 state at Z = 15.5 Å . β is the angle between the bilayer normal and the molecular z axis, and γ defines a rotation around this axis (for γ = 0 and 180, the naphthyl plane is perpendicular to the bilayer surface).

More elongated conformers either align their long naphthyl axis roughly parallel to the bilayer normal (VD orientation), locating their carbonyl below the hydrophobic/hydrophilic interface, or tilt to bring it closer to the polar region of the bilayer. Because neither of these configurations optimizes electrostatic and anisotropic interactions at the same time, elongated conformers are found to be destabilized in the liquid-crystal phase of the bilayer.

Distributions similar to those shown in Figures 3.10 and 3.12, and analogous changes upon excitation, were recently reported from molecular dynamics simulations of Prodan and Laurdan in a liquid-crystalline DOPC bilayer; [175] there, no information was extracted on the orientational and conformational distribution of the probes, probably due to the long simulation times required for a meaningful sampling of these degrees of freedom.

3.2.3.2 QM/PCM fluorescence profile

In this Subsection we report the fluorescence profiles obtained for ACDAN using the QM/PCM approach. The position of the probe was varied through the whole bilayer half-thickness, while only few orientations of the chromophore were considered, shown in Figure 3.14, which were selected on the basis of the orientational distributions of the probes.

In Figure 3.15 we report (line-circles) the fluorescence emission wavelength calculated as a function of the position of the center of the molecular frame across the lipid bilayer. We can see that the emission is red-shifted by about 40 nm as the chromophore moves from the bilayer core to water and has some dependence on the probe orientation. At a given position, the emission wavelength increases as more charges reside in a polar environment and, for the same alignment, probes with the carbonyl group pointing towards water (**VU** and **HU**) are predicted to emit at longer wavelength than those exposing the amino group (**VD** and **HD**).

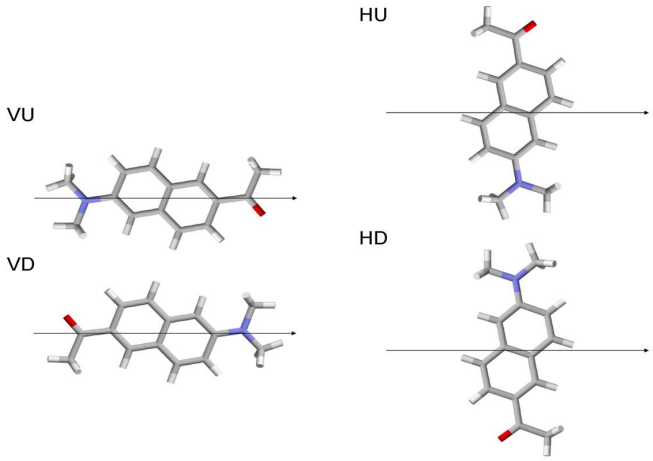

Figure 3.14: Orientations of the 6-acetyl-2-(N,N-dimethylamino)naphthalene chromophore with respect to the normal to the bilayer, selected on the basis of our analysis of the orientational distribution in the lipid bilayer (shown for ACDAN). Arrows indicate the bilayer normal (pointing towards water).

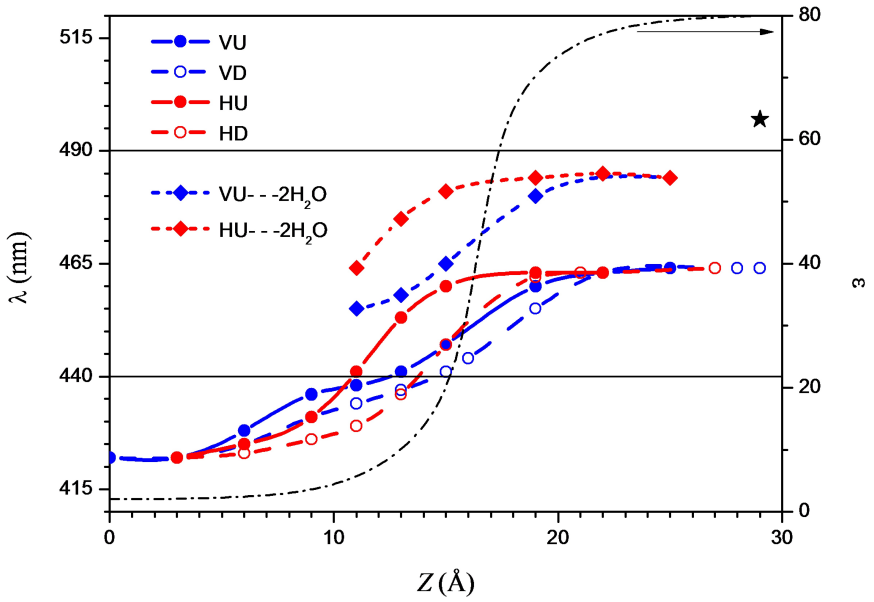

Figure 3.15: Fluorescence emission wavelengths calculated for conformer I of ACDAN in the different alignments/orientations shown in Figure 3.14, as a function of the position of the center of the molecular frame across the lipid bilayer. Fluorescence emission wavelengths calculated for ACDAN + 2 H-bonded waters in the alignments **V** and **H**, with orientation **U** (Figure 3.14) are also reported. The star shows the wavelength in bulk water, as obtained by a QM/MM approach including polarization. [104] The horizontal lines indicate experimental values for Prodan and Laurdan in lipid bilayers. [156] The dash-dotted line shows the profile of the position dependent dielectric permittivity, assumed in calculations. For symmetry reasons, only one half of the bilayer is shown.

For the preferred locations of the probes (see figure 3.10 and 3.12), emission wavelengths in a range including the experimental blue-shifted emission, at about 440 nm, [156] are obtained. On the contrary, the red-shifted wavelength, experimentally observed near 490 nm, is even above that estimated for the probes in bulk water. To explain such findings we have to recall that these results were obtained by a purely continuum model, which means that specific HB effects are not explicitly included. The previous chapter on solvatochromism of Prodan and other analogous probes, [104] has shown that in protic solvents, and in particular in water, the observed fluorescence wavelength is the result of a delicate combination of short-range (H-bonds) and long-range (polarity) solvent effects. By comparing different solvation models it was shown that, to obtain a good estimate of the fluorescence wavelengths in those solvents, a more refined approach has to be introduced by using

extended QM/MM clusters. In Figure 3.15 the wavelength estimated for Prodan in bulk water by such a QM/MM approach including polarization [104] is also shown (star). An alternative strategy is to use smaller clusters of solvent molecules around the probe, but including long-range effects with an external continuum dielectric. In the case of Prodan in water, we have shown in the previous chapter that at least two water molecules H-bonded to the carbonyl oxygen are required, being the carbonyl group the site involved in stronger H-bonds. [104]

The presence of H-bonds can be expected also for our probes in lipid bilayers, at least when the carbonyl group resides in regions where water penetration is not negligible. Therefore we have repeated the QM/PCM calculations for the fluorescence profiles of ACDAN H-bonded to two water molecules inside the lipid bilayer. Both the alignments **V** and **H** were considered, with orientation **U**, in which the CO group points outwards. The emission wavelength profiles obtained in this way are reported in Figure 3.15 (line-diamonds). We can see that the presence of H-bonds yields a significant increase of the emission wavelength, leading the calculated values very close to the red-shifted experimental wavelength.

3.2.3.3 The combination of QM/PCM and MFT approaches

The results of the MFT calculations provide detailed insights into the distribution of the probes in lipid bilayers, both in the ground and in the excited state, which generally are not accessible by experiments, since these report on suitably time- and space-averaged properties.

Our calculations show the orientational and conformational preferences of the probes, which are generally ignored in the literature, where the representation of the chromophore in the 'upright' orientation (**VD** in Figure 3.14) is adopted and the most extended 'rod-like' conformation of Laurdan is assumed. For ACDAN and Prodan we have evidenced the existence of two preferential orientations, one parallel (or Vertical, **V**) and the other perpendicular (or Horizontal, **H**) to the bilayer normal; the former is promoted by the dispersion and anisotropic interactions in the apolar region of the bilayer, while the latter is favored by electrostatic interactions. The orientational distributions obtained by MFT calculation shows, that a change

from vertical to horizontal is predicted for the preferred orientation of ACDAN and Prodan, along with relocation closer to the hydrophobic/hydrophilic interface, on going from the ground to the excited state, as a consequence of the increased dipole. Even though the lifetime of fluorescence, of the order of nanoseconds, it may not be sufficient for the probe to reach its equilibrium distribution in the excited state, this change may affect the emission spectra of ACDAN and Prodan, as well as solvent relaxation. We expect the competition between preferential parallel and perpendicular orientations to be a general feature of polar dyes with elongated aromatic planes; the one or the other orientation would dominate, depending on the state of the lipid bilayer and the polarity of the chromophore. This result is compatible with single molecule fluorescence experiments [176] and two-photon excitation fluorescence microscopy [108, 177]. Thus, the differential emission in the gel and liquid crystal phase would reflect a change in the conformational distribution of Laurdan, and then in its orientational preference, between the two phases.

The spectroscopic behavior of the fluorescent probes under investigation in lipid membranes is often described in terms of probe configurations more or less accessible to water: solutes embedded in the interior of the bilayer would be responsible for the emission at about 440 nm, close to that observed for the same probes in apolar isotropic solvents; [88, 102, 103] and also to the emission of aggregates in aqueous environment. [143, 178, 179] Emission would be shifted at longer wavelengths for probes in the polar region. Our QM calculations have shown that hydrogen bonds with water molecules involving the carbonyl oxygen of the chromophore are needed to yield the large Stokes shifts corresponding to the emission observed at about 490 nm. The positional profiles, calculated as averages over all the conformers and orientations, are shown in Figure 3.16, together with the density profile of water through a model liquid-crystalline DPPC bilayer. [180]

These profile show that for all the probes, the distribution of carbonyl oxygen spreads from the polar head-group region, where water is abundant, to the apolar tail region, where the amount of water becomes negligible. Assuming that H-bonds are the major responsible for the large Stokes shifts, their effects on the emission bands will increase with the water accessibility of the carbonyl oxygen.

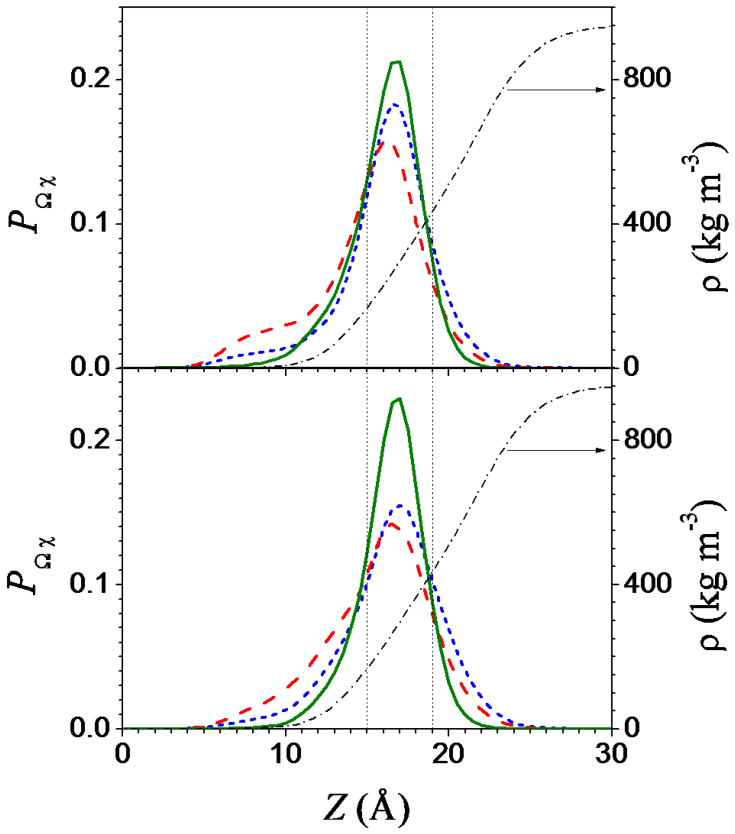

Figure 3.16: Position distribution $P_{\Omega,\chi}(Z)$ calculated for ACDAN (blue short-dashed), Prodan (red dashed) and Laurdan (green solid), in the S_0 (top) and S_1 (bottom) states, as a function of the position of the oxygen atom of their carbonyl group across a DPPC bilayer. The density profile of water [180] is shown for comparison (dash-dotted line). The coordinate Z = 0 corresponds to the bilayer midplane; the vertical lines indicate the average position of carbonyl and phosphate groups of lipids. Given the symmetry of the system, only one half of the bilayer is shown.

The range of emission wavelengths due to probes in different positions and orientations can be discussed in the light of the results of our QM calculations reported in Figure 3.15. The tails of the carbonyl distributions in Figure 3.16 correspond to probes in the 'upright' orientation (**VD**), in which the carbonyl group is buried in the apolar region of the lipid tails; in the case of Laurdan, only the most extend conformers will contribute. These probes will not be involved in H-bonds and their emission wavelength is predicted to span a range between 430 and 450 nm, in close agreement with the experimental reference value of 440 nm for the blue-shifted component of the emission spectrum. In the same range also non-H-bonded chromophores in the **VU** and **HU** (and **HD** when significant) orientations, whose

carbonyls are located below the hydrophobic/hydrophilic interface in Figure 3.16, are predicted to emit. H-bonded chromophores in the same orientations will emit at longer wavelengths: in the range between 455 and 465 nm for **VU** probes, between 475 and 480 nm for **HU**/**HD** probes, closer to the red-shifted component of the experimental emission spectrum at about 490 nm. Some underestimate of the red-shift, 500 against 520 nm (Figure 3.15), was also obtained for Prodan in bulk water (see Subsection 3.1.3); this can be ascribed to some still missing effects in the QM simulation to be directly compared with the measured spectra, for example vibronic effects are completely neglected.

These results suggest a common origin of the features of the fluorescence spectra recorded in lipid membranes for the short- and long-tail probes. In the case of Laurdan, the positional heterogeneity of the carbonyl group is accompanied by a conformational distribution: the carbonyl oxygen of L-shaped conformers would be more or less exposed to water, depending on probe position, and then more or less involved in H-bonds, whereas that of elongated conformers would be buried in zones scarcely accessible to water. Elongated conformers, which are more ordered and are likely to reorient more slowly their transition dipole, might be responsible for the significantly higher steady-state fluorescence anisotropy observed at 440 nm than at 490 nm, a result which was not explained. [160] Somehow surprisingly, the role of molecular flexibility is generally disregarded when discussing the behavior of Laurdan in lipid bilayers. In fact, the acyl chain conformation is expected to have a scarce influence on the electronic transitions of Laurdan, since these essentially involve the chromophore moiety. However the positional distribution show that the chain conformation can affect the fluorescence emission in an indirect way, by determining the location and orientation of the chromophore inside the bilayer.

The relative weight of the long- and short-wavelength contributions in the emission spectrum will be affected by the physical state and the chemical composition of the bilayer: temperature, pressure, nature of lipid head-groups, length and unsaturation of acyl chains, presence of perturbing agents, affecting probe partition and water penetration in the bilayer. The stabilization of the elongated conformers of Laurdan in the gel phase, suggested by the two-photon excitation fluorescence mi-

croscopy experiments mentioned above, [177] is in agreement with the dominating blue emission observed in this condition. [156]

3.3 Molecular probes intercalated in nucleic acids

This Section deals with the modelling of environment effects on the absorption and fluorescence properties in intercalated[1] fluorescent probes in single- and double-strand nucleic acids.

The leading new generation approaches in the frame of biochemical and biophysical sensing make use of fluorescence-based detection because of its high sensitivity, simplicity, and diversity. For instance, fluorescence resonance energy transfer (FRET), [183] fluorescence correlation spectroscopy (FCS) [184] and single-molecule-FRET [185] measurements are nowadays major tools for the analysis of complex biochemical reactions, whereas engineered fluorescent dyes are used to selectively detect particular nucleic acid sequences. [186–188] When fluorescent probes are used to bind to polynucleotides or sense different chemical environments a very desirable characteristic of the chosen dye is that it could behave as a "light-switch". [188–190] This means that the probe fluorescence emission should dramatically change depending on conditions, as outside vs. inside slot in DNA, [188, 190] pH variation, [191] presence or absence of selected metal ions. [192] Among the large variety of molecules displaying non-covalent binding modes, cyanine dyes are widely used as fluorescent probes for polynucleotides, [193–195] this application being connected with the interesting property of cyanines to sharply increase their fluorescence upon interaction with polynucleotides. [193,196,197] On the other hand, it is known that cyanine dyes tend to self-aggregate, [198–205] and this process can influence the course of dye binding to a given substrate. Despite the unquestionable importance of fluorescent dyes, theoretical studies, aimed to an in-depth understanding of the photophysical characteristics of these molecules, are still limited. [206–208] In all cases, at the best of our knowledge, the effects of different environments have never been considered in a detailed way. For these reasons we have undertaken a QM study of the absorbance

[1]The term "intercalation" was firstly proposed by Lerman in 1961 [181,182].

and fluorescence emission characteristics of the cyanine thiazole orange (TO, Figure 3.17) in environments of increasing complexity. First we have considered homogeneous solutions by simulating their effects in terms of a polarizable continuum model (PCM), [47] after we have introduced aggregation effects, and finally we have analysed intercalation of TO into single and double stranded DNA.

The choice of TO is easily understood by recalling that it is a widely used DNA fluorescent probe [196, 209–215], because it is able to ''switch on'' fluorescence when buried into a hydrophobic cavity; in fact it is essentially non-fluorescent in non-viscous solvents, whereas the fluorescence switches on in viscous solvents [196, 216, 217] or upon intercalation in rigid environments, such as dsDNA (fluorescence increase by more than 1000 times) [196, 216–220] , RNA (3000-fold increase) [215], ssDNA (100-fold increase) or fibrillar protein [221]. These observations suggest that TO can indeed be a very good system for computational models to understand and rationalize the important changes induced by different environments on the fluorescence of molecular probes. Here, the environment not only affects the position of the spectroscopic bands but it can also induce a quenching or an enhancement of the signal due to a complex combination of intramolecular twisting, aggregation effects, and structural impediments. Thus, in addition to common quenching mechanisms due to water molecules and hydrophobic effects that were found to play a non-negligible role in similar fluorescent dye systems, [222] this study provides clear evidences about the presence for this particular system of a quenching mechanism due to the twisting of the rings around the central methine bridge. Its structure is reported in Figure 3.17.

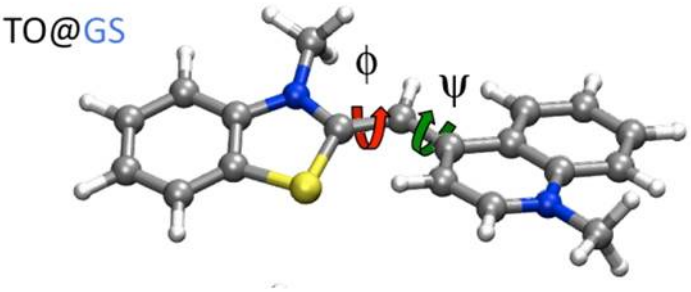

Figure 3.17: The optimized ground state structure of Thiazole Orange (TO)

3.3.1 Computational Details

All the QM calculations have been performed by using a locally modified version of the Gaussian 09 package. [66] The models used in the calculations represent: (i) a single molecule of TO in the gas-phase and in a PCM solvent; (ii) three structures of π-stacked dimers, (iii) two systems where TO is intercalated in a double stranded DNA pocket, and (iv) four systems where TO is intercalated in a single stranded DNA pocket. In particular, concerning dsDNA, two models have been built up, namely the ''Sandwich'' (Sand) and the ''Ring'' systems. All the geometry optimizations of both monomers and dimers were performed without imposing any constraint, while in the case of intercalated systems the geometry of DNA (in its Ring or Sand forms) was kept fixed. The ground and excited state geometry optimizations were calculated with the (TD)DFT method using the M06-2X functional. [67] This functional was chosen for its ability to describe noncovalent interactions such as stacking effects as those determining dimerisation in TO. [68,69] The absorption and emission calculations were calculated with the CAM-B3LYP functional. [90] The 6-311+G(d,p) basis set was used for all the calculations performed on the monomers and dimers of TO. In the intercalated systems, the combination of 6-311+G(d,p) and 6-31G basis sets was used for the calculations on TO (high level) and ring/sand (low level) structures, respectively. The IEF-PCM (see Section 1.1.1.1) has been used to describe the effects of the environment both on the ground and the excited states. PCM cavities have been built as a series of interlocking spheres centered on atoms with Bondi radii: [45] 1.7Å for quaternary C, 1.9Å for aromatic CH, 2.0Å for CH_n (n = 2, 3), 1.6Å for N and 1.2Å for H not bonded to C, all multiplied by a cavity size factor of 1.2. PCM vertical absorption and emission energies were obtained by exploiting the corrected linear response (cLR) scheme (see Section 1.2).

3.3.2 Results and Discussion

The Results and Discussion Section is organized in terms of separated Subsections on (i) monomers and dimers in solution and (ii) influence of intercalation on photophysical properties of TO.

3.3.2.1 Monomers and dimers in solution

To understand the important changes in the photophysical behavior of TO when in the presence of different environmental conditions, we have first analyzed the geometrical structures of both ground and excited states of the isolated and solvated TO monomer and dimer using a (TD)DFT approach combined with a PCM description of the solvent. From now, if not explicitly indicated, the excited state refers to the first singlet excited state of π–π^* nature.

As changes in the fluorescence quantum yield of TO have been attributed to intramolecular torsions [217, 223] the structural analysis has been focused on the two main dihedral angles, namely the two torsional angles between the benzothiazole and the quinoline heterocycles.

The optimized dihedral angles of TO in the gas-phase and in water solution are reported in Table 3.6 whereas the optimized structures for the monomer and the investigated dimers are reported in Figure 3.18. In particular, three different dimeric structures have been investigated; they are all stacked dimers but they differ with respect to the portions of the aromatic system which are allowed to interact.

TO System	Environment	GS		ES	
		ϕ	φ	ϕ	φ
monomer	vacuo	11	15	0	95
monomer	water	10	17	1	92
dimer1	water	4	9	9	21
dimer2	water	8	9	-	-
dimer3	water	4	12	-	-

Table 3.6: Values assumed by dihedral angles ϕ and φ (degrees) obtained from the optimized geometries of the ground (GS) and first excited (ES) states for the monomer and the three different dimeric structures reported in Figure 3.18.

We note that among the different dimeric structures, the H-aggregate (dim1) is found to be the most stable form (with energy more than 7 kcal/mol lower than the two other forms), in agreement with previous literature findings. [205, 216] For this reason, dim2 and dim3 were not considered any further in the study of the photophysical properties. As shown in the previous Subsection, the values of the reaction enthalpy and entropy found for TO dimerisation are considerably more

negative than those found for other dyes. [222] This finding could be rationalized in the light of the structure of dim1. In such an H-aggregate the stabilizing dispersion interactions are maximized (due to the large extension of the overlap of the aromatic portions of each TO) while the repulsive forces between the two positively charged TO are minimized thanks to the antiparallel arrangement. In addition, the same stabilizing interactions lead to a structure in which twisting processes among the two dihedral angles indicated in Figure 3.18 are strongly reduced.

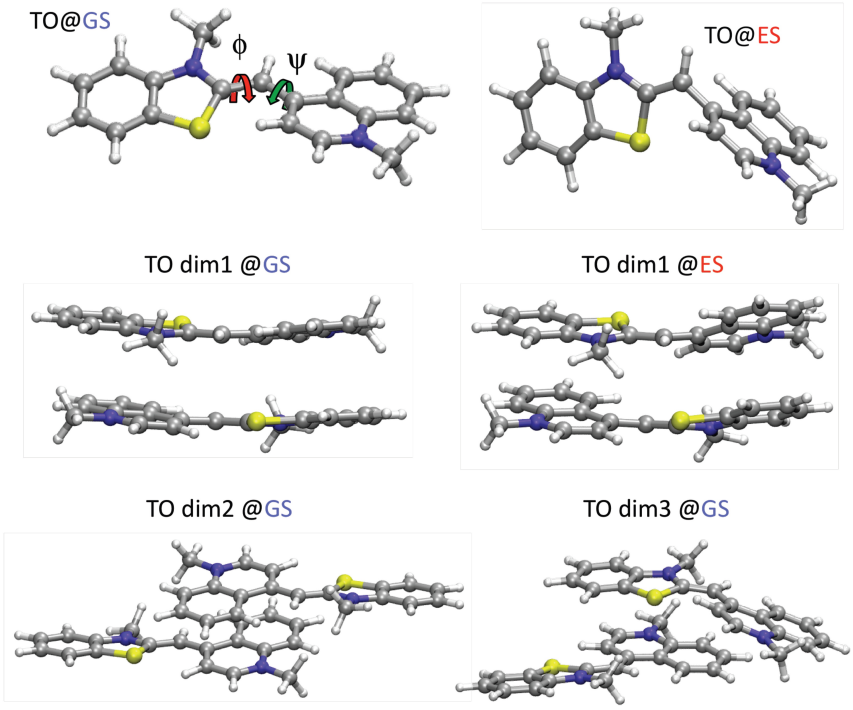

Figure 3.18: Optimized molecular structures of the ground (GS) and first excited (ES) states relative to TO monomer and various TO dimers in water, together with the labelling used to identify two relevant dihedral angles (φ,ψ) investigated in this work.

The suggested relation between torsional angles and photophysical properties has been further analyzed in Figure 3.19 where we report the calculated emission energies for the first two excited states of solvated TO as a function of the dihedral angle ψ.

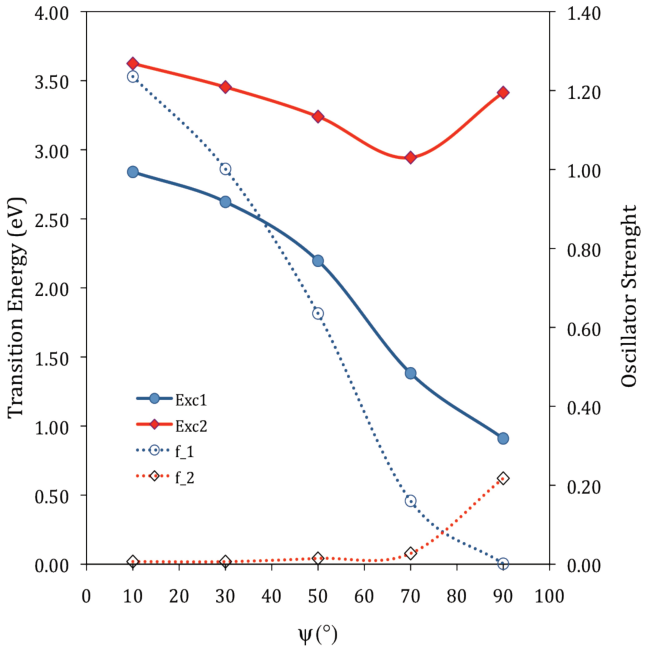

Figure 3.19: Emission energies of TO as a function of the dihedral angle ψ (φ = 10°) for the first two singlet excited states (Exc1 and Exc2) of TO in water; their oscillator strengths are also shown as open labels. For each value of ψ, all the other geometrical parameters have been optimized.

It is in fact a torsion with respect to this angle which, in the geometry optimization of the excited state, has lead to intramolecularly twisted structures while changes of the dihedral angle ϕ were almost negligible. This plot shows a clear relation between the torsional angle ψ and the emission energies as well as the oscillatory strengths. The emission energy of the lowest state drops rapidly with increasing angles and the state becomes completely dark when TO is fully twisted. An opposite trend is instead found for the second state for which both the emission energy and the oscillator strength increase for angles larger than 70°. This behavior can be explained in terms of a loss of conjugation between the benzothiazole and quinoline ring. Moving now to spectroscopic features, in Table 3.7 and 3.8 and we report the calculated absorption and emission energies, and the corresponding Stokes shifts of the TO monomer and dimer, respectively. In both cases, a collection of available experimental data is also shown.

Environment	ABS	FLU	SS	Ref.
Water and 0.1M NaCl	2.47	-	-	[205]
Water and 0.1M NaCl	2.48	2.37	0.11	This work
Tris-HCl buffer	2.47	2.32	0.16	[216]
Tris-HCl buffer	2.47	2.27	0.20	[219]
Tris-EDTA buffer	2.48		-	[218]
Hepes buffer	2.46	-	-	[221]
Methanol	2.48	-	-	[223]
Methanol	2.47	-	-	[217]
TE buffer	2.46	-	-	[224]
90% Glicerol	-	2.27	-	[217]
<Exp>	2.47	2.31	0.16	
TDDFT in vacuo	3.03	Twist	-	This work
TDDFT in water	3.04	Twist	-	This work

Table 3.7: Comparison between experimental and TDDFT calculated absorption (ABS), emission energies (FLU) and Stokes shifts (SS) of the TO monomer in several solvents. All values are in eV.

Environment	ABS	FLU	SS	Ref.
Water and 0.1M NaCl	2.63	-	-	[205]
Water and 0.1M NaCl	2.64	-	-	This work
Water and 3M NaCl	2.61	2.00	0.61	This work
Tris-HCl buffer	2.63	1.95	0.68	[216]
Tris-HCl buffer	2.62	2.02	0.60	[219]
Tris-EDTA buffer	2.63	-	-	[218]
TAE buffer	-	1.94	-	[196]
<Exp>	2.63	1.98	0.63	
TDDFT in water	3.09	2.54	0.55	This work

Table 3.8: Comparison between experimental and TDDFT calculated absorption (ABS), emission energies (FLU) and Stokes shifts (SS) of the TO dimer (dim1). All values are in eV.

As can be seen from Tables 3.7 and 3.8, the calculated transition energies always overestimate the measured ones but it is important to note that such an overestimation is almost constant for absorption and fluorescence on the one side, and for the monomer and dimer, on the other side. This means that we can use this constant error (ca. 0.5 eV) as an offset for the selected QM level of calculation, and focus our analysis on scaled values without loosing reliability in our study. As a matter of fact, the calculated Stokes shift for the dimer which, is not affected by the intrinsic inaccuracy of the QM level inducing the 0.5 eV offset is in good agreement with the

experiments.

If we consider first the monomer, we recall that either in the gas-phase or adding the effects of water through a PCM description, the excited state structure relaxes to a twisted one in which the fluorescence is completely quenched (as shown by the graphs of the oscillatory strengths reported in Figure 3.19). These results show that when TO is free to rotate around the dihedral angle ψ, like in solvents with low viscosity, a large reduction, if not a complete quenching, of the fluorescence has to be expected. Here, to quantify the effects of a very viscous solvent, we can go back to the plot reported in Figure 3.19. If we assume that the viscosity of the solvent will impede significant torsional motions, we can get an estimated emission energy for c close to the value optimized in the ground state structure (i.e. ca. 15°). If we shift this value by the 0.5 eV offset we obtain an energy of ca. 2.3 eV, in quite good agreement with the value measured in water and 3 M NaCl (2.37 eV).

If we now assume that aggregation phenomena are possible, e.g. for high TO concentrations, PCM calculations on the dimer show that fluorescence is kept without imposing any constraint on the geometrical parameters and the resulting emission energy is red-shifted with respect to the signal observed in the viscous solvents. This is confirmed by the present experimental analysis.

Finally, it is worth noting that the measured Stokes shift in the aggregated system (0.63 eV) is almost completely reproduced by calculations on dimers (0.55 eV) showing that the dimeric model gives a reliable picture of changes in the excitation process due to aggregation.

3.3.2.2 Influence of intercalation on photophysical properties of TO

Because of the large size of the system, we modelled the double stranded DNA (dsDNA) intercalation pockets using simplified models which limit the interaction between TO and the dsDNA to the first neighbourhoods. Since experimental results have shown that photophysical properties of TO are similar to those of its homodimeric TOTO analog, [196] we have assumed that the structure of the intercalated TO is likewise similar to that of the intercalated TOTO. Therefore, two intercalated TO configurations were derived from the two arrangements of TO in

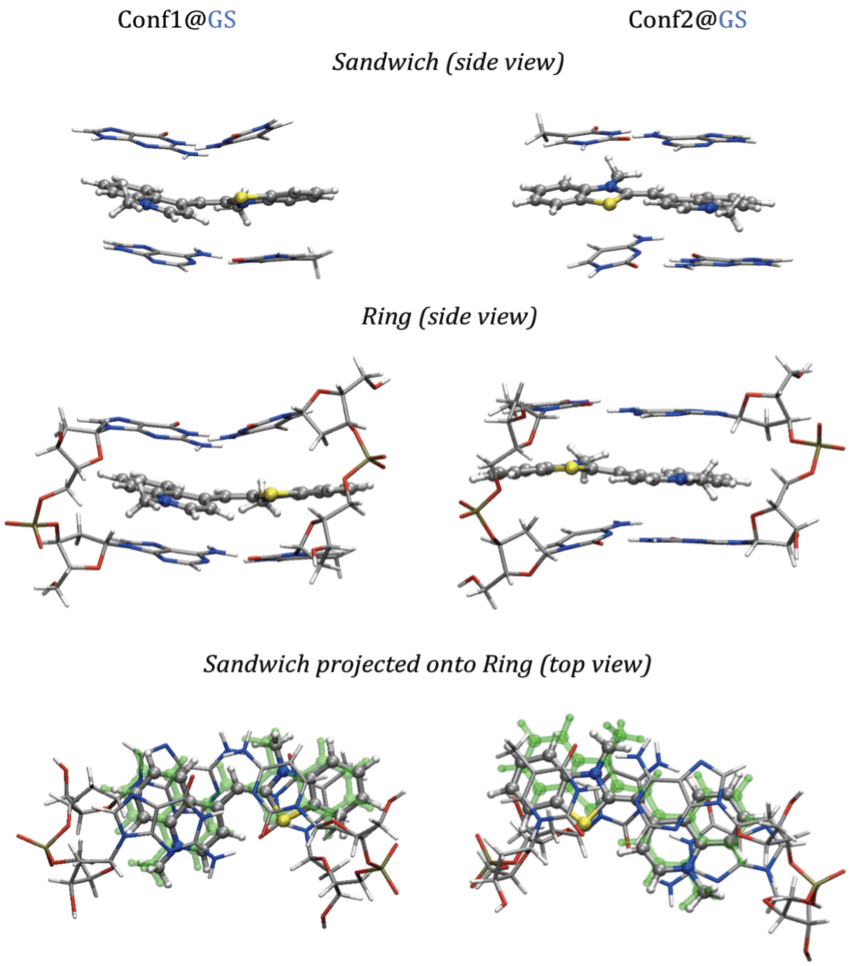

Figure 3.20: Optimized molecular structures of TO intercalated in double stranded DNA in the two investigated configurations ''Conf1'' (left) and ''Conf2'' (right). Sandwich and Ring forms are reported together with their superimpositions.

the intercalated homodimer obtained by Spielmann et al. [225] with an 1H-NMR structural study on TOTO binding to d(CGCTAGCG)$_2$ in the CTAG site. From these two configurations (from now on indicated as Conf1 and Conf2), two model systems have been defined. The smallest model (Sandwich) is obtained by eliminating the whole DNA structure with exception of the four adjacent nucleic acid bases (two above and two below the TO plane), while in the larger model (Ring) also the sugar/phosphate groups connecting those bases have been kept. The ground state optimized structures for the two sets of model systems are shown in Figure 3.20 whereas the superimposition with the corresponding excited state structures is shown in Figure 3.21.

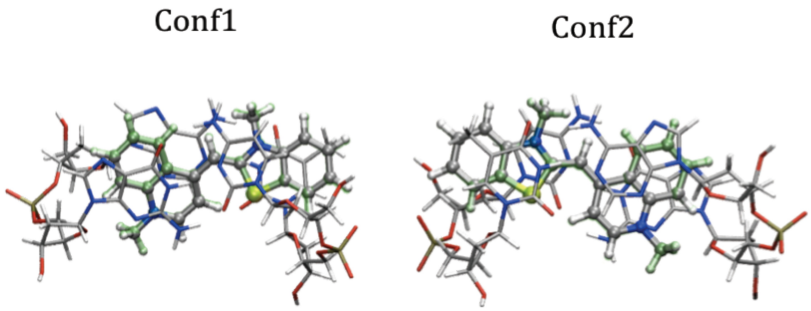

Figure 3.21: Comparison between optimized ground and excited state (in green) structures of dsDNA-intercalated TO in the Sandwich model.

The experimental and calculated absorption, emission energies and Stokes shifts of the TO intercalated in double stranded DNA are reported in 3.9. As for the calculated values, only the results obtained for the ring model are reported as the analogous results obtained for the sandwich were not comparable with experiments. This shows that a reliable description of the short range interactions between TO and the DNA pockets at least requires to include the effects of the lateral sugar/phosphate chains in addition to the stacking bases.

Environment	ABS	FLU	SS	Ref.
ctDNA	2.44	2.35	0.09	[196]
ctDNA	2.43	2.35	0.08	[205]
ctDNA	2.46	2.35	0.12	[217]
ctDNA	2.45	2.32	0.13	[216]
ctDNA	2.44	2.36	0.08	[218]
ctDNA	-	2.35		This work
Salmon DNA	-	2.30	-	[219]
Poly(dA-dT)$_2$	2.44	2.31	0.13	[220]
Poly(dG-dC)$_2$	2.43	2.35	0.08	[218]
Poly(dG-dC)$_2$	2.44	2.31	0.13	[220]
<Exp>	2.44	2.34	0.10	
TDDFT in vacuo Ring/Conf2	2.95	2.76	0.18	This work
TDDFT in vacuo Ring/Conf2	2.91	2.71	0.20	This work
TDDFT in PCM($\epsilon = 4$) Ring/Conf2	2.95	2.75	0.20	This work
TDDFT in PCM($\epsilon = 4$) Ring/Conf1	2.90	2.68	0.22	This work
TDDFT in PCM($\epsilon = 4$) Ring/Conf2	2.95	2.72	0.22	This work
TDDFT in PCM($\epsilon = 4$) Ring/Conf1	2.89	2.64	0.25	This work
<TDDFT>	2.93	2.71	0.21	

Table 3.9: Comparison between experimental and TDDFT absorption (ABS), emission energies (FLU) and Stokes shifts (SS) of TO intercalated in different double stranded DNA (dsDNA). All values are in eV.

Calculations fully confirm this analysis: including the effects of the DNA pocket (through the ring approximation) the excited state TO remains almost planar in contrast to what found for calculations of monomer TO in the gas-phase or in a PCM water (see Table 3.6) and its fluorescence is not quenched (once again, calculations overestimate transition energies by the same 0.5 eV factor). This picture does not change if we introduce the effects of the rest of DNA (and possibly of the external solvent) using a PCM description, TO mimic this effective environment as a low polar or a water-like dielectric.

In order to better understand the role of the DNA pocket we have further extended the QM analysis to single stranded DNA (ssDNA). As no experimental structures are available for TO in ssDNA we have derived alternative pocket structures from the X-ray crystallographic study of Lisgarten et al. [226] on cryptolepine binding to a dsDNA. Our choice has been based on the observation that TO and cryptolepine are structurally similar (they are both aromatic planar and almost planar systems after intercalation), and thus we expect that also their intercalation pockets

are similar.

From this experimental structure we have extracted a pocket formed by two cytosine base pairs: this pocket has been used to model a possible intercalation site for TO in poly(dC). In Figure 3.22 the structures optimized for the ground and the excited state of TO intercalated in the model ssDNA pocket are shown. The different configurations have been obtained rotating TO along its long axis (ssConf1 vs. ssConf2) and short axis (A vs. B); we note that for the ssConf1B only the ground state structure is shown as in its excited state the benzothiazole group rotates with consequent quenching of the fluorescence.

In Table 3.10, we report the corresponding absorption and emission energies and Stokes shifts together with a collection of experimental data taken from the literature for TO in different ssDNA. The results reported in Table 3.10 for TO partially intercalated in ssDNA well agree with the experimental results if the 0.5 eV offset is considered. We note that in particular the Stokes shifts values measured in poly(dC) are very well reproduced by calculations which seems to support the partial intercalation [227] hypothesis we have used in which TO is located between two adjacent bases of the ssDNA (see Figure 3.22). If, alternatively, we consider a "classical" intercalation [181,182] of TO in the ssDNA, namely with a single ring in between the bases' planes, the optimization of the excited state structures leads to a twisted TO with a consequent quenching of the fluorescence. Therefore, according to our estimates a classical intercalation hypothesis for TO intercalated in a ssDNA seems not to be in agreement with the experimental results of fluorescence. [194]

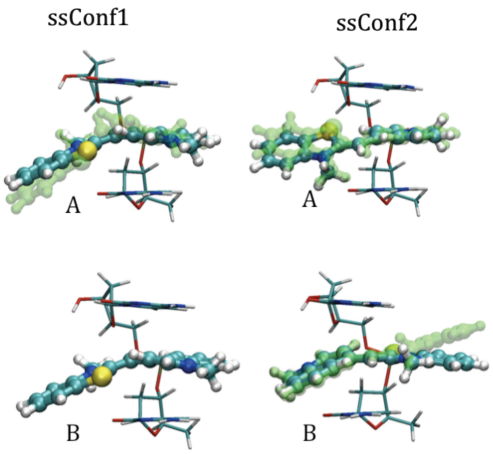

Figure 3.22: Optimized molecular structures of TO intercalated in single stranded DNA in several intercalated configurations, together with the superimpositions of excited structures (green).

Environment	ABS	FLU	SS	Ref.
In poly(dC)	2.61	2.34	0.27	[218]
In poly(dT)	2.60	2.33	0.27	[218]
In poly(dG)	-	2.34	-	[218]
In poly(dA)	2.45	2.36	0.09	[218]
In poly(dA)	-	2.36	-	This work
ssConf1A in poly(dC)	3.02	2.81	0.21	This work
ssConf1B in poly(dC)	2.89	Twist	-	This work
ssConf2A in poly(dC)	2.82	0.34	0.34	This work
ssConf2B in poly(dC)	3.00	2.77	0.22	This work
<TDDFT>	2.93	2.69	0.24	

Table 3.10: Comparison between experimental and calculated absorption (ABS) and emission (FLU) energies and Stokes shift (SS) of ssDNA-intercalated TO. All values are in eV.

Conclusions and perspectives

The aim of this theses has been the modelling of environment effects on spectroscopic molecular responses with hybrid QM/classical methods, in order to model environment effects and to gain a better comprehension of their microscopic origin.

In particular, in **Chapter 2** we have applied an extension of PCM to investigate solvent effects on vibrational couplings within the TDC and HMR approaches. In the case of TDC, we have studied a model system with the aim of dissecting solvent effects in their two main contributions, namely the modification of the transition dipole moments and the screening of their interaction. As the two contributions generally act in opposite directions, the final effect can be either an increase or a decrease of the coupling (and as a result a faster or slower energy transfer). The TDC approach, however, cannot be used to get a quantitative description of the phenomenon due to its intrinsic limitations, which can be further amplified by the presence of the solvent. The application of the much more reliable HMR-PCM formalism shows that this combination, can effectively predict and interpret the vibrational couplings of nucleic acids and peptides in solution.

Finally, we have applied an improved methodology, developed in this PhD thesis to nucleic acids. This methodology makes use of: a) the HMR-PCM approach in order to determine the coupling between vibrations; b) the PHVA in order to accurately determine the vibrational LM's; c) an explicit description of the nearest parts of the DNA helix, in order to account for a part of the DNA environment effect; and d) a continuous description in order to account (in an average manner) for the effect of the rest of the DNA helix and of the solvent. This combination was shown suitable for effectively predict and interpret some features of the 2D-IR spectra of nucleic acids in solutions. Its good correlation with both previous calculations and

experimental findings shows that this method can indeed be used in combination with experimental measurements to gain an accurate modelling of the vibrational coupling between vibrations localized on different DNA bases. Therefore, it can be envisaged as a useful tool to be exploited to determine, through the modifications of the coupling, the modifications in DNA helices.

In **Chapter 3**, we have presented the modelling of environment effects on the electronic absorption and fluorescence spectra, for homogeneous solvents, membranes and pockets in DNA.

Firstly, we have shown that the environment effect in homogeneous solvents, is a complex phenomenon in which very different interactions play a role, each with its proper dynamics. Such a complexity has direct important consequences in the large use that solvatochromism has in many fields of chemical and biological research. In fact, a clear and univocal relation between the position of absorption or fluorescence maxima and the characteristics of the environment cannot be obtained using simplified solvation models or even more complex polarity scales. Indeed, a detailed analysis of the static and dynamic aspects of solvation should be taken into account. We have shown that a new interpretative and predictive strategy is obtained by combining TDDFT approaches with various solvation models. Using only a single type of solvation model (either a continuum approach or an atomistic one) is in fact necessarily limited not only in the quality of the results but also in the completeness of the physical picture it can give, which can be achived. We have tried to show that it is the integration of different (and complementary) solvation models that can reveal the real nature of solvatochromism by directly relating it to the effects of the environment on the formation and relaxation of excited states. In particular, by combining MD and QM descriptions, as well as integrating QM/continuum with QM/polarizable MM and full QM descriptions of the absorption and emission phenomena, we have shown that even in the case of very common and largely studied fluorescent probes, the analysis of solvatochromism is far from being simple and univocal. Many are in fact the aspects which can play a role, and some of them are only indirectly linked to the polarity and/or H-bonding characteristics of the environment. For example, one cannot neglect solubility effects which can hide un-

expected shifts in the spectroscopic responses due not to direct environment effects but to environment-induced aggregations. More important, specific solute-solvent effects such as H-bonds not only can lead to large shifts of both absorption and emission energies but also can affect the nature of the emitting species with resulting reduction of the quantum yield. For some of the investigated probes, we have shown that strong H-bonding effects could lead to protonation of the acceptor sites in the probe or conformational changes.

Secondly, we have considered the environment effects of membranes on selected molecular probes. This implies the connection between the electronic transitions of the probe and how these are affected by the environment, on one side, and the probe distribution in the bilayer and the factors that determine its changes as a function of bilayer composition or external perturbations, on the other side. The integrated QM/PCM and MFT approach, which we have proposed here, appears suitable for a thorough analysis of the spectroscopic properties of fluorescent probes as a function of their interaction with the bilayer environment. The application of this integrated approach to the fluorescent probes Acdan, Prodan, and Laurdan in a model liquid-crystalline DPPC bilayer highlighted important effects. A strong dependence of the fluorescence emission wavelength on the position and orientation of the chromophore inside of the bilayer was evidenced by the QM/PCM calculations, and the molecular field analysis evidenced the actual role of different probe configurations in modulating the emission spectrum. In particular, non-obvious and usually disregarded effects of the orientational and conformational distributions of the probes emerged, which were shown to be able to indirectly affect the spectroscopic response. A complex picture is suggested, where the dynamic contributions, during the fluorescence lifetime, from probes heterogeneously distributed across the bilayer should be considered. The QM/PCM description of the electrostatic effects were found to be insufficient to explain the origin of the red-shifted emission observed for Prodan and Laurdan in membranes; these could be accounted for by introducing the specific effects of H-bonding interactions between the probes and the water molecules penetrating into the bilayer. Thus, our analysis provides support to the hypothesis that the short- and longwavelength maxima in the fluorescence spectra of Prodan

and Laurdan correspond to a H-bond-free and a H-bonded form of the probe, respectively. [170] Although, strictly speaking, our results refer to probes incorporated in a liquid-crystalline DPPC bilayer, some of our conclusions concerning the role of H-bonds and the importance of the conformational and orientational distribution of the probes are expected to be generally meaningful. However, due to the great sensitivity to the physical state and composition of the bilayer exhibited by the spectroscopic response, especially in the case of Prodan, the specific features of the lipid phase should be taken into account to get more accurate predictions, allowing a closer comparison with experiments. The integrated approach used here for the first time appears suitable to bridge the spectroscopic behavior of polarity-sensitive probes and microenvironment properties of lipid membranes.

Finally, we have considered the environment effects of pockets in DNA on Thiazole Orange. The detailed understanding of the physical and chemical aspects related to environment effects on molecular probes for DNA, which are used in the frame of biochemical and biophysical sensing, is indeed a very important issue. In this study we have shown that a possible reliable strategy is based on the integration of computational and spectral methods. In particular, the use of recent DFT functionals in combination with TDDFT extensions to excited state geometries allows us to reproduce the experimental shifts in the absorption and fluorescence bands when moving from the isolated chromophore to the chromophore in different environments of increasing complexity. This strategy has been here applied to the study of TO in the gas-phase and in solution with different conditions of viscosity and different concentrations, and to TO intercalated in single and double stranded DNA. The comparison of the results obtained simulating the different experimental situations with a hierarchy of QM models has finally allowed us to rationalize the quenching/enhancing effects of fluorescence that occur passing from non-viscous to viscous solvents, as well as from solutions to single and double stranded DNA. In the latter cases, QM calculations confirm that intercalation inhibits the twisting of TO in its excited state due to the rigid DNA pocket which is finally reflected in an enhanced fluorescence. The twisting effect on fluorescence quenching does not preclude the presence of other common mechanisms of quenching, such as that due

to water, but it indicates that TO presents a specificity with respect to other dyes where the twisting is not possible.

To summarise, we have shown that the various approaches we have adopted were able to predict and interpret the environment effects on vertical electronic transitions, vibrational transitions and vibrational couplings. However, it is important to point out that there is not a unique approach to study environment effects, but that each approach reveals specific and complementary aspects; thus also the accuracy of the different approaches depends on the peculiar characteristics of the environment.

Further efforts have to be made in order to improve the description of the interaction with the environment, considering the dispersive and repulsive interactions (and not only the electrostatic interactions), the explicit coupled dynamics and the specific persistent interaction which are the key factors in order to better model environment effects in protic environments.

Appendix A

Modelling molecular vibrations: the normal modes (NM's) analysis and the Partial Hessian Vibrational Analysis (PHVA)

The modelling of molecular vibrations in polyatomic systems is usually performed using the Normal Modes (NM's) analysis. It is convenient to start by considering the molecular Hamiltonian of the nuclei, in a rotating and translating frame,[1] and in the Born–Oppenheimer approximation.

$$H\left(\{x_i\}\right) = -\frac{\hbar^2}{2}\sum_i \frac{1}{m_i}\frac{\partial^2}{\partial x_i^2} + V\left(\{x_i\}\right) \tag{A.0.1}$$

where m_i is the mass of the nucleus i. The first term in the former equation, is the kinetic energy operator, whereas the second represents the potential energy that determines the vibrational motion of the nuclei.

The potential energy term, that is obtained from the solution of the electronic

[1]For a semi-rigid molecule (a molecule in which the only motions are small internal vibrations and overall translations and rotations) in a minimum of the Potential Energy Surface, this frame is obtained imposing a set of six constaints on the coordinates, named the Eckart-Sayvetz conditions. These conditions uncouple the $3n$ nuclear degrees of freedom in $3n-6$ internal (vibrational) coordinates and in 6 rigid body motions (the overall 3 rotational and 3 translational motions).

Schrödinger equation, is a function of the nuclear coordinates and cannot be written in a simple analytical form; therefore a common solution is to make an expansion using the Taylor's series for the motion of the nuclei around the equilibrium position, which gives

$$V\left(\{x_i\}\right) = V\left(\{x_i^0\}\right) + \sum_i \left.\frac{\partial V}{\partial x_i}\right|_{x_i^0} \left(x_i - x_i^0\right) + \frac{1}{2}\sum_{i,j} \left.\frac{\partial^2 V}{\partial x_i \partial x_j}\right|_{x_i^0, x_j^0} \left(x_i - x_i^0\right)\left(x_j - x_j^0\right) + \ldots \tag{A.0.2}$$

An harmonic description (taking into account the potential energy up to the second order and neglecting the higher order terms) is usually a reasonable approximation, for small displacement around a minimum[2]. Thus the Hamiltonian can be rewritten as:

$$H\left(\{x_i\}\right) = -\frac{\hbar^2}{2}\sum_i \frac{1}{m_i}\frac{\partial^2}{\partial x_i^2} + \frac{1}{2}\sum_{i,j} \left.\frac{\partial^2 V}{\partial x_i \partial x_j}\right|_{x_i^0, x_j^0} \left(x_i - x_i^0\right)\left(x_j - x_j^0\right) \tag{A.0.3}$$

A further simplification can be performed by introducing the mass-weighted Cartesian displacement coordinates, $q_i = m_i^{1/2}\left(x_i - x_i^0\right)$, obtaining:

$$H\left(\{q_i\}\right) = -\frac{\hbar^2}{2}\sum_i \frac{\partial^2}{\partial q_i^2} + \frac{1}{2}\sum_{i,j} \left.\frac{\partial^2 V}{\partial q_i \partial q_j}\right|_0 q_i q_j \tag{A.0.4}$$

The presence of cross-terms in the former equation prevents a simple analytical solution of the problem; a common choice is to make a change of cooordinates, named normal coordinates:

$$\boldsymbol{Q} = \boldsymbol{L}\boldsymbol{q} \tag{A.0.5}$$

to remove the cross-terms and transform the double sum in Eq. (A.0.4) to a single sum. This diagonalization reduces the problem to a system of uncoupled harmonic oscillators, that is trivial to solve. Thus using normal coordinates the Hamiltonian can be written as a sum of Hamiltonians of uncoupled quantum harmonic oscilla-

[2]We are considering only small displacements from the equilibrium configuration and not chemical reactions or conformational changes, which need large modifications of the nuclear coordinates.

tors[3]:

$$H\left(\{Q_i\}\right) = \frac{1}{2}\sum_i h\left(\{Q_i\}\right) = \frac{1}{2}\sum_i \left\{-\hbar^2\frac{\partial^2}{\partial Q_i^2} + \left.\frac{\partial^2 V}{\partial Q_i^2}\right|_0 Q_i^2\right\} \tag{A.0.6}$$

where $\frac{\partial^2 V}{\partial Q_i^2}$ is the force constant k_i associated to the normal coordinate Q_i.

The former equation is analytically solvable giving the following vibrational energy:

$$E = \sum_i \hbar\omega_i\left(n_i + \frac{1}{2}\right) \tag{A.0.7}$$

where n_i is the quantum number and $\omega_i = \sqrt{k_i}$ the frequency associated to the i-th normal mode.

We can briefly summarize how a quantum chemical software, like Gaussian, obtains the vibrational frequencies and NM's:

- Calculation of the hessian matrix in Cartesian displacement coordinates, as the second derivatives of the potential energy, $F_{ij} = \left.\frac{\partial^2 V}{\partial x_i \partial x_j}\right|_{x_i^0, x_j^0}$ (See Eq. (A.0.3))
- Coordinate transformations:
  - from Cartesian to mass-weighted Cartesian coordinates ($\boldsymbol{q}$), using the transformation matrix $\boldsymbol{M}$ (defined as: $M_{ii} = m_i^{1/2}$).
  - from mass-weighted Cartesian displacement coordinates to the translating + rotating system, i.e. the internal coordinates, using the transformation matrix $\boldsymbol{D}$. This is done using the Sayvetz conditions, which separate the $3n-6$ internal (vibrational) motions from the 6 rigid body motions.

[3]The same consideration can be applied to the Lagrangian (classical) analogue of Eq. (A.0.4), $L\left(\{q_i\}\right) = \frac{1}{2}\sum_i \dot{q}^2 - \frac{1}{2}\sum_{i,j} f_{ij}q_i q_j$, that can be solved using the Lagrangian equation of motion, obtaining $\ddot{q}_i + \sum_j f_{ij}q_j = 0 \quad i = 1, 2, \ldots 3n$. Analogously to Eq. (A.0.4) it contains cross-terms, that prevent a solution in terms of uncoupled oscillators. Analogously to Eq. (A.0.6) the former Lagrangian can be written, in terms of normal modes as, $L\left(\{q_i\}\right) = \frac{1}{2}\sum_i \dot{q}^2 - \frac{1}{2}\sum_{i,j} K_{ii}q_i^2$, that can be solved using the Lagrangian equation of motion, obtaining $\ddot{q}_i + \sum_i f_i q_i = 0 \quad i = 1, 2, \ldots 3n$. Its solutions are the harmonic oscillator functions $q_i = A_i \sin\left(2\pi ct + \phi\right)$ in which each nucleus in the molecule is moving with the same frequency and phase. For a general polyatomic molecule, this provides $3n-6$ vibrational (normal) frequencies $\nu_i = f_i^{1/2}$, and the corresponding normal mode displacements A_i.

– from internal coordinates to normal coordinates ($\boldsymbol{Q}$), using the transformation matrix $\boldsymbol{L}$.

To sum up: $\boldsymbol{Q} = \boldsymbol{MDLq}$.

- Calculation of vibrational frequencies and NM displacements, obtained as the eigenvectors and eigenvalues of the hessian matrix.

The NM's analysis was originally developed in order to study vibrations in a minimum of the potential energy surface. However, it is sometimes needed to perform vibrational calculations in partially optimized structures, i.e. not in an energy minimum, where the investigated part of the system is optimized and the rest is not. This because a global optimization may be very expensive or because we are only considering a fragment of a larger structure, in which the border needs to be kept frozen, to correctly account for the vibrational edge effects. In fact a standard NM's analysis of these systems may show some serious drawbacks, e.g. the appearance of imaginary frequencies, the breakdown of the rotational invariance and the appearance of coordinates dependence. [228] In order to overcome these limitations the Partial Hessian Vibrational Analysis (PHVA) [59–61, 64, 229–231] was initially developed by Head et al. [61–63, 229] and further by Li and Jensen. [232] This approach divides the system into a freely vibrating part and a frozen part; the latter is kept frozen during the vibrational calculation, formally setting to infinite the masses associated to the atoms of the fixed part (this is equal to considering and diagonalizing only a sub-block of the Hessian, neglecting the elements associated to the frozen part). Therefore the frozen part does not directly contribute to the vibrational calculation.

Appendix B

Molecular field theory (MFT) for solutes in membrane environments

The MFT [152] description of the positional and orientational distribution of a molecular solute in membrane environments is based on the definition of a molecular mean-field potential (U), expressed as the sum of the work required to form the molecular-shaped cavity (U_{cav}), the electrostatic (U_{el}) and dispersion (U_{disp}) solute-membrane interactions, and the anisotropic interactions between the solute and the ordered acyl chains in the membrane interior (U_{ord}):

$$U = U_{cav} + U_{el} + U_{disp} + U_{ord} \tag{B.0.1}$$

Due to the nonuniform and anisotropic nature of the bilayer environment, each term in the former equation bears a dependence on the position of the solute along the bilayer normal (Z), on its orientation with respect to the normal (Ω) and, in the case of flexible solutes, on the torsional angles (χ). An atomistic representation of the solute is used, in terms of its atomic charges and polarizabilities and of the solvent excluded molecular surface.

The mean-field potential $U(Z, \Omega, \chi)$ is related to the coupled positional-orientational-conformational distribution function $P(Z, \Omega, \chi)$ by

$$P(Z, \Omega, \chi) = \frac{e^{\frac{U(Z,\Omega,\chi)}{k_B T}}}{Q} \tag{B.0.2}$$

with the partition function

$$Q = \int e^{\frac{U(Z,\Omega,\chi)}{k_B T}} dZ d\Omega d\chi \tag{B.0.3}$$

By properly averaging $P(Z,\Omega,\chi)$ over the orientational and conformational variables, the reduced position distribution function $P_{\Omega,\chi}(Z)$ is defined, such that $P_{\Omega,\chi}(Z)\,dZ$ gives the probability that the solute is located in the element dZ centered at the Z position, irrespective of its orientation and conformation. We can also define a position-dependent free energy,

$$u_{\Omega,\chi}(Z) = u^{\text{bulk}}_{\Omega,\chi}(Z) - k_B T \ln P_{\Omega,\chi}(Z) \tag{B.0.4}$$

which can be interpreted as the transfer free energy from bulk water to the Z position in the bilayer, if $u^{\text{bulk}}_{\Omega,\chi}(Z) = k_B T \ln P^{\text{bulk}}_{\chi}(Z) = \text{const}$, where $P^{\text{bulk}}_{\chi}(Z)$ is the reduced distribution in bulk water.

Acknowledgments

I gratefully acknowledge all the people I have collaborated with during this Ph.D. In particular I would like to thank my supervisor, Prof. Benedetta Mennucci, guiding me through the PhD with enthusiasm and competence, Dr. Chiara Cappelli and Prof. Roberto Cammi.

Special thanks also go to all people who are and have been in the PCM research group during these years: Stefano, Filippo, Ciro, Angel, Aurora, Carles...

I would like to thank Luca Frediani for welcoming me to visit CTCC in Tromsø.

I would also like to acknowledge my dear friends Fabio, Valerio, Lucia and Francesco, who have always been willing to support me during these years.

I also wish to express my gratitude to my family, for its important support during my graduate studies.

List of Publications

This PhD thesis is based on the following publications:

1. A. Biancardi, C. Cappelli, B. Mennucci, R. Cammi
   Toward a Quantum-Mechanical Description of 2D-IR Spectra of Solvated Systems: The Vibrational Mode Coupling within A Polarizable Continuum Model
   J. Phys. Chem. B 2010, 114, 4924

2. A. Marini, A. Muñoz-Losa, A. Biancardi, B. Mennucci
   What is solvatochromism?
   J. Phys. Chem. B 2010, 114,17128

3. A, Biancardi, T. Biver, A. Marini, B. Mennucci, F. Secco
   Thiazole orange (TO) as a light-switch probe: a combined quantum-mechanical and spectroscopic study
   Phys. Chem. Chem. Phys. 2011, 13, 12595

4. G. Parisio, A. Marini, A. Biancardi, A. Ferrarini, B. Mennucci
   Polarity-sensitive fluorescent probes in lipid bilayers: bridging spectroscopic behavior and microenvironment properties.
   J. Phys. Chem. B 2011, 115, 9980

5. A. Biancardi, R. Cammi, C. Cappelli, B. Mennucci, J. Tomasi
   Modeling vibrational coupling in DNA oligomers: a computational strategy combining QM and continuum solvation models
   (Accepted in Theoretical Chemistry Accounts)

Bibliography

[1] J. Tomasi, B. Mennucci, and R. Cammi. *Chem. Rev.*, 105:2999, 2005.

[2] J.Tomasi and M. Persico. *Chem. Rev.*, 94:2027, 1994.

[3] S. Miertus, E. Scrocco, and J. Tomasi. *Chem. Phys.*, 55:117, 1981.

[4] R. Cammi and J. Tomasi. *J. Comp. Chem.*, 16:1449, 1995.

[5] E. Cancés, B. Mennucci, and J. Tomasi. *J. Chem. Phys.*, 107:3032, 1997.

[6] B. Mennucci, E. Cancés, and J. Tomasi. *J. Phys. Chem. B*, 101:10506, 1997.

[7] M. Cossi, G. Scalmani, N. Rega, and V. Barone. *J. Chem. Phys.*, 43:117, 2002.

[8] Onsager L and Samaras N. N. T. *J. Chem. Phys.*, 2:528, 1934.

[9] L. Frediani, R. Cammi, S. Corni, and J. Tomasi. *J. Chem. Phys.*, 120:82004, 2004.

[10] P. B. Petersen and R. J. Saykally. *Annu. Rev. Phys. Chem.*, 57:333, 2006.

[11] C.Curutchet, A. Munoz-Losa, S. Monti, J. Kongsted, and G. D. Scholes ; B. Mennucci. *J. Chem. Theory Comput.*, 5:1838, 2009.

[12] R. Cammi and B. Mennucci. *J. Chem. Phys.*, 110:9877, 1999.

[13] M. E. Casida, D. P. In Recent AdVances in Density Functional Methods; Chong, Ed.; World Scientific: Singapore, and 1995; Part I.

[14] B. D. Bursulaya, D. A. Zichi, and H. J. Kim. *J. Phys. Chem.*, 99:10069, 1995.

[15] R. Cammi, S. Corni, B. Mennucci, and J. Tomasi. *J. Chem. Phys.*, 122:104513, 2005.

[16] M. Caricato, B. Mennucci, J. Tomasi, F. Ingrosso, R. Cammi, and G. Scalmani S. Corni. *J. Chem. Phys.*, 124:124520, 2006.

[17] P. Hamm, M. Lim, W. F. Degrado, and R. M. Hochstrasser. *Proc. Natl. Acad. Sci. USA*, 96:2036, 1999.

[18] J. Zheng, K. Kwak, and M. D. Fayer. *Acc. Chem. Res.*, 40:75, 2007.

[19] B. Henry. *J. Phys. Chem.*, 80:2160, 1976.

[20] B. Henry. *Acc. Chem. Res.*, 10:207, 1977.

[21] M. Sage. *Adv. Chem. Phys.*, 47:293, 1981.

[22] M. Child. *Adv. Chem. Phys.*, 57:1, 1984.

[23] L. Halonen. *Adv. Chem. Phys.*, 104:41, 1998.

[24] P. Jensen. *Mol. Phys.*, 17:1253, 98.

[25] M. H. Cho. Coherent two-dimensional optical spectroscopy. *Chem. Rev.*, 108:1331, 2008.

[26] R. D. Gorbunov, D. S. Kosov, and G. Stock. *J. Chem. Phys.*, 122:224904, 2005.

[27] S. Ham, S. Cha, J.-H. Choi, and M. J. Cho. *Chem. Phys.*, 119:1451, 2003.

[28] Torii H.; Tasumi M. *in Infrared Spectroscopy of Biomolecules and ed. H. H. Mantsch and D. Chapman.* John Wiley & Sons and New York, 1996.

[29] H. Torii and M. Tasumi. *J. Raman Spectrosc.*, 29:81, 1998.

[30] H. Torii and M. Tasumi. *J. Chem. Phys.*, 96:3379, 1992.

[31] S. Krimm and Y. Abe. *Proc. Natl. Acad. Sci. U.S.A.*, 69:2788, 1972.

[32] P. Hamm and S. Wouterson. *Bull. Chem. Soc. Jpn.*, 75:985, 2002.

[33] R.Cammi and J. Tomasi. *J. Chem. Phys.*, 100:7495, 1994.

[34] R.Cammi and J. Tomasi. *J. Chem. Phys.*, 101:3888, 1994.

[35] A. Moran and S. Mukamel. *Proc. Nat. Acad. Sci. U.S.A.*, 101:506, 2004.

[36] R. Cammi, C. Cappelli, S. Corni, and J. Tomasi. *J. Phys. Chem. A*, 104:9874, 2000.

[37] C. Cappelli and Continuum Solvation Approaches to Vibrational Properties. *In Continuum SolVation Models in Chemical Physics: Theory and Applications*. Wiley: Chichester and U.K., 2007.

[38] M. Iozzi, B. Mennucci, J. Tomasi, and R. Cammi. *J. Chem. Phys.*, 120:7029, 2004.

[39] T. Miyazawa, T. Shimanouchi, and S. Mizushima. *J. Chem. Phys.*, 24:408, 1956.

[40] V. N. Uversky and A. Permyakov. *Methods in Protein Structure and Stability Analysis*. Nova Science Pub. Inc., 2007.

[41] M. Jackson and H. H. Mantsch. The use and misuse of ftir spectroscopy in the determination of protein structure. *Crit. Rev. Biochem. Mol. Biol.*, 30:95, 1995.

[42] Y. Wang, R. Purrello, T. Jordan, and T. C. Spiro. *J. Am. Chem. Soc.*, 113:6359, 1991.

[43] A. Becke. *J. Phys. Chem.*, 98:5648, 1993.

[44] M. J. Frisch, G. W. Trucks, H. B. Schlegel, G. E. Scuseria, M. A. Robb, J. R. Cheeseman, J. A. Montgomery, Jr., T. Vreven, K. N. Kudin, J. C. Burant, J. M. Millam, S. S. Iyengar, J. Tomasi, V. Barone, B. Mennucci, M. Cossi, G. Scalmani, N. Rega, G. A. Petersson, H. Nakatsuji, M. Hada, M. Ehara, K. Toyota, R. Fukuda, J. Hasegawa, M. Ishida, T. Nakajima, Y. Honda, O. Kitao, H. Nakai, M. Klene, X. Li, J. E. Knox, H. P. Hratchian, J. B.

Cross, V. Bakken, C. Adamo, J. Jaramillo, R. Gomperts, R. E. Stratmann, O. Yazyev, A. J. Austin, R. Cammi, C. Pomelli, J. W. Ochterski, P. Y. Ayala, K. Morokuma, G. A. Voth, P. Salvador, J. J. Dannenberg, V. G. Zakrzewski, S. Dapprich, A. D. Daniels, M. C. Strain, O. Farkas, D. K. Malick, A. D. Rabuck, K. Raghavachari, J. B. Foresman, J. V. Ortiz, Q. Cui, A. G. Baboul, S. Clifford, J. Cioslowski, B. B. Stefanov, G. Liu, A. Liashenko, P. Piskorz, I. Komaromi, R. L. Martin, D. J. Fox, T. Keith, M. A. Al-Laham, C. Y. Peng, A. Nanayakkara, M. Challacombe, P. M. W. Gill, B. Johnson, W. Chen, M. W. Wong, C. Gonzalez, and J. A. Pople. Gaussian 03, revision b.05. Gaussian, Inc., Wallingford, CT, 2004.

[45] A. Bondi. *J. Phys. Chem.*, 68:441, 1964.

[46] C. Cappelli and B. Mennucci. *J. Phys. Chem. B*, 112:3441, 2008.

[47] J. Tomasi, B. Mennucci, and R. Cammi. *Chem. Rev.*, 105:2999, 2005.

[48] T. Forster. *Ann. Phys.*, 2:55, 1948.

[49] I. V. Rubtsov and R. M. Hochstrasser. *J. Phys. Chem. B*, 106:9165, 2002.

[50] N. T. Hunt. *Chem. Soc. Rev.*, 38:1837, 2009.

[51] A.D. Richards and A. Rodger. *Chem. Soc. Rev.*, 36:471, 2007.

[52] A. Biancardi, T. Biver, A. Marini, B. Mennucci, and F. Secco. *Phys. Chem. Chem. Phys.*, 13:12595, 2011.

[53] A.T. Krummel and M.T. Zanni. *J. Phys. Chem. B*, 110:13991, 2006.

[54] C. Lee, K. Park, and M.Cho. *J. Chem. Phys.*, 125:114508, 2006.

[55] C. Lee, K. Park, and M.Cho. *J. Chem. Phys.*, 126:145102, 2007.

[56] C. Lee, K. Park, and M.Cho. *J. Chem. Phys.*, 125:114510, 2006.

[57] C. Lee, K. Park, and M.Cho. *J. Chem. Phys.*, 125:114509, 2006.

[58] M. McCall, T. Brown, and O. Kennard. *J. Mol. Biol.*, 183:385, 1985.

[59] N. A. Besley and K. A. Metcalf. *J. Chem. Phys.*, 126:035101, 2007.

[60] N. A. Besley and J. A. Bryan. *J. Phys. Chem. C*, 112:4308, 2008.

[61] S. Q. Jin and J. D. Head. *Surf. Sci.*, 318:204, 1994.

[62] J. D. Head. *Int. J. Quantum Chem.*, 65:827, 1997.

[63] J. D. Head. *Int. J. Quantum Chem.*, 77:350, 2000.

[64] J.D. Head and Y. Shi Y. *Int. J. Quantum Chem.*, 75:815, 1999.

[65] A. Ghysels, V. Van Speybroeck, T. Verstraelen, D. Van Neck, and M. Waroquier. *J. Chem. Theory Comput.*, 4:614, 2008.

[66] M. J. Frisch, G. W. Trucks, H. B. Schlegel, G. E. Scuseria, M. A. Robb, J. R. Cheeseman, G. Scalmani, V. Barone, B. Mennucci, G. A. Petersson, H. Nakatsuji, M. Caricato, X. Li, H. P. Hratchian, A. F. Izmaylov, J. Bloino, G. Zheng, J. L. Sonnenberg, M. Hada, K. Toyota M. Ehara, R. Fukuda, J. Hasegawa, M. Ishida, T. Nakajima, O. Kitao Y. Honda, H. Nakai, T. Vreven, J. J. A. Montgomery, F. Ogliaro J. E. Peralta, M. Bearpark, J. J. Heyd, E. Brothers, K. N. Kudin, V. N. Staroverov, R. Kobayashi, J. Normand, K. Raghavachari, J. C. Burant A. Rendell, S. S. Iyengar, M. Cossi J. Tomasi, N. Rega, M. Klene N. J. Millam, J. E. Knox, J. B. Cross, V. Bakken, C. Adamo, R. Gomperts J. Jaramillo, R. E. Stratmann, O. Yazyev, A. J. Austin, C. Pomelli R. Cammi, J. W. Ochterski, R. L. Martin, K. Morokuma, G. A. Voth V. G. Zakrzewski, P. Salvador, J. J. Dannenberg, S. Dapprich, O. Farkas A. D. Daniels, J. B. Foresman, J. V. Ortiz, J. Cioslowski, and D. J. Fox, editors. *GAUSSIAN 09 (Revision A.1) and Gaussian Inc. and Wallingford CT.* 2009.

[67] Y. Zhao and D. G. Truhlar. *Theor. Chem. Acc.*, 120:215, 2008.

[68] E. G. Hohenstein, S. T. Chill, and C. D. Sherrill. *J. Chem. Theory Comput.*, 4:1996, 2008.

[69] L. R. Rutledge and S. D. Wetmore. *Can. J. Chem.*, 88:815, 2010.

[70] R. Santamaria, E. Charro, A. Zacarías, and M. Castro. *J. Comput. Chem.*, 20:511, 1999.

[71] A. K. Chandra, M. T. Nguyen, T. Uchimaru, and T. Zeegers-Huyskens. *J. Phys. Chem. A*, 103:8853, 1999).

[72] A. Pelmenschikov, D. M. Hovorun, O. V. Shishkin, and J. Leszczynski. *J. Chem. Phys.*, 113:5986, 2000).

[73] T. K. Ha and H. H. Gunthard. *Spectrochim. Acta and Part A*, 57:55, 2001.

[74] J.S. Kwiatkowski and J. Leszczynski. *J. Phys. Chem.*, 100:941, 1996.

[75] A.T. Krummel, P. Mukherjee, and M.T. Zanni. *J. Phys. Chem. B*, 107:9165, 2003.

[76] K. Szczepaniak and M. Szczesniak. *J. Mol. Struct.*, 156:29, 1987.

[77] M. Szczesniak, K. Szczepaniak, J.S. Kwiatkowski, K. KuBulat, and W. B. Person. *J. Am. Chem. Soc.*, 110:8319, 1988.

[78] M. J. Nowak, L. Lapinski, and J. Fulara. *Spectrochim. Acta and Part A*, 45:229, 1989.

[79] G. N. Tena and V. I. Baranov. *J. Appl. Spectr.*, 72:155, 2005.

[80] M. J. Frisch, G. W. Trucks, H. B. Schlegel, G. E. Scuseria, M. A. Robb, J. R. Cheeseman, J. A. Montgomery, Jr., T. Vreven, K. N. Kudin, J. C. Burant, J. M. Millam, S. S. Iyengar, J. Tomasi, V. Barone, B. Mennucci, M. Cossi, G. Scalmani, N. Rega, G. A. Petersson, H. Nakatsuji, M. Hada, M. Ehara, K. Toyota, R. Fukuda, J. Hasegawa, M. Ishida, T. Nakajima, Y. Honda, O. Kitao, H. Nakai, M. Klene, X. Li, J. E. Knox, H. P. Hratchian, J. B. Cross, V. Bakken, C. Adamo, J. Jaramillo, R. Gomperts, R. E. Stratmann, O. Yazyev, A. J. Austin, R. Cammi, C. Pomelli, J. W. Ochterski, P. Y. Ayala, K. Morokuma, G. A. Voth, P. Salvador, J. J. Dannenberg, V. G. Zakrzewski, S. Dapprich, A. D. Daniels, M. C. Strain, O. Farkas, D. K. Malick, A. D. Rabuck, K. Raghavachari, J. B. Foresman, J. V. Ortiz, Q. Cui, A. G. Baboul,

S. Clifford, J. Cioslowski, B. B. Stefanov, G. Liu, A. Liashenko, P. Piskorz, I. Komaromi, R. L. Martin, D. J. Fox, T. Keith, M. A. Al-Laham, C. Y. Peng, A. Nanayakkara, M. Challacombe, P. M. W. Gill, B. Johnson, W. Chen, M. W. Wong, C. Gonzalez, and J. A. Pople. Gaussian 03. Gaussian, Inc., Wallingford, CT, 2004.

[81] I. M. Alecu, J. Zheng, Y. Zhao, and D. G. Truhlar. *J. Chem. Theory Comput.*, 6:2872, 2010.

[82] G. D. Scholes, C. Curutchet, B. Mennucci, R. Cammi, and J. Tomasi. *J. Phys. Chem. B*, 111:6978, 2007.

[83] P. Suppan and N. Ghoneim. *Solvatochromism.* The Royal Society of Chemistry: Cambridge, 1997.

[84] C. Reichardt. *Solvent and Solvent Effects in Organic Chemistry and 3rd ed.* Wiley-VCH: Weinheim, 2002.

[85] J. R. Lakowicz. *Principles of Fluorescence Spectroscopy.* Springer: New York, 2006.

[86] B. Valeur. *Molecular Fluorescence: Principles and Applications.* Wiley-VCH: Weinheim, 2001.

[87] B. A. Rowe, C. A. Roach, J. Lin, V. Asiago, O. Dmitrenko, and S. L. Neal. *J. Phys. Chem. A*, 112:13402, 2008.

[88] F.M. Cerezo, S.C. Rocafort, P.S. Sierra, F. Garcia-Blanco, and J.C. Sierra C.D. Oliva. *Helv. Chim. Acta*, 84:3306, 2001.

[89] O. F. Mohammed, O.-H. Kwon, C. M. Othon, and A. H. Zewail. *Angew. Chem. and Int. Ed.*, 48:6251, 2009.

[90] T. Yanai, D. P. Tew, and N. C. Handy. *Chem. Phys. Lett.*, 393:51, 2004.

[91] M. Chiba, T. Tsuneda, and K. Hirao. *J. Chem. Phys.*, 124:144106, 2006.

[92] W. L. Jorgensen, J. Chandrasekhar, J. D. Madura, R. W. Impey, and M. L. Klein. *J. Chem. Phys.*, 926:79, 1983.

[93] W. D. Cornell, P. Cieplak, C. I. Bayly, I. R. Gould, D. M. Ferguson K. M. Merz, D. C. Spellmeyer, T. Fox, Caldwell, and J. W. P. A. Kollman. *J. Am. Chem. Soc.*, 117:5179, 1995.

[94] D. A. Case, T. A. Darden, T. E. I. Cheatham, C. L. Simmerling, J. Wang, R. E. Duke, R. Luo, V. Merz, D. A. Pearlman, V. Crowley, R. C. Walker, W. Zhang, B. Wang, S. Hayik, A. Roitberg, G. Seabra, K. F. Wong F. Paesani, X. Wu, S. Brozell, V. Tsui, H. Gohlke, L. Yang, C. Tan, J. Mongan, V. Hornak, G. Cui, P. Beroza, D. H. Mathews, C. Schafmeister, W. S. Ross, and P. A. Kollman and, editors. *AMBER 9, University of California: San Francisco and CA.* 2006.

[95] U. C. Singh and P. A. Kollman. *J. Comput. Chem.*, 5:129, 1984.

[96] B. H. Besler, Jr K. M. Merz, and P. A. Kollman. *J. Comput. Chem.*, 11:431, 1990.

[97] H. C. Andersen. *J. Chem. Phys.*, 72:2384, 1980.

[98] T. Darden, D. York, and L. Pedersen. *J. Chem. Phys.*, 98:10089, 1993.

[99] A. E. Garcia and L. Stiller. *J. Comput. Chem.*, 14:1396, 1993.

[100] L. Gagliardi, R. Lindh, and G. Karlstrom. *J. Chem. Phys.*, 121:4494, 2004.

[101] G. Karlstrom, V. Lindh, P. Å. Malmqvist, B. O. Roos, U. Ryde, V. Veryazov, P.-O. Widmark, M. Cossi, B. Schimmelpfennig, and L. Seijo P. Neogrady. *Comput. Mater. Sci.*, 28:222, 2003.

[102] G. Weber and F. J. Farris. *Biochemistry*, 18:3075, 1979.

[103] J. Catalan, P. Perez, J. Laynez, and F. G. Blanco. *J. Fluoresc.*, 1:215, 1991.

[104] A. Marini, A. Muoz-Losa, A. Biancardi, and B. Mennucci. *J. Phys. Chem. B*, 114:17128, 2010.

[105] J. B. Massey, H. S. She, and H. J. Pownall. *Biochemistry*, 24:6973, 1985.

[106] Sommer A., Paltauf F., and Hermetter A. *Biochemistry*, 29:11134, 1990.

[107] T. Parasassi, A. M. Giusti, E. Gratton, E. Monaco, M. Raimondi, G. Ravagnan, and O. Sapora. *Inter. J. Radiation Biology*, 65:329, 1994.

[108] E. K. Krasnowska, L. A. Bagatolli, E. Gratton, and T. Parasassi. *Biochim. Biophys. Acta (BBA) - Biomembranes*, 1511:330, 2001.

[109] O.P. Bondar and E.S. Rowe. *Biophys. J.*, 76:956, 1999.

[110] B. Sengupta, J. Guharay, and P. K. Sengupta. *Spectrochim. Acta and Part A*, 56:1433, 2000.

[111] R. Hutterer and M. Hof. *J. Fluorescence*, 11:227, 2001.

[112] J. Sykora, P. Jurkiewicz ; R. M. Epand, Y. R. Kraa, M. Langner, and M. Hof. *Chem. and Phys. of Lipids*, 135:213, 2005.

[113] H. A. Wilson-Ashworth, Q. Bahm, J. Erickson, A. Shinkle, and M. P. Vu Woodbury D.; Bell J.D. *Biophys. J.*, 91:4091, 2006.

[114] B. C. Lobo and C. J. J. Abelt. *Phys. Chem. A*, 107:10938, 2003.

[115] R. K. Everett, H. A. A. Nguyen, and C. J. Abelt. *J. Phys. Chem. A*, 114:4946, 2010.

[116] B. N. Davis and C. J. Abelt. *J. Phys. Chem. A*, 109:1295, 2005,.

[117] G. Saroja, T. Soujanya, B. Ramachandram, and A. Samanta. *J. Fluorescence*, 8:405, 1998.

[118] A. Samanta. *Proc. Indian National Science Academy*, 69:95, 2003.

[119] T. Soujanya, R. W. Fessenden, and A. Samanta. *J. Phys. Chem.*, 100:3507, 1996.

[120] T. Soujanya, T. S. R. Krishna, and A. Samanta. *J. Phys. Chem.*, 96:8544, 1992.

[121] S. Das, A. Datta, and K. Bhattacharyya. *J. Phys. Chem. A*, 101:3299, 1997.

[122] G. Saroja and A. Samanta. *Chem. Phys. Lett.*, 246:506, 1995.

[123] L. U. Bucsiova and P. Hrdlovic. *J. Macro. Science and Part A: Pure and Applied Chemistry*, 44:1047, 2007.

[124] S. Mukherjee, K. Sahu, D. Roy, S. K. Mondal, and K. Bhattacharyya. *Chem. Phys. Lett.*, 384:128, 2004.

[125] D. E. Wetzler, C. Chesta, R. Fernandez-Prini, and P. F. Aramendia. *J. Phys. Chem. A*, 106:2390, 2002.

[126] K. Sahu, S. K. Mondal, D. Roy, R. Karmakar, and K. Bhattacharyya. *J. Photochem. Photobiol. A: Chemistry*, 172:180, 2005.

[127] O. A. Kucherak, P. Didier, Y. Mely, and A. S. Klymchenko. *J. Phys. Chem. Lett.*, 1:616, 2010.

[128] V. Karunakaran, T. Senyushkina, G. Saroja, J. Liebscher, and N. P. Ernsting. *J. Phys. Chem. A*, 111:10944, 2007.

[129] P. Ilich and F. G. Prendergast. *J. Phys. Chem.*, 93:4441, 1989.

[130] A. B. J. Parusel, F. W. Schneider, and G. Kohler. *J. Mol. Struct. (THEOCHEM)*, 398:341, 1997.

[131] B. Mennucci, M. Caricato, F. Ingrosso, C. Cappelli, R. Cammi, J. Tomasi, G. Scalmani, and M. J. Frisch. *J. Phys. Chem. B*, 112:414, 2008.

[132] W. R. Ware, S. K. Lee, G. J. Brant, and P. P. Chow. *J. Chem. Phys.*, 54:4729., 1971.

[133] T. Hagan, D. Pilloud, and P. Suppan. *Chem. Phys. lett.*, 139:499, 1987.

[134] G. Saroja, T. Soujanya, B. Ramachandram, T. Soujanya, and A. Samanta and R. W. Fessenden. *J. Phys. Chem.*, 100:3507, 1996.

[135] A. Samanta and R. W. Fessenden. *J. Phys. Chem. A*, 104:8972, 2000.

[136] N. A. Nemkovich and W. Baumann. *J. Photochem. Photobiol. and A*, 185:26, 2007.

[137] A. Balter, V. Nowak, W. Pawelkiewicz, and A. Kowalczyk. *Chem. Phys. Lett.*, 143:565, 1988.

[138] B. E. Cohen, A. Pralle, X. Yao, G. Swaminath, C. S. Gandhi, Y. N. Jan, B. K. Kobilka, E. Y. Isacoff, and L. Y. Jan. *Proc. Natl. Acad. Sci.*, 102:965, 2005.

[139] A. Marini, A. Munoz-Losa, A. Pucci, G. Ruggeri, and B. Mennucci. *Phys. Chem. Chem. Phys.*, 12:8999, 2010.

[140] D. Yuan and R. G. Brown. *J. Phys. Chem. A*, 101:3461, 1997.

[141] T. O. Harju, A. H. Huizer, and C. A. G. O. Varma. *Acta Chem. Scand.*, 49:829, 1995.

[142] D. Noukakis and P. Suppan. *J. Lumin.*, 47:285, 1991.

[143] F. Moyano, M. A. Biasutti, J. J. Silber, and N. M. Correa. *J. Phys. Chem. B*, 110:11838, 2006.

[144] F. Moyano, P. G. Molina, J. J. Silber, L. Sereno, and N. M. Correa. *Chem. Phys. Chem.*, 11:236, 2010.

[145] D.J. Fermin. *Adv. Electrochem. Sci. Eng.*, 9:127, 2006.

[146] M. De Serio, A.N. Bader, M. Heule, R. Zenobi, and V. Deckert. *Chem. Phys. Lett.*, 380:47, 2003.

[147] M. De Serio, H. Mohapatra, R. Zenobi, and V. Deckert. *Chem. Phys. Lett.*, 417:452, 2006.

[148] J. M. Perera and G. W. Stevens. *Anal. Bioanal. Chem.*, 395:1019, 2009.

[149] S. Sen, S. Yamaguchi, and T. Tahara. *Angew. Chem. Int. Ed.*, 48:6439, 2009.

[150] H. Wang, E. Borguet, and K. B. Eisenthal. *J. Phys. Chem. A*, 101:713, 1997.

[151] H. Wang, E. Borguet, and K. B. Eisenthal. *J. Phys. Chem. B*, 102:4927, 1998.

[152] G. Parisio and A. Ferrarini. *J. Chem. Theory Comput.*, 6:2267, 2010.

[153] P.L.-G. Chong. *Biochemistry*, 27:399, 1988.

[154] P.L.-G. Chong. *High Pressure Res.*, 5:761, 1990.

[155] T. Parasassi, G. De Stasio, A. d'Ubaldo, and E. Gratton. *Biophys. J.*, 60:1179, 1990.

[156] T. Parasassi, E.K. Krasnowska, L. Bagatolli, and E. Gratton. *J. Fluoresc.*, 8:365, 1998.

[157] J. Sykora, P. Kapusta, V. Fidler, and M. Hof. *Langmuir*, 18:571, 2002.

[158] L.A. Bagatolli. *Biochim. Biophys. Acta*, 1758:1541, 2006.

[159] G. Parisio, A. Marini, A. Biancardi, A. Ferrarini, and B. Mennucci. *J. Phys. Chem. B.*, 115:9980, 2011.

[160] A.D. Lùcio, C.C. Vequi-Suplicy, R.M. Fernandez, and M.T. Lamy. *J. Fluoresc.*, 20:473, 2010.

[161] J. Zeng and P.L.-G. Chong. *Biophys. J.*, 68:567, 1995.

[162] M. Kusube, H. Matsuki, and S. Kaneshina. *Colloids and Surf. B*, 42:79, 2005.

[163] M. Goto, H. Sawaguchi, N. Tamai, H. Matsuki, and S. Kaneshina. *Langmuir*, 26:13377, 2010.

[164] Y.-L. Zhang, J.H Frangos, and M. Chachisvilis. *Biochem. Biophys. Res. Commun.*, 347:838, 2006.

[165] H. Rottenberg. *Biochemistry*, 31:9473, 1992.

[166] T. Parasassi, F. Conti, and E. Gratton. *Cell. Mol. Biol.*, 32:103, 1986.

[167] T. Parasassi and E. Gratton. *J. Fluor.*, 5:59, 1995.

[168] P. Jurkiewicz, A. Olzynska, M. Langner, and M. Hof. *Langmuir*, 22,:8741, 2006.

[169] A. Olzynska, P. Jurkiewicz, and M. Hof. *J. Fluorescence*, 18:925, 2008.

[170] A.S. Klymchenko, G. Duportail, A.P. Demchenko, and Y. Mély. *Biophys. J.*, 86:2929, 2004.

[171] T.Parasassi, G. De Stasio, G. Ravagnan, R. M. Rusch, and E. Gratton. *Biophys. J.*, 60:179, 1991.

[172] P.L.-G. Chong and P.T.T. Wong. *Biochim. Biophys. Acta*, 1149:260, 1993.

[173] A. B. J. Parusel, W. Nowak, S. Grimme, and G. Köhler. *J. Phys. Chem. A*, 102:7149, 1998.

[174] D. Marsh. *Biochim. Biophys. Acta*, 1286:183, 1996.

[175] J. Barucha-Kraszewska, S. Kraszewski, P. Jurkiewicz, and M. Hof C. Ramseyer. *Biochim. Biophys. Acta*, 1798:1724, 2010.

[176] P.W Livanek, H.A. Huckabay, and R.C. Dunn. *J. Phys. Chem. B*, 113:10240, 2009.

[177] L.A. Bagatolli and E. Gratton. *Biophys. J.*, 78:290, 2000.

[178] S. Sun, M. P. Heitz, S. A. Perez, L. A. Colon, S. Bruckenstein, and F. V. Bright. *Appl. Spectr.*, 51:1316, 1997.

[179] K. A. Kozyra, J. R. Heldt, G. Gondek, P. Kwiek, , and J. Heldt. *Z. Naturforsch.*, 59a:809, 2004.

[180] M. Kupiainen, E. Falck, S. Ollila, P. Niemelä, and A. A. Gurtovenko. *J. Comp. Theory Nano*, 2:401, 2005.

[181] L. S. Lerman. *J. Mol. Bio.*, 18:39, 1961.

[182] L. S. Lerman. *Proc. Nat. Acad. Sci. U.S.A.*, 49:94, 1963.

[183] J. Liu and Y. Lu. *Methods Mol. Biol.*, 335:257, 2006.

[184] O. Krichevsky and G. Bonnet. *Rep. Prog. Phys.*, 65:251, 2002.

[185] R. Roy, S. Hohng, and T. Ha. *Nat. Methods*, 5:507, 2008.

[186] S. Muller. *Angew. Chem. and Int. Ed.*, 49:1197, 2010.

[187] K. E. Erkkila, D. T. Odom, and J. K. Barton. *Chem. Rev.*, 99:2777, 1999.

[188] Y. Jenkins, A. E. Friedman, N. J. Turro, and J. K. Barton. *Biochemistry*, 31:10809, 1992.

[189] K. Rurack. *Spectrochim. Acta and Part A*, 57:2161, 2001.

[190] R. E. Holmlin and J. K. Barton. *Inorg. Chem. (Washington and DC and U. S.)*, 34:7, 1995.

[191] J. Y. Han and K. Burgess. *Chem. Rev.*, 110:2709, 2010.

[192] S. J. Charlton and G. Vauquelin. *Br. J. Pharmacol.*, 161:1250, 2010.

[193] R. Pei, J. Rothman, Y. Xie, and M. N. Stojanovic. *Nucleic Acids Res.*, 37:e59, 2009.

[194] H. S. Rye and A. N. Glazer. *Nucleic Acids Res.*, 23:1215, 1995.

[195] D. G. Norman, R. J. Grainger, D. Uhrin, and D. M. Lilley. *Biochemistry*, 39:6317, 2000.

[196] H. S. Rye, S. Yue, D. E. Wemmer, M. A. Quesada, R. P. Haugland, R. A. Mathies, and A. N. Glazer. *Nucleic Acids Res.*, 20:2803, 1992.

[197] S. Gurrieri, K. S. Wells, I. D. Johnson, and C. Bustamante. *Anal. Biochem.*, 249:44, 1997.

[198] T. Biver, A. De Biasi, F. Secco, M. Venturini, and S. Yarmoluk. *Biophys. J.*, 89:374, 2005.

[199] B. A. Armitage. *Top. Curr. Chem.*, 253:55, 2005.

[200] A. H. Herz. *Photogr. Sci. Eng.*, 18:323, 1974.

[201] R. F. Khairutdinov and N. Serpone. *J. Phys. Chem. B*, 101:2602, 1997.

[202] W. West and S. Pearce. *J. Phys. Chem.*, 69:1894, 1965.

[203] E. S. Emerson, M. A. Conlin, A. E. Rosenoff, K. S. Norland, and D. Chin G. R. Bird H. Rodriguez. *J. Phys. Chem.*, 71:2396, 1967.

[204] R. Steiger, R. Pugin, and J. Heier. *Colloids Surf. B*, 74:484, 2009.

[205] T. Biver, A. Boggioni, F. Secco, E. Turriani, M. Venturini, and S. Yarmoluk. *Arch. Biochem. Biophys.*, 465:90, 2007.

[206] P. A. Hunt and M. A. Robb. *J. Am. Chem. Soc.*, 127:5720, 2005.

[207] A. Sanchez-Galvez, P. Hunt, M. A. Robb, M. Olivucci, T. Vreven, and H. B. Schlegel. *J. Am. Chem. Soc.*, 122:2911, 2000.

[208] C. S. M. Allan, B. Lasorne, G. A. Worth, and M. A. Robb. *J. Phys. Chem. A*, 114:8713, 2010.

[209] N. Glazer and H. S. Rye. *Nature*, 359:859, 1992.

[210] H. S. Rye, M. A. Quesada, K. Peck, R. A. Mathies, and A. N. Glazer. *Nucleic Acids Res.*, 19:327, 1991.

[211] K. Srinivasan, S. C. Morris, M. C.Kline J. E.Girard, and D. J. Reeder. *Appl. Theor. Electrophor.*, 3:235, 1993.

[212] E. Privat, T. Melvin, F. Merola, G. Schweizer, S. Prodhomme, and P. Vigny U. Asseline. *Photochem. Photobiol.*, 75:201, 2002.

[213] N. Svanvik, A. Stahlberg, U. Sehlstedt, R. Sjoback, and M. Kubista. *Anal. Biochem.*, 287:179, 2000.

[214] H. Zhu, S. M. Clark, S. C. Benson, H. S. Rye, A. N. Glazer, and R. A. Mathies. *Anal. Chem.*, 66:1941, 1994.

[215] L. G. Lee, C. Chen, and L. A. Chiu. *Cytometry*, 7:508, 1986.

[216] T. Y. Ogulchansky, M. Y. Losytskyy, V. B. Kovalska, and S. M. Yarmoluk V. M. Yashchuk. *Spectrochim. Acta and Part A*, 57:1525, 2001.

[217] G. L. Silva, V. Ediz, D. Yaron, and B. A. Armitage. *J. Am. Chem. Soc.*, 129:5710, 2007.

[218] J. Nygren, N. Svanvik, and M. Kubista. *Biopolymers*, 46:39, 1998.

[219] E. N. Kurtaliev, N. Nizomov, S. I. Rahimov, G. Khodjayev, and D. P. Khakimova. *Proc. SPIE*, 7571:7571161, 2007.

[220] M. Y. Losytskyy, V. B. Kovalska, and S. M. Yarmoluk. *Biopolym. Cell*, 16:75, 2000.

[221] K. D. Volkova, V. B. Kovalska, A. O. Balanda, M. Y. Losytskyy, A. G. Golub, R. J. Vermeij, V. Subramaniam, O. I. Tolmachev, and S. M. Yarmoluk. *Bioorg. Med. Chem.*, 16:1452, 2008.

[222] B. Garcia, S. Ibeas, R. Ruiz, J. M. Leal, T. Biver, F. Secco A. Boggioni, and M. Venturini. *J. Phys. Chem. B*, 113:188, 2009.

[223] V. Karunakaran, J. L. Perez Lustres, L. Zhao, N. P. Ernsting, and O. Seitz. *J. Am. Chem. Soc.*, 128:2954, 2006.

[224] H. Hilal and J. A. Taylor. *Dyes Pigm.*, 75:483, 2007.

[225] H. P. Spielmann, D. E. Wemmer, and J. P. Jacobsen. *Biochemistry*, 34:8542, 1995.

[226] J. N. Lisgarten, M. Coll, J. Portugal, C. W. Wright, and J. Aymami. *Nat. Struct. Mol. Biol.*, 9:57, 2002.

[227] N. J. Pritchard and A. Blake A. R. Peacocke. *Nature*, 212:1360, 1966.

[228] A. Ghysels, D. Van Neck, V. Van Speybroeck, T. Verstraelen, and M. Waroquier. *J. Chem. Phys.*, 126:224102, 2007.

[229] M. D. Calvin, J. D. Head, and S. Jin. *Surf. Sci.*, 345:161, 1996.

[230] J.D. Head. *Int. J. Quantum. Chem.*, 65:827, 1997.

[231] J.D. Head. *Int. J. Quantum. Chem.*, 77:350, 2000.

[232] H. Li and J. H. Jensen. *Theor. Chem. Acc.*,, 107:211, 2002.

List of Figures

List of Tables